Big-Data-Driven Multi-Scale Experimental Study of Nanostructured Block Copolymer's Dynamic Toughness

By

Hanxun Jin

M. Sc., Solid Mechanics, Brown University, 2017

B.Eng., Mechanical Engineering, Nanjing Tech University, 2015

B.B.A., Finance and Accounting, Nanjing Tech University, 2015

A dissertation submitted in partial fulfillment of the

requirements for the Degree of Doctor of Philosophy

in the School of Engineering at Brown University

PROVIDENCE, RHODE ISLAND

Feb, 2022

This thesis by Hanxun Jin is accepted in its present form

by the School of Engineering as satisfying the

thesis requirements for the degree of Doctor of Philosophy

Date_____ _____

Prof. Kyung-Suk Kim, Advisor

Recommended to the Graduate Council

Date_____ _____

Prof. Huajian Gao, Reader

Date_____ _____

Prof. Pradeep R. Guduru, Reader

Date_____ _____

Prof. George Em Karniadakis, Reader

Approved by the Graduate Council

Date_____ _____

Prof. Andrew G. Campbell, Dean of the Graduate School

Curriculum Vitae

Hanxun Jin was born in Suzhou, Jiangsu Province, P.R.China, in August 1993. He graduated from Nanjing Tech University with a B.Eng. degree in Mechanical Engineering and Automation, and a B.B.A. degree in Finance in June 2015. Subsequently, he started his ScM. program in Mechanics of Solids at Brown University, School of Engineering. He received ScM. Degree in Engineering in May 2017. His research mainly focused on studying the mechanics of soft materials' self-organization through multi-scale experimental and computational approaches.

Publications

• Journal Articles: (Not included in this thesis)

1. **H. Jin**, AK. Landauer, K.-S. Kim. Ruga mechanics of soft-orifice closure under external pressure. Proceedings of the Royal Society A, 2021, 477(2249): 20210238. https://doi.org/10.1098/rspa.2021.0238.

2. Z. Rao, **H. Jin**, A. Engwall, E. Chason, K.-S. Kim. Determination of stresses in incrementally deposited films from wafer-curvature measurements. Journal of Applied Mechanics, 2020, 87(10). https://doi.org/10.1115/1.4047572.

• Conference Proceedings:

1. **H. Jin**, C. Machnicki, J. Hegarty, R.J. Clifton, K.-S. Kim, Understanding the nano-scale deformation mechanisms of Polyurea from *in-situ* AFM tensile experiments, Conference Proceedings of the 2021 Annual Meeting of Society for Experimental Mechanics. (To be published)

2. K.-S. Kim, **H. Jin**, T. Jiao, R.J. Clifton. Dynamic Fracture-Toughness Testing of a Hierarchically Nano-Structured Solid. Fracture, Fatigue, Failure and Damage Evolution, Volume 3, 2021, Conference Proceedings of the 2020 Annual Meeting of Society for Experimental Mechanics. https://doi.org/10.1007/978-3-030-60959-7_16.

Teaching Experience

- **ENGN0030**: Introduction to Engineering. 2016 Fall, 2020 Fall, 2021 Spring
- **ENGN0031**: Honor Introduction to Engineering. 2017 Fall, 2018 Fall, 2019 Fall
- **ENGN0040**: Dynamics and Vibration. 2019 Spring
- **ENGN1300**: Structural Analysis. 2017 Spring
- **ENGN0720**: Thermodynamics. 2016 Spring

Acknowledgements

I would like to express my greatest gratitude to my advisor, Prof. Kyung-Suk Kim, for his untiring support and enlightening advice during my graduate study. I was lucky that Prof. Kim accepted me, who had no background in mechanics at that time, as a master's student to conduct research in his group. Then, I am grateful for his tremendous trust to take me, who still almost knew nothing about mechanics, as a Ph.D. student. During my graduate study, Prof. Kim is not only teaching me how to conduct fundamental research but also how to understand experimental and computational mechanics in-depth rather than just become operational, by inspiring everyday storytelling on the broad history of Mechanics and beyond. This 6-year experience in his group has shaped me firmly not to fear any difficulties and challenges in future research and life.

Second, I would also like to extend my thanks to Prof. Rodney J. Clifton for valuable suggestions and discussions on my research. It is my great honor to work in such a prestige Plate Impact Lab at Brown. I would like to thank Prof. Huajian Gao, Prof. Pradeep Guduru, and Prof. George Karniadakis, who generously spend their time reading my thesis and offering helpful suggestions. I also want to thank the entire faculty of Engineering, Applied Math, Computer Science, and many other departments at Brown University for providing the wonderful education with freedom.

Third, sincere appreciation is extended to everyone who has been working in the same labs with me through many years, especially Prof. Ruike Zhao, Prof. Ruizhi Li, Dr. Tong Jiao, Dr. Mrityunjay Kothari, Dr. Alexander Landauer, Catherine Machnicki, Siyuan

Song, Xincheng Wang, and Jiahao Wei. The funding resources from ONR, machine shop, and computing resources provided by Brown University are also appreciated.

Finally, I would like to thank my parents for their support and encouragement during my pursuit of Ph.D. degree in the United States, and for their upbringing. Also, I would like to thank all my friends who supported and accompanied me throughout my life.

Table of Contents

Curriculum Vitae ..... **IV**

Publications ..... **IV**

Teaching Experience ..... **V**

Acknowledgements ..... **VI**

List of Figures ..... **XII**

Chapter 1 Introduction **1**

1.1 Brief overview on segmented block copolymers 1

1.2 Mechanical behaviors of polyurea 3

1.3 Structural properties of polyurea 4

1.4 Physics-informed and physics-based data-driven deep learning approaches in Solid Mechanics 6

1.5 Outline of the dissertation 8

Chapter 2 A deep learning framework to inversely determine cohesive parameters from dynamic big-data-generating experiments **10**

2.1 Introduction 10

2.2 Methodology 13

2.2.1 Big-data-generating experiments with Dynamic Line-Image Shearing Interferometry (DL-ISI) 13

2.2.2 Dataset preparation from FEM simulations 14
2.2.3 Convolutional neural network (CNN) 16
2.3 Results 17
2.3.1 Training and validation 19
2.3.2 Prediction on cohesive parameters and fracture toughness 20
2.4 Discussions 23
2.4.1 How much training data do we need? 23
2.4.2 The sensitivity of DL-ISI fringe image on prediction performance 27
2.5 Conclusions 29
Chapter 3 Dynamic fracture of a hierarchically nanostructured copolymer: A deep-learning analysis of big-data-generating experiment 30
3.1 Introduction 30
3.2 Dynamic Line-Image Shearing Interferometer (DL-ISI) 33
3.3 Experiments 37
3.3.1 Design of polyurea specimen with mid-plane crack 37
3.3.2 Streak-camera triggering system design 40
3.3.3 Plate impact experiments 41
3.3.4 Numerical simulations 43
3.4 Results and discussions 44
3.4.1 DL-ISI fringes 45
3.4.2 Physics-based DL-ISI fringe inpainting with Conditional Generative Adversarial Nets (cGAN) 49

3.4.3 Cohesive parameters and dynamic fracture toughness of polyurea 55

3.5 Conclusion 61

Appendix 3.A Linear elastic fracture mechanics (LEFM) estimation of dynamic fracture toughness 63

Appendix 3.B Detailed cGAN model 64

Appendix 3.C Train and predict performance of CNN model on the polyurea FEM dataset 65

Appendix 3.D DL-ISI fringe sensitivity on the detailed cohesive laws 67

Chapter 5 Nanophase fragmentation and self-healing of a block copolymer under deformation: *in-situ* AFM experiments and mesoscale simulations..... 68

4.1 Introduction..... 68

4.2 Experiments 72

4.2.1 *in-situ* AFM loading device with displacement invariance control 72

4.2.2 Polyurea thin film synthesis..... 74

4.2.3 Digital Image Correlation (DIC) analysis of the *in-situ* loading system 75

4.2.4 AFM tapping-mode imaging of polyurea nanophases under stress relaxation 77

4.3 Simulation methods 79

4.3.1 Modeling of self-assembly morphology from Dissipative Particle Dynamics (DPD) 79

4.3.2 Potential switch for the nanodomain evolution process 84

4.4 Results and Discussions 87

4.4.1 Strain induced anisotropic hard-domain coarsening in equilibrium morphologies 87

4.4.2 Nanophase fragmentation and self-healing processes during stress-relaxation at fixed strains 90

4.4.3 Load carrying capacities between hard and soft domains during tensile deformation 99

4.5 Conclusions 104

Chapter 6 Conclusions and Perspectives 105

5.1 Concluding remarks 105

5.2 Outlook for future research 107

Reference 105

List of Figures

Figure 1.1 (a-b) Schematics of polyurea polymerization of 4,4'-methylene diphenyl diisocyanate (MDI) and polytetramethylene oxide-di-p-aminobenzoate (Versalink P-1000; Air Products). Chemical structure of bidentate hydrogen bonding between urea linkages to form hard segments. Soft segments arise from the repeating unit of poly(tetramethylene oxide). (c) 500 ×500 nm AFM tapping-mode phase image of polyurea indicating bright regions for hard segments and dark for soft domain. 2

Figure 1.2 Schematics of three deep learning approaches based on available physics and data. 7

Figure 2.1 A deep learning framework to inversely determine cohesive parameters from dynamic big-data-generating experiments. (a) The linear traction-separation cohesive laws with three parameters ($\sigma c, \delta c$, and δf). (b) Finite element simulations with interfacial cohesive laws. (c) The Dynamic line image shear interferometry (DL-ISI) fringes are generated from FEM. The horizontal axis represents spatial information, while the vertical axis represents temporal information. (d) A convolutional neural network (CNN) is composed of two convolutional layers, two max-pooling layers, one flatten layer, and one hidden layer for two outputs ($\sigma c, \delta f$). (e) The experimental DL-ISI fringes were generated from the streak camera system. (f) Dynamic plate impact experiments with DL-ISI setups. 13

Figure 2.2 (a) Summary of the CNN architecture, which consists of two blocks of convolutional layers with kernel size 3×3, max-pooling layers with kernel size 2×2, flatten layer, fully connected layer with 8 neurons, and output layer. (b) The Mean Absolute Percentage Error (MAPE) of σc, and δf for 5 different CNN architectures. The notation F: $n1/n2$ means the number of filters of the first and second convolutional layer is $n1$, and $n2$. The notation K: $n3$ means the kernel

size on the convolutional layer is $n3 \times n3$. The error bar represents the standard deviation of 4 independent training procedures. 18

Figure 2.3 The Mean Absolute Percentage Error (MAPE) of training and validation datasets as a function of train epoch for (a) σc, and (b) δf with total number of 961 FEM datasets. 19

Figure 2.4 Prediction preformation (True values Vs Predictions) of cohesive parameters on training datasets for (a_i) σc, and (a_{ii}) δf, and testing datasets for (b_i) σc, and (b_{ii}) δf. 21

Figure 2.5 (a) Predicted and true values of cohesive parameters ($\sigma c, \delta f$) for 12 randomly selected fringe images in the test dataset. (b) Fringe images, predicted cohesive parameters and toughness, true values, and errors for 4 fringe images labeled in (a). The prediction errors larger than 2% are labeled in red and errors smaller than 2% are labeled in green. 22

Figure 2.6 The Mean Absolute Percentage Error (MAPE) of σc and δf as a function of total FEM dataset size. The error bar represents the standard deviation of 4 independent training procedures. 24

Figure 2.7 The Mean Absolute Percentage Error (MAPE) of (a) σc and (b) δf as a function of dataset size with and without transfer learning. The error bar represents the standard deviation of 4 training procedures. 26

Figure 2.8 The fringe images for the case with cohesive parameters $\boldsymbol{\sigma c = 200 MPa}$ and $\boldsymbol{\delta f = 0.052 mm}$ from 4 different image shear distance $\boldsymbol{\Delta x}$; (b) The Mean Absolute Percentage Error (MAPE) of $\boldsymbol{\sigma c}$ and $\boldsymbol{\delta f}$ as a function of image shear distance $\boldsymbol{\Delta x}$. The error bar represents the standard deviation of 4 independent training procedures. 28

Figure 3.1 Optical schematics of dynamic line-image shearing interferometer (DL-ISI) in the plate impact experiment. The black solid line represents the DL-ISI optical

circuits, the red solid line represents the optical triggering circuits for the streak camera system. SL represents the spherical Lens; M represents the mirror. 34

Figure 3.2 Schematics of two beams reflected from the front surface and rear surface of a glass plate with thickness t and a small tilt angle δ. 36

Figure 3.3 (a) Injection molding setup to mold polyurea with a sharp mid-plane crack. (b) Polyurea specimen with a mid-plane crack. 38

Figure 3.4 Time-displacement diagram for symmetric impact on a specimen with a mid-plane crack. 39

Figure 3.5 (a) Delay triggering setup for the streak camera system. (b) Triggering sequence design. 41

Figure 3.6 Raw experimental DL-ISI fringe image measured from Shot HJ2101. The time markers correspond to those in **Fig.3.4.**..... 46

Figure 3.7 (a) Smoothed experimental DL-ISI fringe image; (b) Computational DL-ISI fringe image from FEM with a prefect-bonded cohesive law; (c) Computational DL-ISI fringe image considering surface warping effect. 48

Figure 3.8 Schematics of the cGAN model consisted of a generator with U-NET architecture and a discriminator with PatchGAN architecture for the physics-based DL-ISI fringe inpainting. 50

Figure 3.9 Training performance of the cGAN model as a function of train epoch. 52

Figure 3.10 Input fringe images, ground-truth fringe images, predicted fringe images, and the normalized L2 errors of two randomly selected input images in the test dataset after 200 epochs of training. 53

Figure 3.11 Fringe inpainting of experimental fringe image with initial fringe padding from pre-trained cGAN with 200 epochs..... 54

Figure 3.12 Correlation coefficients contour between the experimental fringe and 961 FEM fringes in the dataset. The cohesive parameters with error bar determined

from bivariate normal distribution are marked in yellow. The dynamic fracture toughness is marked in blue dotted line with shaded error bar. The CNN predictions with error bars are marked in green. 56

Figure 3.13 (a) Inpainted experimental fringe; (b) FEM fringe generated from FEM simulation with predicted cohesive parameters of $\sigma c = 294.03MPa$ and $\delta f = 0.0823mm$. The crack tip positions are labeled in green dots. 58

Figure 3.14 Fractography for Shots HJ2101. 60

Figure 3.15 High dynamic fracture toughness of polyurea at a high crack-tip loading rate plotted on an Ashby diagram (Ashby, 2012). 61

Figure 3.C.1 The Mean Absolute Percentage Error (MAPE) of training and validation datasets as a function of train epoch for (a) σc, and (b) δf with total number of 961 FEM datasets. 65

Figure 3.C.2 Prediction preformation of cohesive parameters on training datasets for (a_i) σc, and (a_{ii}) δf, and testing datasets for (b_i) σc, and (b_{ii}) δf. 66

Figure 3.D.1 DL-ISI fringe images from FEM simulations with 3 different cohesive laws: bilinear, trapezoid, and exponential laws with the same fracture energy. 67

Figure 4.1 Schematics of *in-situ* AFM loading device with displacement invariance control. 73

Figure 4.2 Sequential AFM topography images of scan size $10\mu m \times 10\mu m$ of a PU-1000 sample under tension in the vertical direction with tensile strains, (a_i) $\varepsilon = 0.32\%$ and (a_{ii}) $\varepsilon = 0.65\%$. The displacement plots obtained from DIC for horizontal (b_i) and vertical (b_{ii}) displacements. 76

Figure 4.3 (a) Schematics of *in-situ* AFM tapping-mode phase imaging of polyurea thin film under symmetric displacement $u(t)$. PSPD is the abbreviation of Position-sensitive Photo Diode; TMPI is the abbreviation of Tapping Mode Phase

Imaging; ADIS is the abbreviation of Displacement Invariance Sight. (b) Multi-step loading history from rapid loading to equilibrium through stress relaxation. The blue points represent the morphologies right after rapid loading; the red points represent the equilibrium morphologies at each fixed strain $\varepsilon(t)$. 78

Figure 4.4 (a) Coarse-grained bead mapping scheme of polyurea; (b) The chain distribution in the built polydisperse model with PDI=1.52; the equilibrium morphology for (c) polydisperse and (d) monodisperse model after DPD simulation; (e) the radial distribution functions $g(r)$ of the hard domains for these two models. 83

Figure 4.5 AFM tapping-mode phase images of a polyurea thin film under various strains at equilibrium with scan size $1\mu m \times 1\mu m$ for (a) $\varepsilon = 0\%$, (b) $\varepsilon = 20\%$, (c) $\varepsilon = 78\%$, (d) $\varepsilon = 110\%$, (e) $\varepsilon = 200\%$, and (f) $\varepsilon = 264\%$. The loading direction is indicated by the black arrow. The image-autocorrelation of each phase image with size $500nm \times 500nm$ is plotted. Distinct long-range peaks in autocorrelation images are indicated by red arrows. 88

Figure 4.6 Anisotropic domain size evolution in the stretch and transverse directions at various strains identified by image autocorrelation. 90

Figure 4.7 *in-situ* AFM tapping-mode phase images of a polyurea thin film under stress-relaxation process at various fixed strains for (a) $\varepsilon = 5\%$, (b) $\varepsilon = 15\%$, (c) $\varepsilon = 20\%$, (d) $\varepsilon = 40\%$, (e) $\varepsilon = 60\%$, (f) $\varepsilon = 78\%$, (g) $\varepsilon = 110\%$, (h) $\varepsilon = 130\%$, and (i) $\varepsilon = 200\%$. The loading direction is indicated by the black arrow. The unit of time is minute. The autocorrelation image of each phase image is plotted in the left of the second row, and the 2D FFT image is plotted in the right. Images due to material drifting are marked with dotted squares..... 93

Figure 4.8 Two-way scans of *in-situ* AFM tapping-mode phase images of a polyurea thin film under stress-relaxation process from 0 to 12 mins at various fixed strains for (a) $\varepsilon = 20\%$, (b) $\varepsilon = 50\%$, (c) $\varepsilon = 100\%$, and (d) $\varepsilon = 200\%$. The loading direction is indicated by the black arrow. The unit of time is minute. Each slow-

scan direction is indicted on top of each scan. Images due to material drifting are marked with dotted squares. 96

Figure 4.9 The time variation of (a) mean value of $\mathfrak{I}$ tensor, $\mathfrak{I}mean$; (b) deviatoric value of $\mathfrak{I}$ tensor, $\mathfrak{I}dev$; and (c) principal axial rotation of $\mathfrak{I}$ tensor, θp, for the FFT images of *in-situ* AFM tapping-mode phase images with one-way scans of 4 different strains selected in **Fig.4.7**..... 98

Figure 4.10 The time variation of (a) mean value of $\mathfrak{I}$ tensor, $\mathfrak{I}mean$; (b) deviatoric value of $\mathfrak{I}$ tensor, $\mathfrak{I}dev$; and (c) principal axial rotation of $\mathfrak{I}$ tensor, θp, for the FFT images of *in-situ* AFM tapping-mode phase images with two-way scans of 4 different strains in **Fig.4.8**..... 99

Figure 4.11 (a) Morphologies of polyurea at different strains under tensile deformation from mesoscale simulation. The red beads represent the soft domains, and the blue beads represent the hard domains. The stretch direction is indicated by the black arrow. (b) 2D order parameter ϕ as a function of 8 strains in (a)..... 101

Figure 4.12 Total stresses in soft and hard domains along the (a) stretch direction, and (b) transverse direction. 103

List of Tables

Table 2.1 Average Mean Square Loss (MSE) and MAPE for σc, δf, and G on train and test datasets. 21

Table 3.1 Summary of experimental results. h is the thickness of the flyer, H is the thickness of the specimen with a mid-plane crack, $V0$ is the impact speed of projectile, θt is the tilt angle, $\sigma 0$ is the normal stress, Δc is the crack growth length..... 44

Table 3.2 DL-ISI parameters in HJ2101 44

Table 3.3 Cohesive parameters predictions from the correlation and CNN methods..... 57

Table 3.B.1 Detailed U-Net Generator architecture..... 64

Table 3.B.2 Detailed PatchGAN Discriminator architecture..... 64

Table 4.1 Coarse-grain simulation potential parameters for polyurea 86

Chapter 1

Introduction

1.1 Brief overview on segmented block copolymers

Over the past decades, segmented block copolymers such as polyurea and polyurethane have been extensively utilized as protective coating materials owing to their fast reactivity for casting, relative moisture insensitivity, and failure resistance under mechanical loading. More recently, polyurea has been further developed as high-toughness nanocomposites to be used under extreme loading conditions (Amini et al., 2010; Jiao and Clifton, 2014; Kim et al., 2021). In segmented block copolymers, the thermodynamically incompatible components are linked by primary covalent bonds respectively, which produces unique microphase separation morphology. This phase morphology is primarily governed by the parameters, χN, f_A, and f_B, where χ is the Flory-Huggins parameter (Flory, 1942; Huggins, 1941), N the degree of polymerization, and f_A, f_B the volume fractions of components A and B (Young and Lovell, 2011). In addition, strong bidentate hydrogen bonds are formed between two neighboring Urea linkages as observed from Fourier transform infrared spectroscopy (FT-IR) (Li et al., 2019; Yilgor et al., 2002), which facilitates the microphase separation process. The bidentate hydrogen bond energy was calculated as 58.5 kJ/mol from the quantum-mechanical calculation (Yilgor et al., 2002), which is four times higher than the energy of monodentate hydrogen bond.

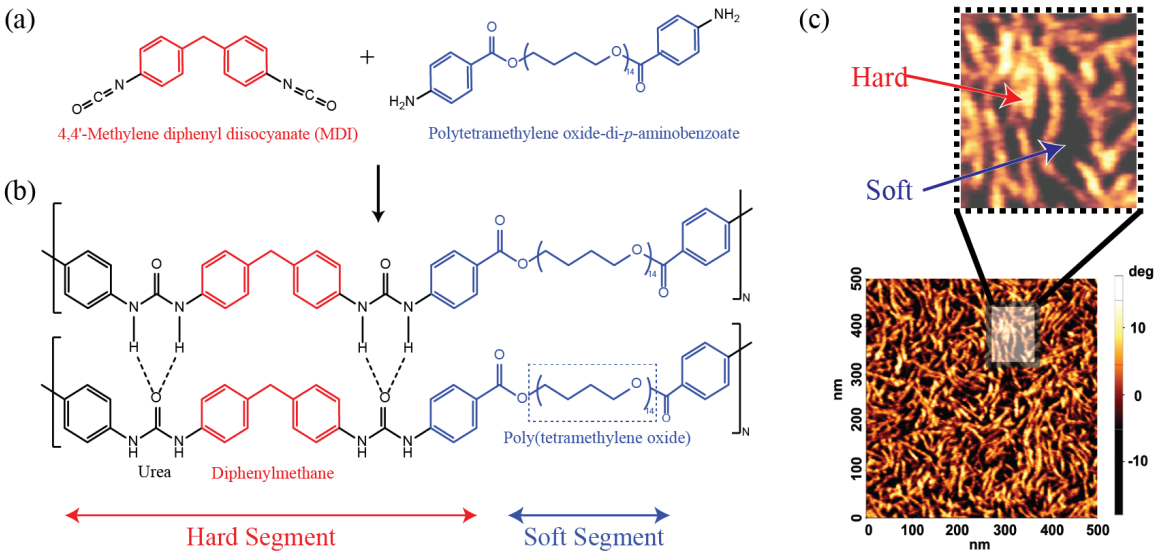

Figure 1.1 (a-b) Schematics of polyurea polymerization of 4,4'-methylene diphenyl diisocyanate (MDI) and polytetramethylene oxide-di-p-aminobenzoate (Versalink P-1000; Air Products). Chemical structure of bidentate hydrogen bonding between urea linkages to form hard segments. Soft segments arise from the repeating unit of poly(tetramethylene oxide). (c) 500 ×500 nm AFM tapping-mode phase image of polyurea indicating bright regions for hard segments and dark for soft domain.

As shown in **Fig.1.1**, during linear polymerization of polyurea, hard diisocyanate and soft diamine segments self-assemble into unique dual-phase bicontinuous nanostructures consisting of hard arms with high aspect ratio. These hard-phase segments have glass transition temperature T_g higher than room temperature, and they are dispersed in a continuous soft rubbery medium, as observed in Atomic Force Microscopy (AFM) tapping-mode phase images (Das et al., 2007; Grujicic et al., 2014a; Kim et al., 2021; Pangon et al., 2014; Wisse et al., 2006). The hard-phase arms have diameters of ~15nm and lengths of several hundred nanometers, and a high-resolution AFM tip of 2nm radius could reveal details of the nanostructure assemblies through tapping-mode imaging within

submicron observation window. The polyurea has unusually high dynamic toughness compared to other typical polymeric materials that exhibit embrittlement under high strain rate loading; however, so far, the structural-property relationship between the nanophase separation morphology and the corresponding dynamic toughening mechanisms at such a high rate of loading has not been revealed. Here, we first review current understandings of mechanical behaviors of polyurea under quasi-static and dynamic loading.

1.2 Mechanical behaviors of polyurea

Several experiments (Bogoslovov et al., 2007; Jiao and Clifton, 2014; Roland et al., 2007; Sarva et al., 2007; Shim and Mohr, 2009; Yi et al., 2006) under widespan of strain rates from quasi-static to extreme rate $\sim 10^6 \mathrm{s}^{-1}$ have been conducted to characterize the mechanical properties of polyurea. From tensile experiments (Yi et al., 2006) and compression experiments (Sarva et al., 2007) in a wide range of strain rate from $0.001 \mathrm{s}^{-1}$ to $10^4 \mathrm{s}^{-1}$, Boyce and colleagues found a strong hysteresis and rate-dependent behavior of polyurea PU1000 and suggested the rubbery material enters glassy state when the strain rate is larger than $10^2\ \mathrm{s}^{-1}$. In contrast, Roland et al. (Roland et al., 2007) found there is no clear indication of such glassy transition from their tensile experiments of the same polyurea product. This discrepancy is probably due to the sensitivity of chemical stoichiometry on mechanical properties. Only a 5% change in stoichiometry caused an enormous change in mechanical behaviors (Roland et al., 2007). Roland et al. measured the material toughness of the polyurea around $58 MJ/m^3$ (material toughness is defined as the total strain energy to failure during tensile test), which is independent of stoichiometry. To study the mechanical response of polyurea under an extreme high strain rate, Time-

Temperature Superposition (TTS) principle was proposed to extrapolate desired data for polyurea within frequency range from 10^{-5} to 10^{10} Hz (Jia et al., 2016; Zhao et al., 2007).

Regarding experiments with extreme strain rate, Bogoslovov and colleagues (Bogoslovov et al., 2007) observed the polyurea entered the glassy state during a projectile impact loading with the mean strain rate ~$10^5 \mathrm{s}^{-1}$. This strain rate is one order of magnitude higher than the glass transition frequency measured from dielectric relaxation spectroscopy at the impact temperature (Castagna et al., 2012; Roland and Casalini, 2007). Jiao et al. (Jiao and Clifton, 2014) found the shear resistance of polyurea at strain rate $10^5 \mathrm{s}^{-1}$ is unremarkably comparable to high strength steel from the pressure shear plate impact experiments.

Regarding the fracture toughness of polyurea, Zhu et al. (Zhu et al., 2009) measured the Mode I fracture toughness between polyurea/steel interface as $7kJ/m^2$ under quasi-static loading. Kim et al. (Kim et al., 2012) measured the fracture energy for E-glass/polyurea/steel joints as ~$350J/m^2$ at a peak strain rate of $10^7 \mathrm{s}^{-1}$. These findings help our understanding of the role of polyurea as a coating material. However, to our knowledge, so far, no research has been done to measure the dynamic fracture toughness of polyurea under an extremely high crack-tip loading rate.

1.3 Structural properties of polyurea

The unique bicontinuous phase morphology of polyurea is believed to have an influence on its superior mechanical behaviors under dynamic loading. Here, we review some current understandings of the structural evolution process from Atomic Force Microscopy (AFM),

and small- and wide-angle X-ray scattering (SAXS/WAXS) experiments. AFM Tapping-mode imaging is commonly used to directly observe the nanostructures of polyurea in equilibrium within submicron window (Castagna et al., 2012; Das et al., 2007; Grujicic et al., 2014a; Kim et al., 2021; Pangon et al., 2014; Wisse et al., 2006). Some key structural information such as the degree of phase separation, average interdomain spacing and domain size could be extracted from AFM images after correcting the tip-radius effect. However, few research has been done to study the phase-morphology evolution under deformation due to experimental difficulties. To our knowledge, there is no research to directly observe the *in-situ* hard domain evolution process as well as the relaxation process of polyurea. *In-situ* SAXS/WAXS have been performed by Rinaldi et al. (Rinaldi et al., 2011) and Choi et al. (Choi et al., 2012) to study the micro-structural evolution processes of polyurea under deformation. They found that average hard domain spacing in the stretch direction is reducing at the strain ~0.4 under the quasi-static loading. Based on this observation, they hypothesized that the hard domains disassociated at this strain, and this dissociation-breakage is an important mechanism of energy dissipation during tensile loading. However, the current understanding of the nanodomain evolution process during the deformation is still limited due to the lack of direct observation on the domain evolution process.

1.4 Physics-informed and physics-based data-driven deep learning approaches in Solid Mechanics

Recent advances in deep learning (LeCun et al., 2015) play a significant role in engineering applications and technologies like computer vision (Krizhevsky et al., 2012), natural language processing (Hinton et al., 2012), etc. In principle, the deep learning approach uses a multi-layer neural network structure to learn the nonlinear mapping between inputs and ground-truth labels of the training dataset. Then, a well-trained neural network can effectively predict labels from a new dataset. Depending on how large a dataset we could obtain and how much we know about embedding physics, the deep learning approaches can be categorized into three categories as shown in **Fig.1.2**: (I) physics-informed learning method (Raissi et al., 2019), (II) physics-based data-driven method, and (III) purely data-driven method. In engineering and physics, the first two approaches are typically used. In the first category, a concrete physics-based problem is usually governed by well-defined physical laws such as governing partial differential equations (PDEs) in solid and fluid mechanics. Moreover, the physical laws themselves provide valuable a priori temporal or spatial information, which can be integrated into neural networks during training. To this end, a physics-based deep learning approach called physics-informed neural networks (PINNs) (Raissi et al., 2019) has been proposed. This breakthrough framework has paved a new pathway to solving physical-law-governed forward and inverse problems without massive data-driven training. For example, PINNs have been successfully applied to inversely determine the material inhomogeneity in nonlinear solids (Zhang et al., 2020).

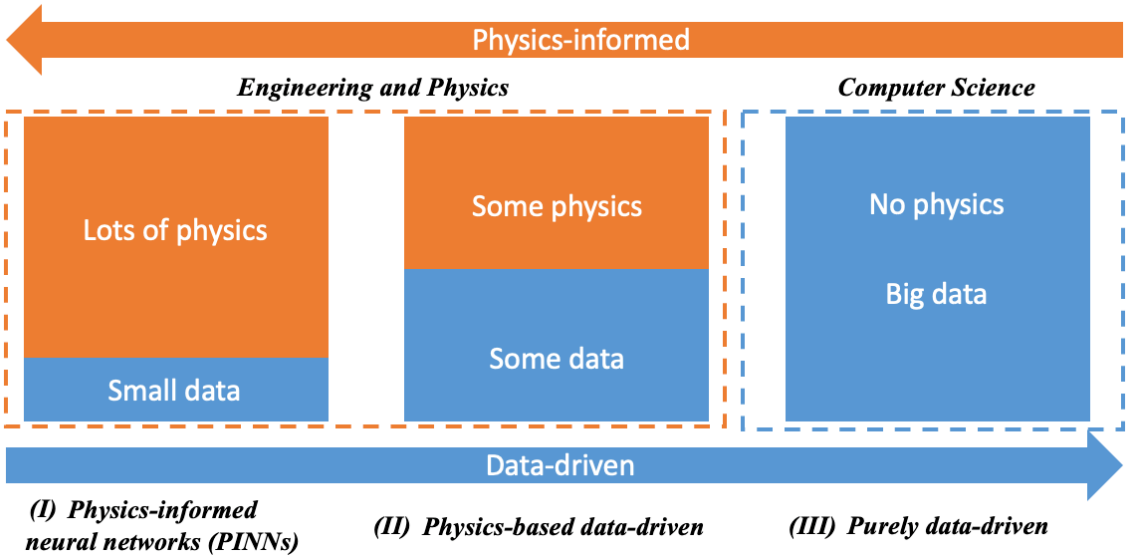

Figure 1.2 Schematics of three deep learning approaches based on available physics and data.

On the other hand, the physics-based data-driven method is employed when a problem is too complex to be concretely described by PDEs, but the training dataset can be relatively easily obtained from massive computational simulations like Finite Element Analysis (FEA) or Molecular dynamics (MD) within a reasonable time frame. For example, when the analytical solution is not available, machine learning can accurately predict the fracture toughness for complex structures from a neural network pre-trained with an FEM training dataset (Liu et al., 2020, 2021). Physics-based data-driven methods can also help inversely obtain the local material stiffness distribution from the external measured displacement field through a conditional generative adversarial network (cGAN) (Ni and Gao, 2021).

In this thesis, the dynamic cohesive or interfacial constitutive behaviors on a nonlinear material could not be easily described by PDEs; however, recent advances in FEM can accurately simulate the dynamic impact process with given cohesive laws.

Therefore, we adopted the physics-based data-driven approach to preparing the FEM dataset to train a neural network that can inversely determine the cohesive parameters. Most of the current physics-based data-driven methods in solid mechanics for forward and inverse problems are limited to a computational framework, and we hope this thesis demonstrates the power of deep learning used for nontrivial inverse problems in experimental mechanics.

1.5 Outline of the dissertation

The dissertation will focus on understanding the dynamic behaviors of a hierarchically nanostructured copolymer, the polyurea, through multi-scale big-data-generating experiments and simulations. The thesis consists of five chapters and is organized as follows.

In Chapter 1, we overview the basics of the copolymer, polyurea's structural properties, and its mechanical behaviors over different strain rates. A brief review of deep learning and its application in solid mechanics is also included.

In Chapter 2, we propose a convolutional-neural-network (CNN)-based deep-learning framework to inversely determine the accurate interfacial cohesive parameters of dynamic-fracture processes through dynamic big-data-generating experiments. We select determining dynamic cohesive laws and dynamic interfacial fracture toughness in a bi-material specimen with a polyurea coating in the plate impact experiments as a computational example to demonstrate the framework.

In Chapter 3, we quantitatively measure the dynamic fracture toughness of polyurea with the framework proposed in Chapter 2 applied to a dynamic big-data-generating

experiment. First, we present our invention of Dynamic Line Image Shear Interferometry (DL-ISI) that can generate massive experimental data in one single experiment compared to conventional data collection methods in dynamic experiments. Then, we apply a state-of-art conditional generative adversarial net (cGAN) for physics-based experimental fringe inpainting. Finally, the fracture toughness of the polyurea under a high crack-tip loading rate is determined from the inpainted experimental fringe image.

In Chapter 4, we study why the polyurea exhibits unusually high dynamic toughening from a molecular level point of view. First, we present our design of a novel *in-situ* AFM tensile loading device that can provide a stationary observation sight with minimal drifting. Then, reported are the *in-situ* AFM-tapping mode-phase images of polyurea relaxation processes under tensile deformation made by the loading device. In addition, mesoscale coarse-grained molecular-dynamics (CGMD) simulations have been performed to assist the understanding of the phase evolution process under the deformation process.

Conclusions and future directions are summarized in Chapter 5.

Chapter 2

A deep learning framework to inversely determine cohesive parameters from dynamic big-data-generating experiments

2.1 Introduction

Constitutive responses of interfaces, which are typically characterized by Cohesive Zone Models (CZMs), have been widely used to analyze complicated fracture processes in linear and nonlinear materials over the past several decades (Barenblatt, 1983; Dugdale, 1960; Tvergaard and Hutchinson, 1996; Xu and Needleman, 1993). In general, CZM employs a physical traction-separation law to describe the cohesive behavior between similar or dissimilar interfaces. For example, as shown in **Fig.2.1(a)**, a bilinear elastic traction-separation law can be effectively described by three cohesive parameters, the maximum interfacial stress σ_c and its separation δ_c, and the failure separation δ_f. Since its development, CZM has been successfully used to describe various fracture and friction problems such as void growth in metals (Tvergaard and Hutchinson, 1996), polymer crazing (Hong et al., 2009; Hong and Kim, 2003), and single and multi-asperity friction

(Kim et al., 1998; Li and Kim, 2008, 2009). Therefore, it is crucial to develop rigorous experimental techniques to accurately measure the cohesive parameters, which can be further implemented in Finite Element Analysis (FEA) or micromechanics models to understand the fracture and friction behaviors for the bulk or interfaces of composite materials. Obtaining cohesive laws from experiments is usually an inverse problem. Practically, experimentists first measure the load-displacement curves at the boundary of a specimen (Bazant, 2002) or obtain the whole deformation field using optical methods such as moiré interferometry (Mohammed and Liechti, 2000). Then, optimization algorithms like the steepest descent method are employed to find the optimal cohesive parameters iteratively. However, using this approach to obtain accurate cohesive parameters is challenging. The non-uniqueness of the inverse problem may lead to finding parameters in local minima, which can also depend on the optimization algorithms.

Recent advances in machine learning, especially deep learning, provide a powerful method to solve inverse problems in engineering and physics (Hsu et al., 2020; Sanchez-Lengeling and Aspuru-Guzik, 2018; Shi et al., 2020). In principle, the deep-learning approach uses a multi-layer neural network structure that can learn the nonlinear mapping between training dataset and pre-set labels or parameters (LeCun et al., 2015). Then, the pre-trained neural network can effectively predict parameters for the test dataset. In many cases, the prediction accuracy can surpass human performance (Krizhevsky et al., 2012). In the application of solving inverse problems in Solid Mechanics, deep learning has been successfully employed to extract the mechanical properties from instrumented indentation (Lu et al., 2020), obtain the local material stiffness distribution from the external measured displacement field (Ni and Gao, 2021; Zhang et al., 2020), or detect inhomogeneous

inclusion geometries in a nonlinear medium (Zhang et al., 2020). Regarding using deep learning to determine the cohesive laws inversely, recent studies (Ferdousi et al., 2021; Su et al., 2021) have used load-displacement curves at the boundary of the specimen to train a deep dense-layer neural-net architecture. However, such quasi-static load-displacement measurement technique cannot be applied to dynamic experiments under extreme conditions like plate-impact experiments in which local strain rates exceed $10^6 s^{-1}$. At most, a laser interferometry technique was used to measure a time trace of displacements at a point to inversely determine the fracture toughness (Ravichandran and Clifton, 1989) based on analytical dynamic crack-tip solutions of Freund (Freund, 1972, 1973). However, such "one-point" measurement cannot accurately determine the interfacial properties like cohesive parameters. A new experimental technique that can generate a sufficient dataset in a single experiment is desired for deep learning to determine the cohesive parameters inversely. We defined such a high-throughput experiment as a big-data-generating experiment.

Therefore, in this chapter, we present a deep-learning framework that can inversely determine the accurate cohesive parameters in dynamic big-data-generating experiments. Here, we select determining dynamic cohesive laws and dynamic interfacial fracture toughness in a bi-material specimen in the plate impact experiment as a relevant example. The general deep learning framework is illustrated in **Fig.2.1**. The key components of the framework include: (I) a novel experimental technique to collect sufficient experimental data in a single experiment; (II) a computational simulation method to obtain a training dataset within a reasonable time; (III) a deep-learning algorithm that has the capability to train the network and validate the prediction.

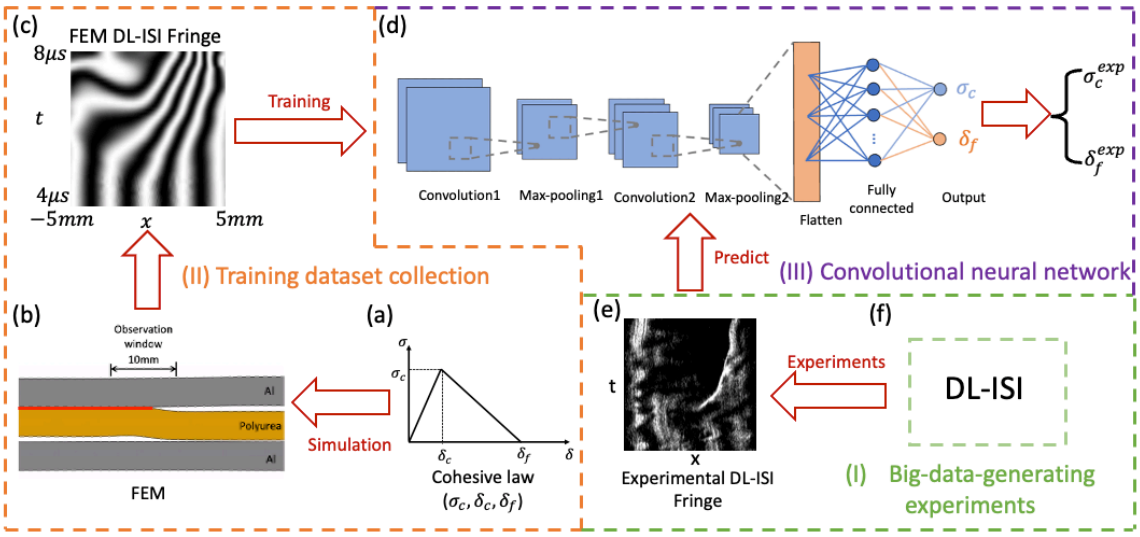

Figure 2.1 A deep learning framework to inversely determine cohesive parameters from dynamic big-data-generating experiments. (a) The linear traction-separation cohesive laws with three parameters (σ_c, δ_c, and δ_f). (b) Finite element simulations with interfacial cohesive laws. (c) The Dynamic line image shear interferometry (DL-ISI) fringes are generated from FEM. The horizontal axis represents spatial information, while the vertical axis represents temporal information. (d) A convolutional neural network (CNN) is composed of two convolutional layers, two max-pooling layers, one flatten layer, and one hidden layer for two outputs (σ_c, δ_f). (e) The experimental DL-ISI fringes were generated from the streak camera system. (f) Dynamic plate impact experiments with DL-ISI setups.

2.2 Methodology

2.2.1 Big-data-generating experiments with Dynamic Line-Image Shearing Interferometry (DL-ISI)

Our framework aims to train a neural network that can predict the cohesive parameters from the experimentally measurable dataset. For this purpose, we invented a Dynamic

Line-Image Shearing Interferometry (DL-ISI) with a streak camera system. The detailed design of DL-ISI and procedure of the plate impact experiments will be presented in **Chapter 3**. In brief, from each experiment, we obtain a full-field fringe (**Fig.2.1(e)**), where the horizontal axis represents the spatial information of displacement gradient along a line on the rear surface of the sample, and the vertical axis represents the temporal information within a few microseconds. Compared to conventional laser interferometry, each fringe image presents a massive dataset covering the spatial and temporal information of crack initiation and growth. With this informative dataset in one fringe image, accurate cohesive parameters can be extracted from a pre-trained neural network with an adequate FEM training dataset.

2.2.2 Dataset preparation from FEM simulations

Training a deep-learning neural network usually requires an adequate training dataset. In our case, the input variables would be a DL-ISI fringe image, and the output variables would be three cohesive parameters $(\sigma_c, \delta_c, \delta_f)$ of a bilinear interfacial cohesive law (**Fig. 2.1(a)**). Since the dynamic crack initiation and growth is most relevant to the fracture toughness of the interface, $G = \frac{1}{2}\sigma_c\delta_f$, we consider the two cohesive parameters (σ_c, δ_f) as the output variables and set $\delta_c = 0.2\delta_f$ for simplicity. The relevant parameter space of the output variables is selected as $\sigma_c \in [100,300]$MPa, $\delta_f \in [0.01,0.1]$mm, which yields the interfacial fracture toughness $G \in [500, 15000]\mathrm{J/m^2}$. This toughness parameter space covers the spall strength of homogeneous microcrack nucleation in the bulk material and the craze dimension estimated from postmortem fracture surfaces. Therefore, we think this parameter range is representative of the cohesive laws for the Al-Polyurea interface. The

parameter space is uniformly discretized into $m \times m$ intervals. Therefore, the total number of training samples is $M = (m+1)^2$. We chose $m = 9, 13, 19, 24, 30$, which yields $M = 100, 196, 400, 625, 961$ to explore the effect of the training dataset on the neural network performance.

Next, we carried out FEM simulations to obtain the training dataset, i.e., the computational fringes with the labeled cohesive parameters. The FEM simulations on plate impact experiments were performed by ABAQUS/Explicit 2017 package. As shown in **Fig. 2.1(b)**, a flyer made by Aluminum with a thickness of 2.22mm impacts a bi-material sample, which has a polyurea layer with a thickness of 2.22mm coated on an Al plate with a thickness of 2.22mm. The simulations were conducted under the 2D plane-strain condition. To reduce the effects of boundary waves on the surface motion, the simulation domain was chosen as the same size as the experimental samples, i.e., the length is 50mm. The impact speed of the flyer is defined as an initial condition of 100m/s. The left half portion of the interface is considered bonded with a cohesive law. Each cohesive law with two cohesive parameters (σ_c, δ_f) was implemented as a VUINTER subroutine in the simulation. The strain energy of polyurea can be expressed as, $\overline{W}(\overline{I_1}, J) = C_{10}(\overline{I_1} - 3) + f(J)$, where $f(J) = -A(J^{-N-1} - J^{-M-1})$ (Clifton and Jiao, 2015), where $\overline{I_1}$ is the invariant of the left Cauchy-Green tensor, and J is the volume ratio between the current and reference volumes. Here, $C_{10} = 150\text{MPa}$, $A = 858\text{MPa}$, $N = 6$, and $M = 3$, and the density of polyurea is 1070 kg/m^3. This instantaneous finite deformation constitutive law of polyurea represents the material characteristics well when simulating the spall experiments. Therefore, quasi-linear viscoelasticity was not considered in modeling the bulk behaviors of polyurea. Polyurea was modeled through a user subroutine VUMAT in ABAQUS. Since

the maximum local strain in the Al is less than 1%, Al was modeled as purely elastic material with Young's modulus $E_{Al} = 70GPa$, Poisson's ratio $\nu = 0.33$, and density 2700 kg/m^3. The gradient mesh was adapted where the mesh size around the crack tip is $50\mu m$. All solutions reported here are the final convergent solutions checked by mesh sensitivity tests. The average wall time of each simulation was 10s when running on a CPU with 24 cores. The total training dataset collection for 961 simulations took ~3 hours. After each simulation, the displacement profile along a line within 10mm observation window size at the middle of the target's rear surface was extracted. Then, displacement gradients along the line were calculated to plot corresponding computational DL-ISI fringe images based on the theoretical derivations in **Chapter 3**. Each simulated DL-ISI fringe image was then cropped into a time window of interest, i.e., the initial crack-tip opening period, and rescaled into 64×64 pixels for training. An example of a computational fringe image is shown in **Fig.2.1(c)**.

2.2.3 Convolutional neural network (CNN)

The recent development of convolutional neural network (CNN) has shown a solid capability to classify images into thousands of labels (Krizhevsky et al., 2012), which has an enormous impact on modern technology such as face recognition (Parkhi et al., 2015) and self-driving cars (Bojarski et al., 2016). Here, we adopted a CNN-based neural network to train our computational fringe images with labeled cohesive parameters. The network structure is illustrated in **Fig.2.1(d)**. The fringe images were first fed into a convolution layer with the rectified linear activation function (ReLU), followed by a conventional 2×2 max-pooling layer. The effects of the convolution kernel size and the number of

convolution layers were explored and discussed in **Section 2.4**. Then, the output was flattened and fed into a fully connected layer for two outputs σ_c, and δ_f, respectively. To validate and test the CNN network, the total dataset was randomly divided into 80% training dataset, 10% validation dataset, and 10% test dataset. The accuracy metrics in estimating cohesive parameters were represented by the Mean Absolute Percentage Error (MAPE) as,

$$MAPE = \frac{1}{N}\sum_{i=1}^{N} \left| \frac{y_i^{true} - y_i^{pre}}{y_i^{true}} \right| \times 100\%. \tag{2.1}$$

Where N is the number of the dataset, and y_i^{true}, y_i^{pre} are ground-true values and predicted values for the cohesive parameters. The CNN optimized the Mean Square Error (MSE) loss by using the Adam optimizer (Kingma and Ba, 2014) with the learning rate of 0.0001 for 2000 epochs on the open-source platform TensorFlow V2.5 (Abadi et al., 2016). The total training time for the dataset with 961 fringe images on an 8-core CPU is around 5 mins.

2.3 Results

In this section, we present the results of predictions for cohesive parameters (σ_c, δ_f) and fracture toughness G determined by the CNN architecture, which was trained by FEM fringe images. The optimized CNN architecture is summarized in **Fig.2.2(a)**. The architecture has two blocks of convolutional units. The first block has a convolutional layer with 8 filters with 3×3 kernel size, followed by a max-pooling layer with 2×2 kernel size and a batch normalization layer. The MAPEs of σ_c and δ_f predicted from 5 different CNN architectures are plotted in **Fig.2.2(b)**. As we can see, as the number of filters in the

first convolution layer increases from 4 to 8, the MAPEs reduce from around 2.5% to targeted 2.0%. Moreover, filters with 3× 3 kernel size have better prediction performance than with 5× 5 kernel size.

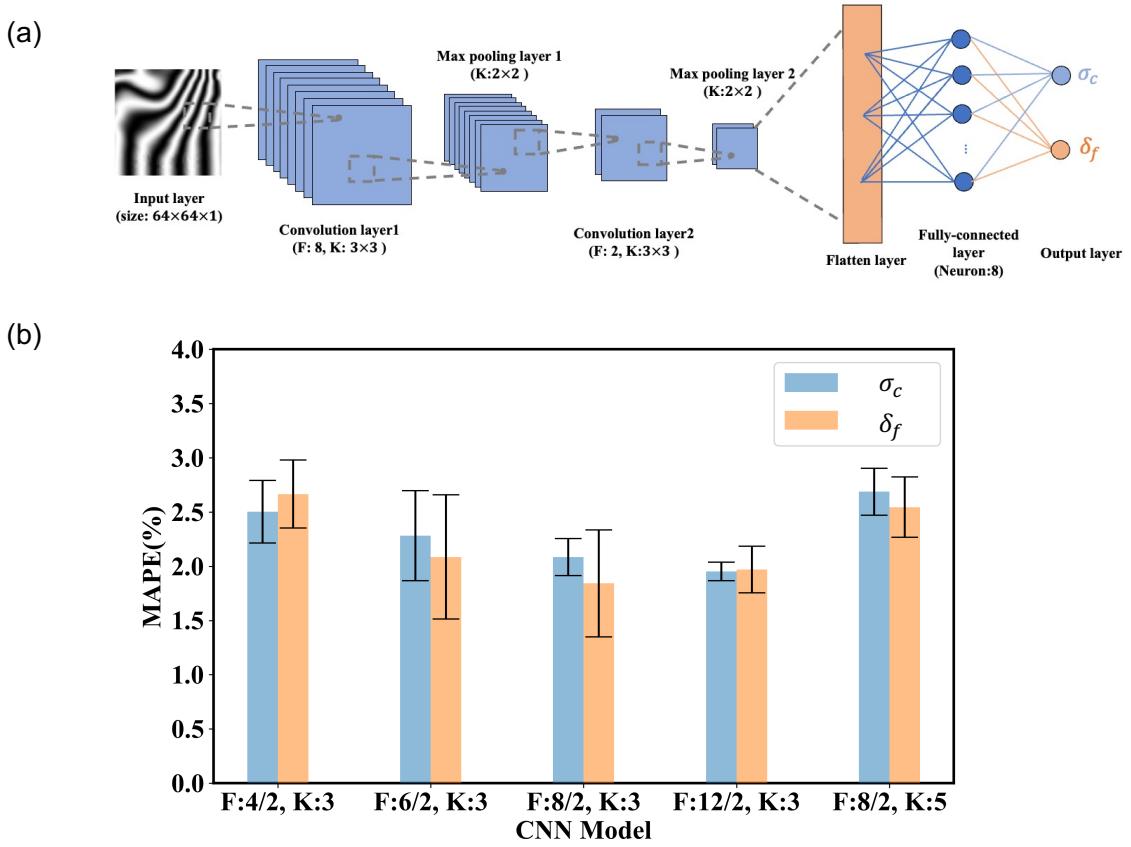

Figure 2.2 (a) Summary of the CNN architecture, which consists of two blocks of convolutional layers with kernel size 3 × 3, max-pooling layers with kernel size 2 × 2, flatten layer, fully connected layer with 8 neurons, and output layer. (b) The Mean Absolute Percentage Error (MAPE) of σ_c, and δ_f for 5 different CNN architectures. The notation F: n_1/n_2 means the number of filters of the first and second convolutional layer is n_1, and n_2. The notation K: n_3 means the kernel size on the convolutional layer is $n_3 \times n_3$. The error bar represents the standard deviation of 4 independent training procedures.

2.3.1 Training and validation

To validate the training process as well as prevent unexpected training issues such as overfitting, the MAPE of training and validation datasets for σ_c and δ_f as a function of the training epoch is plotted in **Fig.3(a)&(b)**, respectively.

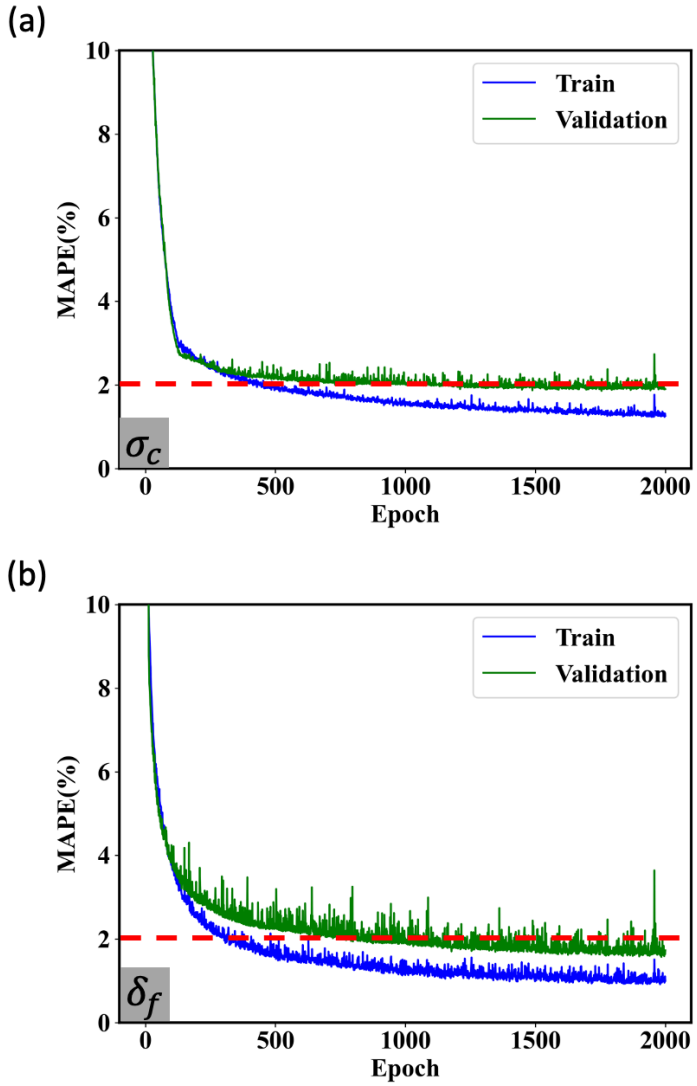

Figure 2.3 The Mean Absolute Percentage Error (MAPE) of training and validation datasets as a function of train epoch for (a) σ_c, and (b) δ_f with total number of 961 FEM datasets.

As we can see in **Fig.2.3**, the MAPEs of both training and validation datasets drop rapidly to 3% when the training epoch reaches ~250, which validates the effectiveness of the current architecture. The MAPEs of both σ_c and δ_f gradually decrease to targeted 2% as the training epoch increases. It is worth noting that the MAPE for validation datasets is slightly higher (~0.5%) than the train datasets. This discrepancy exists for all dataset sizes and CNN architectures we considered. It may be due to the limitation of fringe sensitivity to cohesive parameters. Therefore, decreasing the train dataset mesh to increase the train dataset size does not help. Nevertheless, the overall performance of the current CNN architecture with MAPE less than 2% has already suppressed many exiting inverse algorithms for cohesive parameter determinations for nonlinear materials.

2.3.2 Prediction on cohesive parameters and fracture toughness

The Mean Square Losses (MSE) and MAPEs of σ_c and δ_f are listed in **Table 2.1** on the train and test datasets to observe the CNN performance. After the training, the average MAPEs of σ_c, δ_f, and G on the test dataset for four independent training are 2.08%, 1.84%, and 2.05% correspondingly. To observe the prediction performance on individual case, the predicted and ground-truth cohesive parameters are plotted in **Fig.2.4(a)&(b)** for the training and testing datasets, respectively. The coefficients of determination (R^2) between predicted and true values were also calculated to illustrate the training and prediction performance. With the 2-block CNN architecture, the R^2 values on the training dataset are greater than 0.999 for both σ_c and δ_f. As we can see in **Fig.2.4(a$_i$)**, the predicted and true σ_c have more significant variations when $\sigma_c > 250MPa$ than the cases when $\sigma_c < 250MPa$. This is because, with larger σ_c, the crack will have a subtle growth, which yields

the fringe variations not as distinct as the cases with smaller σ_c. The R^2 values on the test dataset for both parameters are greater than 0.997, which illustrates that the current deep learning architecture can inversely identify the cohesive parameters from the given fringe images, and there is no overfitting on the training datasets.

Table 2.1 Average Mean Square Loss (MSE) and MAPE for σ_c, δ_f, and G on train and test datasets.

Description	σ_c		δ_f		G	
	Train	Test	Train	Test	Train	Test
MSE	0.0006	0.0031	0.0004	0.0025	NA	NA
MAPE (%)	1.599	2.085	1.380	1.842	1.459	2.049

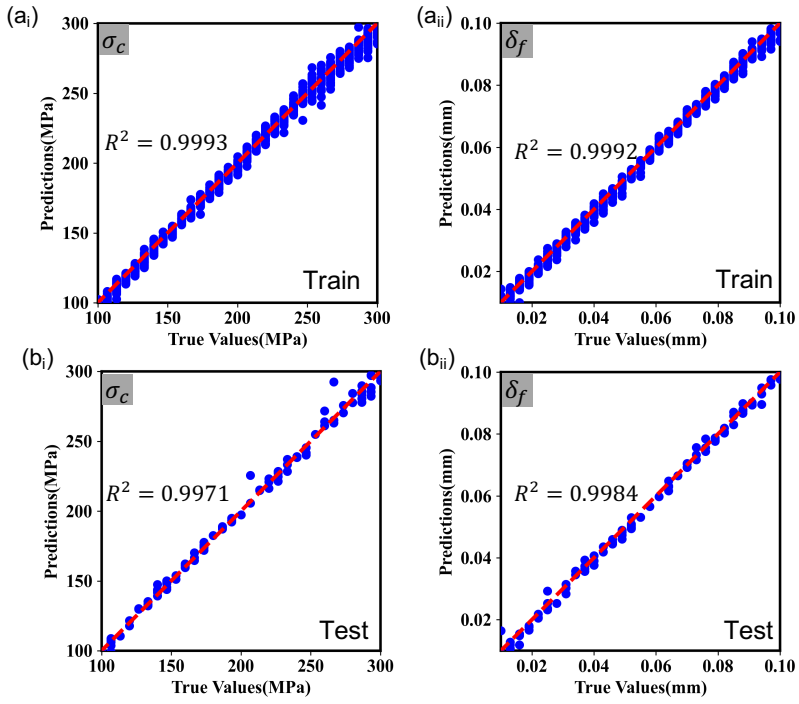

Figure 2.4 Prediction preformation (True values Vs Predictions) of cohesive parameters on training datasets for (a_i) σ_c, and (a_{ii}) δ_f, and testing datasets for (b_i) σ_c, and (b_{ii}) δ_f.

(a)

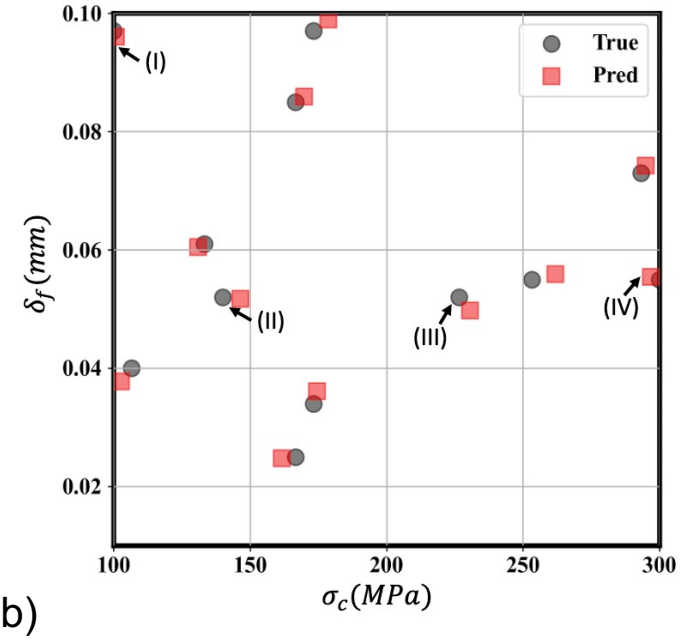

(b)

Fringe	$\sigma_c(MPa)$	$\delta_f(mm)$	$G(J/m^2)$
(I) 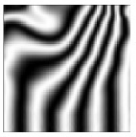	True: 100.00	True: 0.0970	True: 4850.00
	Pred: 100.87	Pred: 0.0960	Pred: 4841.76
	Error: 0.87%	Error: 1.03%	Error: 0.17%
(II) 	True: 140.00	True: 0.0520	True: 3640.00
	Pred: 146.49	Pred: 0.0518	Pred: 3794.09
	Error: 4.6%	Error: 0.38%	Error: 4.23%
(III) 	True: 226.66	True: 0.0520	True: 5893.16
	Pred: 230.63	Pred: 0.0498	Pred: 5742.69
	Error: 1.75%	Error: 4.23%	Error: 2.56%
(IV) 	True: 300.00	True: 0.0550	True: 8250.00
	Pred: 296.88	Pred: 0.0554	Pred: 8223.58
	Error: 1.04%	Error: 0.73%	Error: 0.32%

Figure 2.5 (a) Predicted and true values of cohesive parameters (σ_c, δ_f) for 12 randomly selected fringe images in the test dataset. (b) Fringe images, predicted cohesive parameters and toughness, true values, and errors for 4 fringe images labeled in (a). The prediction errors larger than 2% are labeled in red and errors smaller than 2% are labeled in green.

To visualize the prediction performance of the current CNN architecture, the predicted cohesive parameters compared with true values for 12 randomly selected fringe images from the test dataset are plotted in two-parameter spaces in **Fig.2.5(a)**. It is shown that most predictions overlap the true parameters with prediction errors of less than 2%. Among these 12 cohesive parameter pairs, the prediction performance and the fringe images of 4 pairs are presented in **Fig.2.5(b)**. As we can see, the fringe images look almost identical to human eyes, especially for Cases (I) and (IV). However, our CNN architecture has the capability to distinguish the fringe images to identify the cohesive parameters with prediction errors around 1%, which yields the prediction errors of interfacial toughness less than 0.5% (Case (I) and (IV)). For Case (II) and (III), one of the parameters has a prediction error greater than 4%. This error may be caused by the numerical noise of FEM with certain cohesive parameters. For example, there are some noises on the fringe image of Case (III). These noises can potentially affect the prediction of a single case. This result suggests that some noise reduction techniques are desired on the experimentally measured fringes to improve the prediction accuracy.

2.4 Discussions

2.4.1 How much training data do we need?

Obtaining sufficient and high-quality training datasets is crucial to train a CNN architecture to make accurate predictions. Now a question arises. How much FEM training data do we need to train our CNN architecture? Recall that we discretized the cohesive parameters into uniform intervals for training data generation in FEM. Ideally, we could reduce the interval

to generate a sufficient training dataset. However, if the interval is too small, the fringe image may not be sensitive enough to determine the cohesive parameters accurately. Here, we discuss the effects of training dataset size on prediction performance. The Mean Absolute Percentage Error (MAPE) of σ_c and δ_f as a function of total FEM dataset size is plotted in **Fig.2.6**. The training dataset size is 80% of the total dataset size M. Interestingly, the prediction error for δ_f is twice larger than the error for σ_c when dataset size $M < 200$. This result indicates that an insufficient training dataset could generate training bias for these two parameters. When $M > 400$, the MAPEs of both parameters have similar values, and they reduce steadily as M increase. A dataset of 961 FEMs could provide the targeted prediction with MAPEs less than 2%.

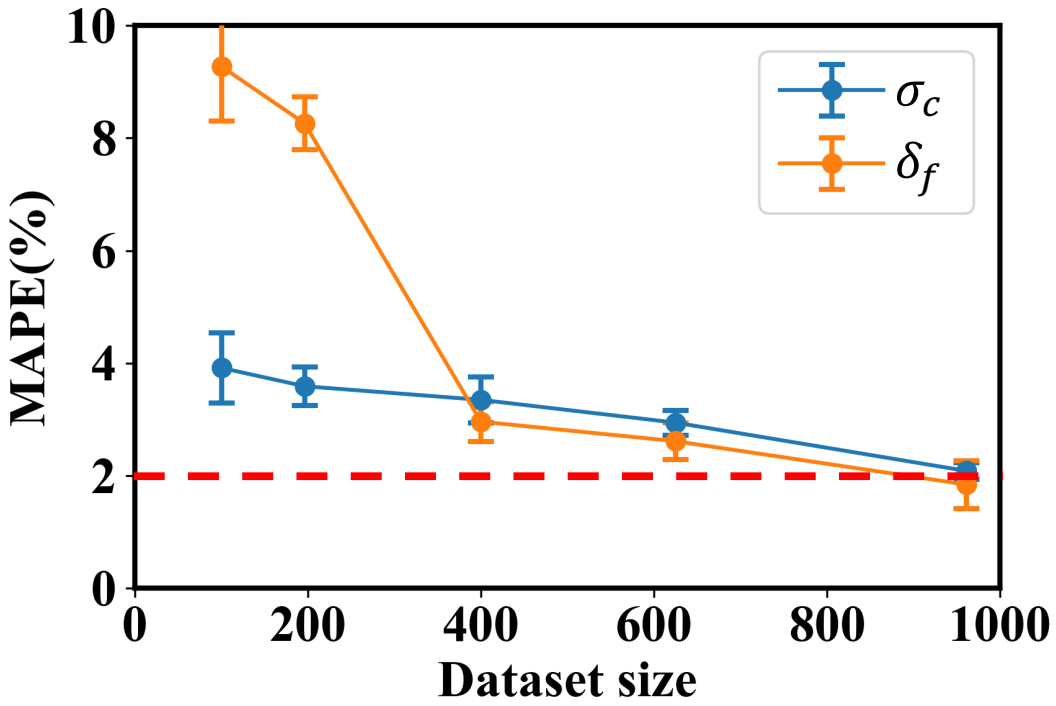

Figure 2.6 The Mean Absolute Percentage Error (MAPE) of σ_c and δ_f as a function of total FEM dataset size. The error bar represents the standard deviation of 4 independent training procedures.

Then, another question arises. If some experiment conditions such as the impact speed change, do we need to train another new batch of 961 FEMs to predict the cohesive parameters? The detailed fringe patterns for two different impact speeds will be different; however, the previously trained neuron weights may still help characterize the new fringe patterns since the fundamental governing equations are the same. Therefore, transferring the previously trained neuron network to further train on the new datasets can practically reduce the dataset size for the new case. Such a technique is called transfer learning (Pan and Yang, 2009). Here, as an example, we study the effect of transfer learning on cohesive parameter prediction on a new FEM dataset with an impact speed of 200m/s. The previously trained network on the dataset with impact speed 100m/s was transferred to further train on the new FEM dataset. The prediction performance as a function of the new FEM dataset size is plotted in **Fig.2.7(a)&(b)** for $\sigma_c \& \delta_f$ with and without transfer learning. As we can see, with transfer learning, the MAPEs drops from ~10% to ~5% compared with the training with a fresh start. With a new dataset of 400 FEMs, MAPEs reach the targeted ~2% if transfer learning is employed. This result illustrates that we can first create a comprehensive training dataset as a baseline and then add a smaller amount of dataset of a specific case to improve the overall training efficiency.

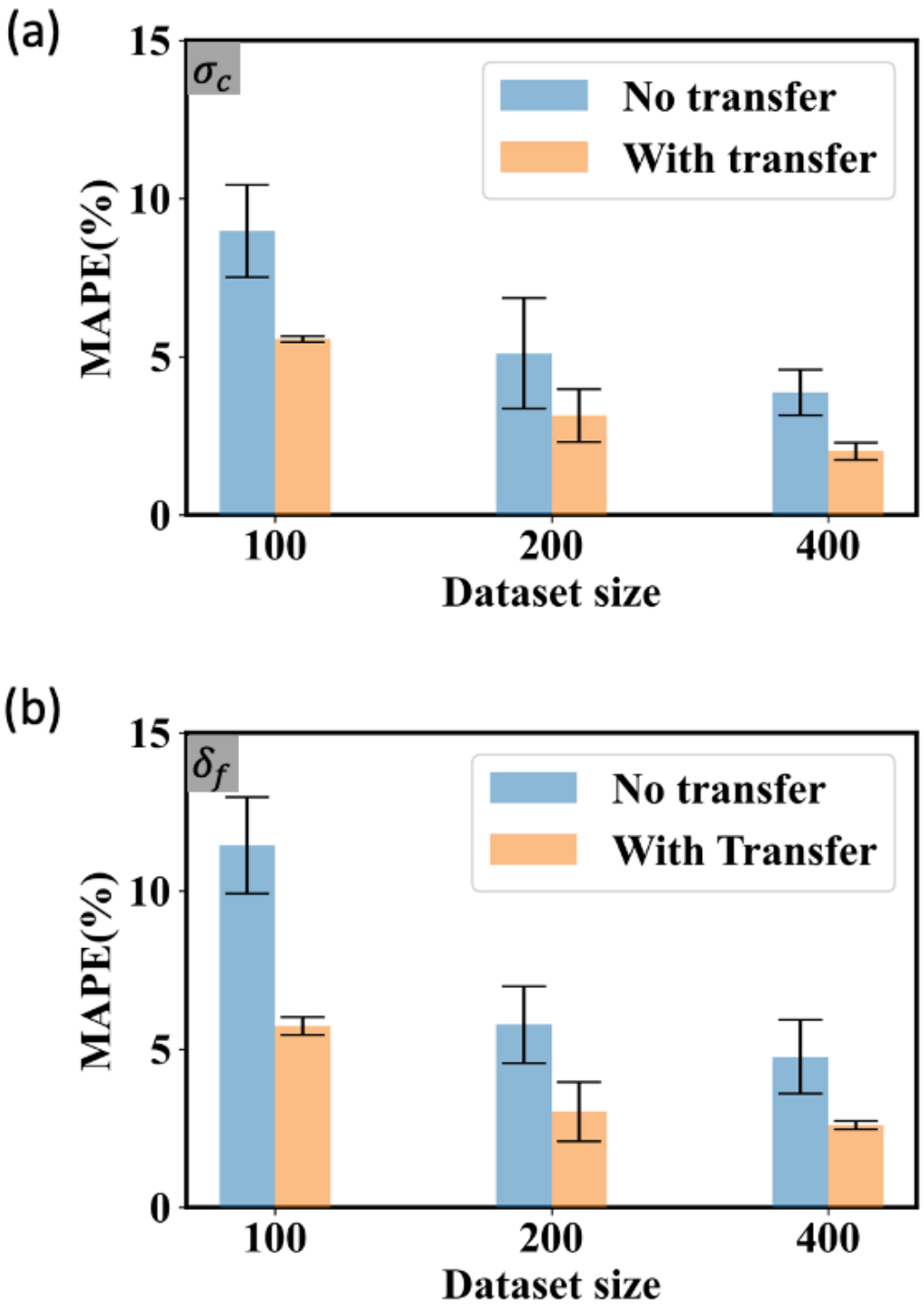

Figure 2.7 The Mean Absolute Percentage Error (MAPE) of (a) σ_c and (b) δ_f as a function of dataset size with and without transfer learning. The error bar represents the standard deviation of 4 training procedures.

2.4.2 The sensitivity of DL-ISI fringe image on prediction performance

The DL-ISI fringe image, representing the displacement gradient on the rear surface, depends on the image shear distance Δx, which relates to the beam incident angle θ_{in}, glass thickness t, and refractive index n_g. A larger Δx yields a denser fringe distribution, which increases the sensitivity to the displacement gradient. The cohesive parameter prediction performance may be affected by the fringe density due to different Δx. **Fig.2.8(a)** shows the FEM fringe images for the same case with cohesive parameters $\sigma_c = 200MPa$ and $\delta_f = 0.052mm$ for four different Δx. To explore the effect of fringe density on the prediction performance, MAPEs of σ_c and δ_f as a function of 4 different Δx are plotted in **Fig.2.8(b)**. Among these four Δx, the MAPE reaches minimum value when $\Delta x = 111\mu m$. As fringe density further increases, the prediction error increases slightly (less than 1%). This is counterintuitive that denser fringe should yield a better prediction performance since it has a larger variation due to surface motion. This phenomenon may be caused by the image resolution limitation. As we can see in the fringe image with $\Delta x = 444\mu m$, the highest fringe density is around 2 pixels per fringe, which is smaller than the kernel size (3×3) of the convolution layer. Therefore, the individual fringe feature could not be fully detected by the convolution kernel for cohesive parameter detection compared to the case with coarser fringes. One possible solution is to increase the image resolution; however, increasing the resolution will significantly increase the training time. Another solution is to use fringe phase unwrapping techniques (Judge and Bryanston-Cross, 1994). When a dense fringe was obtained in an experiment, fringe phase unwrapping was usually used to extract the field information. Therefore, the displacement gradients profile can be obtained

from unwrapping the fringe image. However, the accuracy of fringe unwrapping is subjected to the fringe smoothness and the unwrapping algorithms. If we could adjust the experimental parameters like glass thickness to obtain fringe density according to the optimized FEM training performance, we could maximize the prediction performance and reduce the unnecessary computations on unwrapping data processing.

(a)

Shearing Δx	$56\mu m$	$111\mu m$	$222\mu m$	$444\mu m$
DL-ISI Fringe				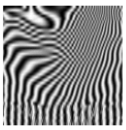
Max Fringe density (pix per fringe)	10	6	4	2

(b)

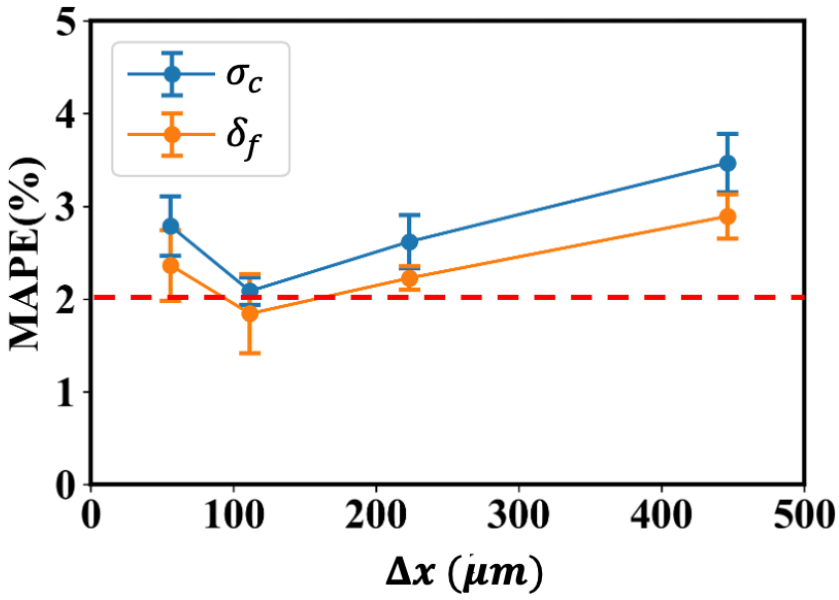

Figure 2.8 The fringe images for the case with cohesive parameters $\sigma_c = 200MPa$ and $\delta_f = 0.052mm$ from 4 different image shear distance Δx; (b) The Mean Absolute Percentage Error (MAPE) of σ_c and δ_f as a function of image shear distance Δx. The error bar represents the standard deviation of 4 independent training procedures.

2.5 Conclusions

In this chapter, we proposed a deep-learning framework that can be used to inversely determine the cohesive laws for dynamic big-data-generating experiments. We chose the problem of determining the dynamic interfacial cohesive parameters between polyurea coating and Al plate under the strain rate up to $10^6 s^{-1}$ as a prototypical problem to illustrate our framework concept. We demonstrated that with a design of novel experimental technique that can generate high-throughput experimental data from a single experiment combined with a state-of-art deep learning algorithm pre-trained with reliable computational training datasets, the dynamic cohesive parameters could be accurately determined with a MAPE less than 2%. This framework serves as an effective methodology to reduce the human effort in designing sophisticated inverse algorithms. Furthermore, this framework has the potential to solve a widespread inverse problem in engineering and physics. For example, determine the material properties like hardness, damage laws, etc., from externally measured full-field displacement field.

Chapter 3

Dynamic fracture of a hierarchically nanostructured copolymer: A deep-learning analysis of big-data-generating experiment

Note: Preliminary experimental results in this chapter has been published in SEM2020 conference proceedings (Kim et al., 2021).

3.1 Introduction

Recently, a nanophase-segregated elastomeric copolymer, polyurea, has gained significant attention on its nano-scale mechanisms of dynamic fracture toughening (Clifton and Jiao, 2015; Grujicic et al., 2015; Jain et al., 2013; Youssef and Gupta, 2012). Bulk polyurea is typically self-assembled to be clustered in hard isocyanate-group and soft diamine-group phases at nanometer-length scales and not homogeneous but segregated. Therefore, polyurea contains a two-phase microstructure consisting of discrete, rod-shaped, so-called hard domains that are dispersed within a continuous soft matrix. The segregated and hierarchically clustered nanostructures are believed to provide peculiar dynamic deformation mechanisms responsible for ultra-high strength of polyurea under high strain-

rate and/or pressure loading. For studying the dynamic response of polyurea, current research on the high-strain-rate response has addressed its deformation under dynamic loading without tackling its resistance to failure associated with failure-initiation and crack-propagation processes. However, the survivability of the structural element that the coating is intended to protect depends on its adhesion to the structural component, and the development of a mechanism-based understanding of failure in elastomers and their interfaces with other materials is critically important.

Regarding the failure analysis, initiation of tensile failure in polyurea PU1000 under conditions of uniaxial strain has been observed through plate-impact, release-wave experiments, which are often used for spall tests (Clifton and Jiao, 2015). In these experiments, a thin flyer impacts a test-sample plate to create a compressive pulse that reflects from the rear surface of the polyurea and generates a tensile pulse after the reflected pulse passes through the oncoming compressive pulse. The dynamic plane-wave test revealed tensile failure stress of polyurea PU1000 approximately 105 MPa under conditions of uniaxial strain. However, polyurea did not spall at this stress level within the tensile-pulse duration. Instead, micro-voids opened on the putative "spall plane," which continued to transmit tensile stress. Knowing the failure initiations stress, actual constitutive relations of the full failure process in spalling require realistic fracture models involving void initiation, growth, and coalescence. Such failure processes are often characterized by cohesive failure models that provide a computational foundation for modeling failure in elastomers. The development of such cohesive models appears to require results of more well-characterized crack-propagation experiments than "spall" tests that involve heterogeneous nucleation and growth of voids.

Such experiments, involving plane wave loading of plates with a single mid-plane crack, have been previously developed and used to study crack growth in a metal, AISI 4340 steel, under mode I (Ravichandran and Clifton, 1989) as well as II & III loading conditions (Zhang and Clifton, 2003, 2007). These plane wave experiments are attractive because of their simplicity in tracing the crack-tip loading conditions through measurements of the motion at the traction-free rear surface of the pre-cracked target plate. However, all previous studies used interferometric techniques like Normal Displacement Interferometry (NDI) or Transverse Displacement Interferometry (TDI) (Kim et al., 1977) that could only measure velocity-time profiles at a single point on the rear surface of the sample. The single-point measurement was particularly troublesome in its accuracy to inversely assess the crack-tip loading profiles. The full displacement-time profiles at the rear surface covering the crack initiation and growth process are desired to inversely determine the cohesive parameters and fracture toughness. Such measurement can be readily achieved from our invention of the Dynamic Line-Image Shearing Interferometer (DL-ISI) with a high-speed streak camera system. Compared to conventional experimental techniques in dynamic experiments, our invention is capable of collecting massive experimental data in a single experiment. We call such a high-throughput experiment the big data-generating experiment.

In this chapter, we first present our invention of the Dynamic Line-Image Shearing Interferometer (DL-ISI) with the streak camera system, which has the capability to generate time-displacement information along with a line profile for material characterization. Then, detailed plate impact experiments on polyurea with mid-plane crack are discussed. The experimental fringe image collected by the streak camera is cleaned and inpainted by a

state-of-art Conditional Generative Adversarial Network (cGAN). The cohesive parameters and fracture toughness are then readily determined from the correlation method as well as the deep learning framework proposed in **Chapter 2**.

3.2 Dynamic Line-Image Shearing Interferometer (DL-ISI)

Due to the resolution limitation of the streak camera system, recording displacement profile directly using an interferometer like the Michelson type is challenging. The number of fringes obtained from the Michelson interferometer is, $n = 2d/\lambda$, where d is the rear surface displacement, and λ is the wavelength of the laser. From a simple FEM analysis, d is in order of 1mm when the crack opens. Therefore, the fringe number n reaches ~4000, which is out of the resolution of the streak camera system with 1024×1024 pixels. A new interferometer that can measure the rear surface line profile with reasonable fringe density is needed. For this purpose, we invented the Dynamic Line-Image Shear Interferometer (DL-ISI), where the fringe information represents the rear surface's displacement gradients.

The DL-ISI optical design is shown schematically as black lines in **Fig.3.1**. In the optical circuit, a laser beam is modulated to synchronously switch the beam by an acousto-optic modulator (AOM) located at the focal plane of the spherical lens SL1, for the exposure duration of a high dynamic range streak camera (C7700). Then the laser beam is collimated and passing through a slit with a size of $10mm \times 2mm$. The slit of collimated beams is illuminated on the rear surface of the specimen with mirror-finish quality. The orientation of the illuminated slit is perpendicular to the crack-front line. Then, the slit image of the reflected beam is projected on the image plane of the streak camera through

the two spherical lenses SL2 and SL3 with the same focal length f_{len}. At the focal point of SL2, a microscope coverslip glass with 150μm thickness is used to create image shearing interfered fringes. The schematics of these two interfered beams reflected from the front surface and rear surface of the glass is shown in **Fig.3.2**. The electric field of the beam reflected from the front surface of the glass can be written as,

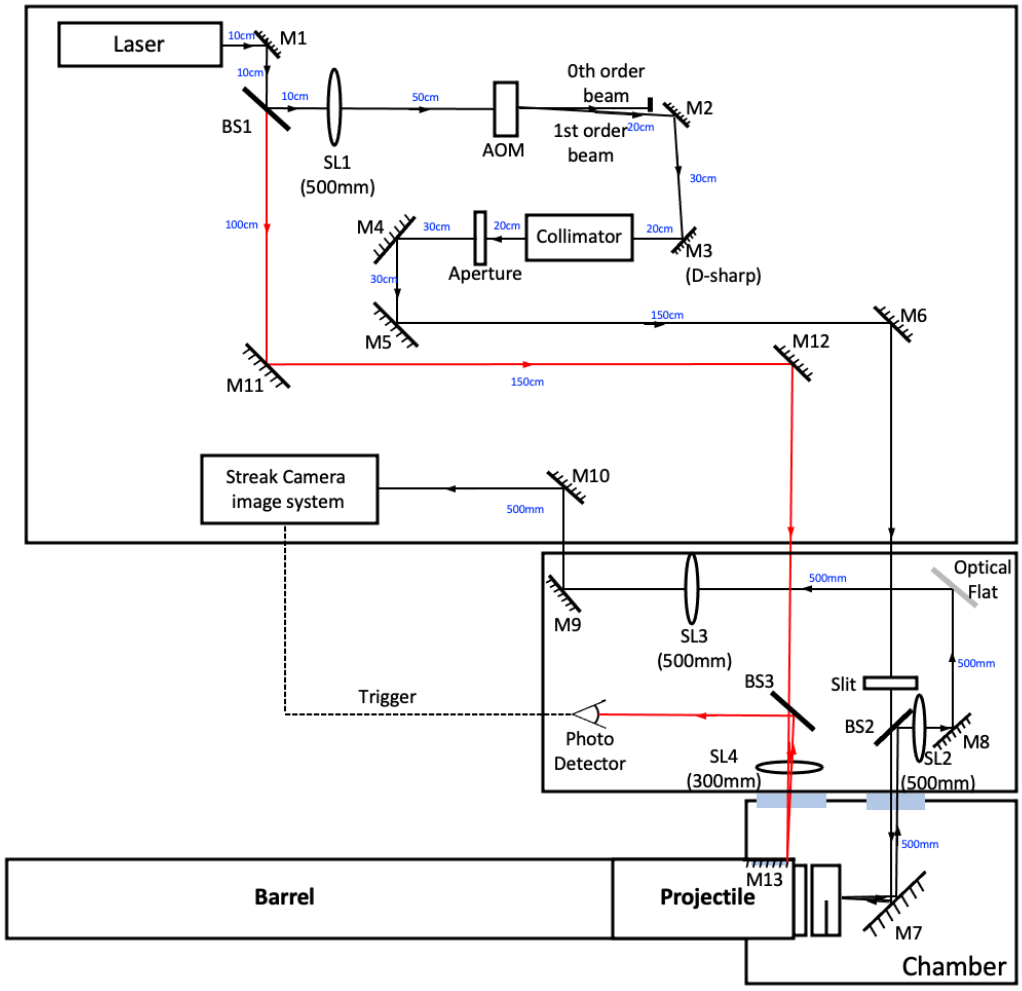

Figure 3.1 Optical schematics of dynamic line-image shearing interferometer (DL-ISI) in the plate impact experiment. The black solid line represents the DL-ISI optical circuits, the red solid line represents the optical triggering circuits for the streak camera system. SL represents the spherical Lens; M represents the mirror.

$$\boldsymbol{E_1}(x,y,z,t) = \boldsymbol{E_{10}}\, exp\left[ik\cdot z + i\frac{k}{2R(z)}(x^2+y^2) - i\omega t - ik\cdot 2u(x,t)\right], \quad (3.1)$$

where $R(z)$ is the radius of curvature of the wave front at z, and $R(z) = f_{len}$ at the image plane. $u(x,t)$ is the out-plane displacement of the sample. Since the slit height is way smaller than the width (less than 1%), we consider the streak camera records the line displacement information only. The electric field amplitude of the beam reflected from the rear surface of the glass is,

$$\begin{aligned}\boldsymbol{E_2}(x+\Delta x, y, z', t) &= \boldsymbol{E_{20}}\, exp\left[ik\cdot z' + i\frac{k}{2R(z')}((x+\Delta x)^2+y^2) - i\omega t - ik\right.\\ &\left.\cdot 2u(x+\Delta x,t)\right], \end{aligned} \quad (3.2)$$

where $z' = z + D + \beta z$ with D the optical path difference of these two beams in the glass and β is the angle between two reflected beams due to a small tilt angle δ in the glass. Δx is the shearing distance in x direction. Their relation can be derived as,

$$D = 2t\left(n_g^2 - sin^2\,\theta_{in}\right)^{1/2}, \quad (3.3a)$$

$$\Delta x = 2t\cdot\frac{sin\theta_{in}cos\theta_{in}}{\sqrt{n_g^2 - sin^2\,\theta_{in}}}, \quad (3.3b)$$

$$\beta = \frac{2\delta\left(n_g^2 - sin^2\,\theta_{in}\right)^{\frac{1}{2}}}{cos\theta_{in}}, \quad (3.3c)$$

where t is the glass thickness, θ_{in} is the beam incident angle, and n_g is the refractive index of the glass. The intensity of these two interfered beams is,

$$I(x,y,z,t) = I_1 + I_2 + 2\sqrt{I_1 I_2}\,cos(\phi), \quad (3.4)$$

where the phase difference ϕ is,

$$\begin{aligned}\phi = k\cdot z + \frac{k}{2R(z)}(x^2+y^2) - k\cdot 2u(x,t) - k\cdot z' - \frac{k}{2R(z')}[(x+\Delta x)^2+y^2] + k\\ \cdot 2u(x+\Delta x,t). \end{aligned} \quad (3.5)$$

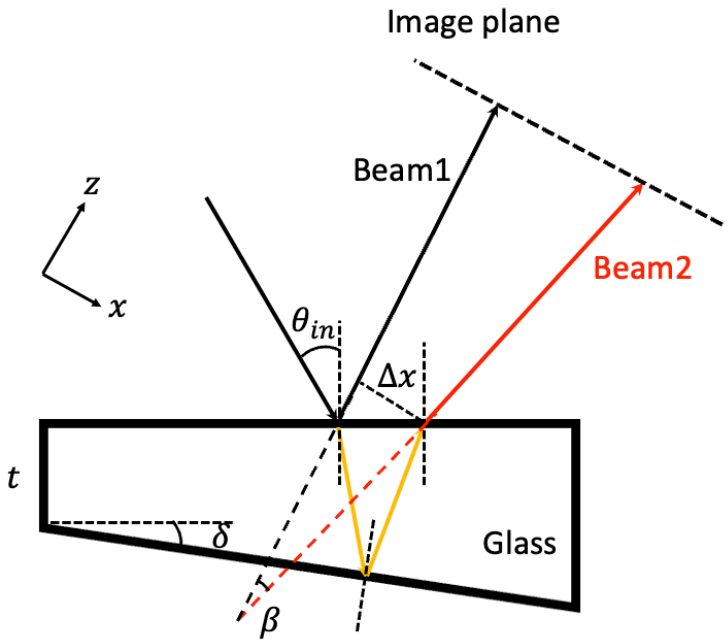

Figure 3.2 Schematics of two beams reflected from the front surface and rear surface of a glass plate with thickness t and a small tilt angle δ.

Since the distance from the glass to the image plane, z is 3 orders of magnitude larger than the optical path difference D, and the glass tilt angle δ is measured as $0.018mrad$ which is considered as negligible, we consider $R(z) \cong R(z + D + \beta z)$. Assuming $I_1 \cong I_2 = I_0$, the intensity of these two interfered beams at the image plane can be derived as,

$$I(x,t) = 4I_0 cos^2\left(\frac{\phi}{2}\right) = 4I_0 cos^2\left[\frac{\pi}{\lambda}D + \frac{\pi}{\lambda}\frac{\Delta x}{f_{len}}x - \frac{2\pi\Delta x}{\lambda}\frac{\partial u(x,t)}{\partial x}\right] \qquad (3.6)$$

As we can see from **Eq.3.6**, the DL-ISI fringe variation depends on the displacement gradient along the image shearing direction $\frac{\partial u(x,t)}{\partial x}$. The second term

represents an initial fringe density which caused by the shearing of the spherical wavefront at the glass plate. The number of initial fringes at the image plane of the streak camera is,

$$N_{inif} = L_b/(\frac{f_{len}\lambda}{\Delta x}), \tag{3.7}$$

where L_b is the length of the laser beam illuminated at the sample. Select proper experimental parameters like glass thickness t or incident angle of the laser beam θ_{in} for different initial fringe density would yield better performance of cohesive parameter determination, as discussed in **Chapter 2**.

3.3 Experiments

3.3.1 Design of polyurea specimen with mid-plane crack

Designing a polyurea sample with a sharp and straight mid-plane crack is crucial in the plate impact experiment. We made the sample through an innovative injection method. First, polyurea solution was prepared from the mixture of an oligomeric diamine, Versalink P-1000 (Air Product) with a diisocyanate, Isonate 143L (Dow Chemicals) in a 4:1 ratio. The P-1000 and Isonate 143L mixture was stirred by a glass stirring rod for 1 min at ambient conditions and degassed for 6 mins in a vacuum chamber. Then the degassed mixture was poured into a syringe. As shown in **Fig.3.3(a)**, the syringe symmetrically injected the mixture into two sides of an acrylic mold which was sprayed with polyurea release spray. A Teflon thin film with a thickness of $50\mu m$ was firmly clamped in the bottom half of the acrylic frames and the supportive plates. As the injection process goes, the mixture automatically lifted the supportive plates while keeping the Teflon thin-film straight. The polyurea specimen was cured and stored in a desiccator at room temperature

for at least 72 hours before demolding. The demolded specimen was cut into $50\text{mm} \times 50\text{mm}$ size with mid-plane crack aligned in the middle of the sample, as shown in **Fig.3.3(b)**. In this way, a polyurea specimen with a sharp mid-plane crack and shiny surface quality for Al coating was prepared. The polyurea flyer was directly molded to a disk shape with a $50mm$ diameter. The flyer and the specimen were molded from the same batch of mixture solution to ensure their material properties were the same. Both flyer and specimen were coated with 200nm Al coating for conductivity for the tilt triggering and reflectivity for the DL-ISI measurement. The Teflon thin film was removed for the first two shots, but it was found the compressive wave will partially self-heal the mid-plane crack in the second shot. Therefore, the Teflon thin film was kept in the third shot.

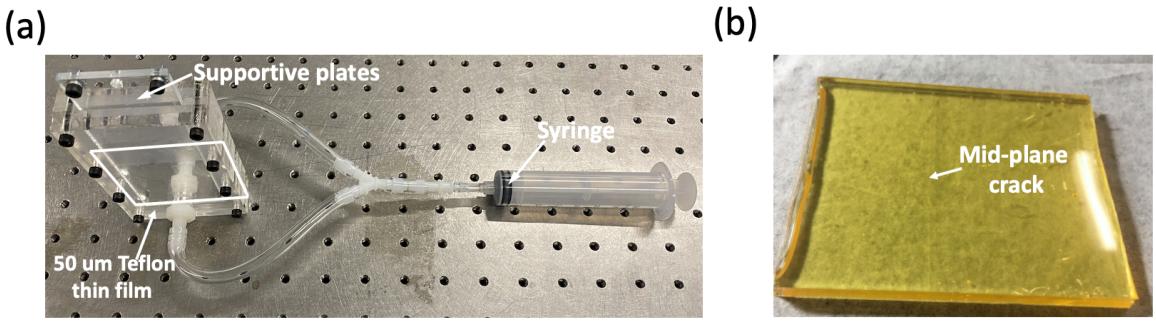

Figure 3.3 (a) Injection molding setup to mold polyurea with a sharp mid-plane crack. (b) Polyurea specimen with a mid-plane crack.

The thickness of the flyer and the specimen is determined based on the time-displacement diagram, as shown in **Fig.3.4**. When the flyer impacts the specimen, compressive waves are generated. When these two waves arrive at the rear surface and reflect as tensile waves, the crack will be loaded for a duration of $t_{load} = \frac{2h}{C_l}$, where h is

the thickness of the flyer, and C_l is the longitudinal wave speed of polyurea. To ensure the observation time window on the rear surface (t_{sd}, t_{ed}) is within the streak camera sweep time window, the thickness of the flyer is selected $h = 2.22\ mm$, while the thickness of the sample is $H = 2h = 4.44\ mm$.

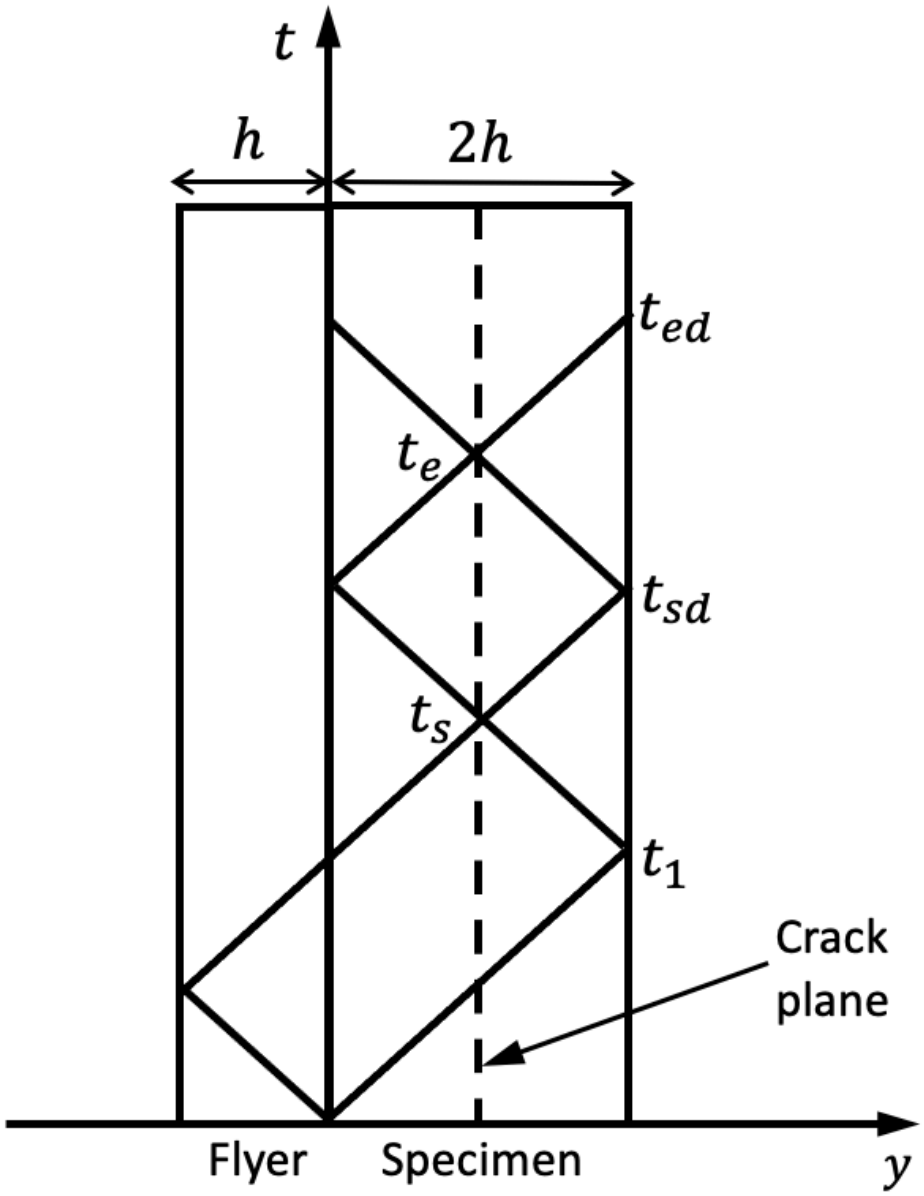

Figure 3.4 Time-displacement diagram for symmetric impact on a specimen with a mid-plane crack.

3.3.2 Streak-camera triggering system design

The streak camera system has an instinct delay time which depends on the sweeping time. If the sweeping time is set as $T_{sweep} = 20\mu s$, the time difference between triggering the streak camera sweep and the beginning of the sweeping image is $T_{delay} = 13.2\mu s$. Therefore, if we trigger the streak camera system at the impact, we will miss the observation window. Triggering the system ahead of the impact is crucial to record the fringe evolution within the window of interests. Here, we designed an optical triggering method, where the optical circuits are illustrated as red lines in **Fig.3.1**. After the fine alignment between the flyer and the specimen, an acrylic spacer with uniform thickness $d_{sp} = 3.88mm$ is placed in between, as shown in **Fig.3.5(a)**. Then, a mirror with a sharp edge is mounted inside the fiberglass projectile. The optics are aligned such that the beam reflected from the edge of the mirror is focused onto a photodetector, which triggers a delayer generator (DG645) that controls the streak camera system. The rising time of the photodetector is 100ns, which is negligible in our case. The triggering sequence is illustrated in **Fig.3.5(b)**. The time when the streak camera gate is triggered by the photodetector is denoted as T_0. Then the streak camera sweep is triggered at $T_1 = 2\mu s$. The sweeping image starts at $T_2 = T_1 + T_{delay} = 15.2\mu s$, and ends at $T_4 = T_2 + T_{sweep} = 35.2\mu s$. Suppose the impact speed of the projectile is $V_0 = 210m/s$, the time at impact will be $T_3 = \frac{d_{sp}}{V_0} = 18.48\mu s$. In this triggering sequence design, the $10\mu s$ window of interests after impact will be centered within the $20\mu s$ sweep time. This triggering design can also accommodate a spacer alignment error up to $1mm$ or an impact speed error up to $50m/s$.

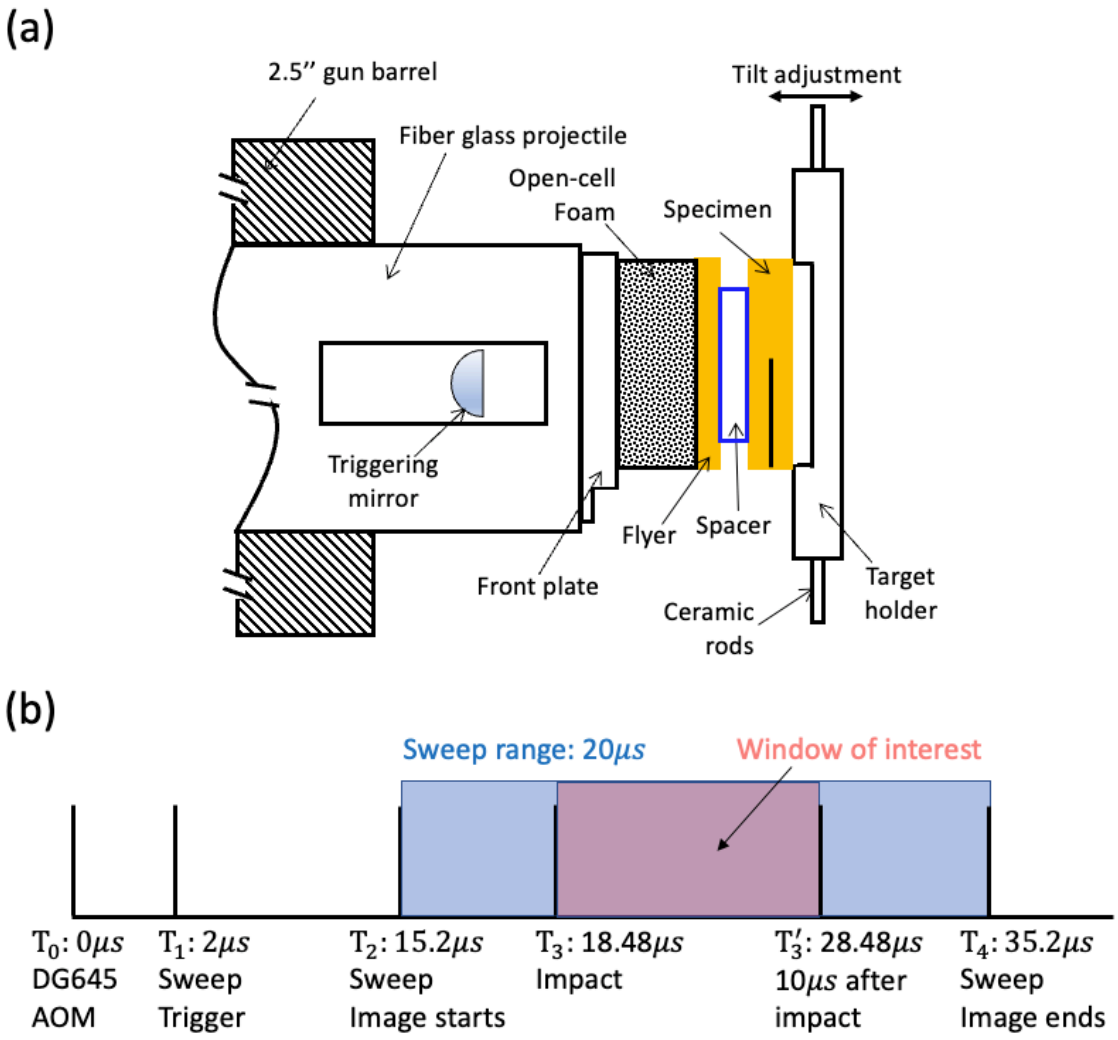

Figure 3.5 (a) Delay triggering setup for the streak camera system. (b) Triggering sequence design.

3.3.3 Plate impact experiments

The plate impact experiments were conducted by a 2.5-inch diameter single-stage gas gun. The detailed experimental procedure for conducting plate impact experiments can be referred to previous Ph.D. theses (Espinosa, 1992; Grunschel, 2009; Kim, 1980; Ravichandran, 1987). Here, key experimental procedures are briefly described below.

The thicknesses of the flyer and the specimen were $2.22mm$ and $4.44mm$, respectively. To reach an ideal stress-free boundary on the rear surface of the flyer, a rigid open-cell foam with $5mm$ thickness was glued between the Al front plate and the flyer. The Al front plate was mounted on a center-grounded fiberglass projectile tube. An "O" ring at the end cup of the projectile helped prevent gas from leaking to the front. A Teflon key was used to prevent the rotation of the projectile in the gas gun barrel with a keyway. The total mass of the projectile and triggering mirror assembly was around 580g. The polyurea specimen with mid-plane crack was mounted on a Delrin sample holder, which was fixed in an adjustable base by four ceramic rods. An optical alignment technique developed by Kumar and Clifton could ensure the tilt angle between the flyer and the sample within $2 \times 10^{-5} rad$ (Kumar and Clifton, 1977). The projectile was accelerated by a sudden release of nitrogen gas. The velocity of the projectile was measured from the times at which five pairs of wire pins with known distances were shortened by the front plate. The parallelism between the flyer and the projectile was measured from the times at which four tilt pins that were glued at the corners of the specimen were shortened by the Al coating on the flyer. The first contact pin triggered the KEYSIGHT oscilloscope for velocity, tilt, and DG645 reference signals. The plate impact experiments were conducted in a vacuum condition to minimize the air cushion between the flyer and the specimen. A good vacuum level between 60 $mTor$ and 80 $mTor$ was desired. Corrugated lead plates were filled in a catcher tank to decelerate the projectile and the sample.

3.3.4 Numerical simulations

To understand the cohesive behavior and determine the fracture toughness of polyurea, FEM simulations of plate impact experiments were conducted by ABAQUS/Explicit package. The strain energy of polyurea can be expressed as (Clifton and Jiao, 2015), $\bar{W}(\bar{I_1}, J) = C_{10}(\bar{I_1} - 3) + f(J)$, where $f(J) = -A(J^{-N-1} - J^{-M-1})$, where $\bar{I_1}$ is the invariant of the left Cauchy-Green tensor, and J is the volume ratio between the current and reference volumes. Here, $C_{10} = 150MPa$, $A = 858Mpa,$ $N = 6$, and $M = 3$. Polyurea was modeled through a user subroutine VUMAT in ABAQUS. The simulations were conducted under the 2D plane-strain condition. The gradient mesh was adapted where the mesh size around the crack tip is $10\mu m$. All solutions reported are the final convergent solutions checked by mesh sensitivity tests. A user-defined bilinear traction-separation cohesive law was implemented as a VUINTER subroutine in the simulations. To explore the fringe sensitivity to the detailed cohesive laws, the DL-ISI fringes from 3 different cohesive laws: bilinear, trapezoid, and exponential laws, with the same fracture toughness, were plotted in **Fig.3.D** in **Appendix**. As we can see, the fringe images are similar to each other, and the image correlations among them are larger than 0.98. Therefore, our DL-ISI fringes are mainly governed by the fracture energy, and it has less sensitivity to the detailed cohesive laws. However, the wall time for each FEM simulation with the exponential cohesive law is almost twice longer than the bilinear cohesive law. Hence, in this thesis, we will use the bilinear traction-separation cohesive law for computational efficiency.

3.4 Results and discussions

We performed three shots with impact speeds of the projectile V_0 ranging from 164 m/s to 210m/s. The experimental results are summarized in **Table 3.1**. Among three shots, we successfully captured the DL-ISI fringe within the desired window in the third shot. The DL-ISI parameters are listed in **Table 3.2**.

Table 3.1 Summary of experimental results. h is the thickness of the flyer, H is the thickness of the specimen with a mid-plane crack, V_0 is the impact speed of projectile, θ_t is the tilt angle, σ_0 is the normal stress, Δc is the crack growth length.

Shots No.	h (mm)	H (mm)	Teflon	V_0 (m/s)	θ_t $(mrad)$	σ_0 (MPa)	Δc (μm)
HJ1901	1.98	4.44	N	164	1.70	184	400
HJ2001	2.22	4.33	N	209	2.44	234	297
HJ2101	2.25	4.38	Y	204	3.04	229	306

Table 3.2 DL-ISI parameters in HJ2101

Description	Notation	Value
Wavelength of laser	λ	532nm
Laser beam length	L_b	10mm
Laser beam width	W_b	2mm
Streak camera slit width	W_{sk}	$100\mu m$
Refractive index of glass plate	n_g	1.52
Beam incident angle	θ_{in}	45^0
Glass thickness	t	$150\mu m$
Image plane distance	f_{img}	$500mm$

3.4.1 DL-ISI fringes

The raw experimental fringe image from the streak camera system for Shot 2101 is shown in **Fig.3.6**. The horizontal axis represents the spatial information in a line perpendicular to the crack plane at the rear surface with $x = 0$ aligned at the initial mid-crack tip position, while the vertical axis represents the temporal information with $t = 0\mu s$ representing the time at impact.

To correct the image noise and inhomogeneous illumination issues of the streak camera system, the raw experimental fringe image was filtered by the 3×3 low pass filters and then passed through an intensity-normalization filter. The resultant fringe image is shown in **Fig.3.7(a)**. To understand the general feature of the experimental fringe, a benchmark FEM simulation with a perfect-bonded cohesive law is performed, and the computational fringe is plotted in **Fig.3.7(b)**. When $t < t_1 = 2.7\mu s$, the compressive wave has not arrived at the rear surface. Therefore, the sweeping of the initial fringe is observed. From **Eq.3.7**, the number of initial fringes is $N = 4.2$, which is consistent with the experimental observation. The 3.04mrad tilt angle between the flyer and the specimen generated a tilt of compressive wavefront 1.7^0, which led to a shift of initial fringe, as observed in both experimental and FEM fringe images. During the crack loading time range ($t_{sd} < t < t_{ed}$), the tensile wave reflected from the crack tip arrived at the rear surface. Thus, the fringe density varied according to the change of displacement gradient due to crack opening.

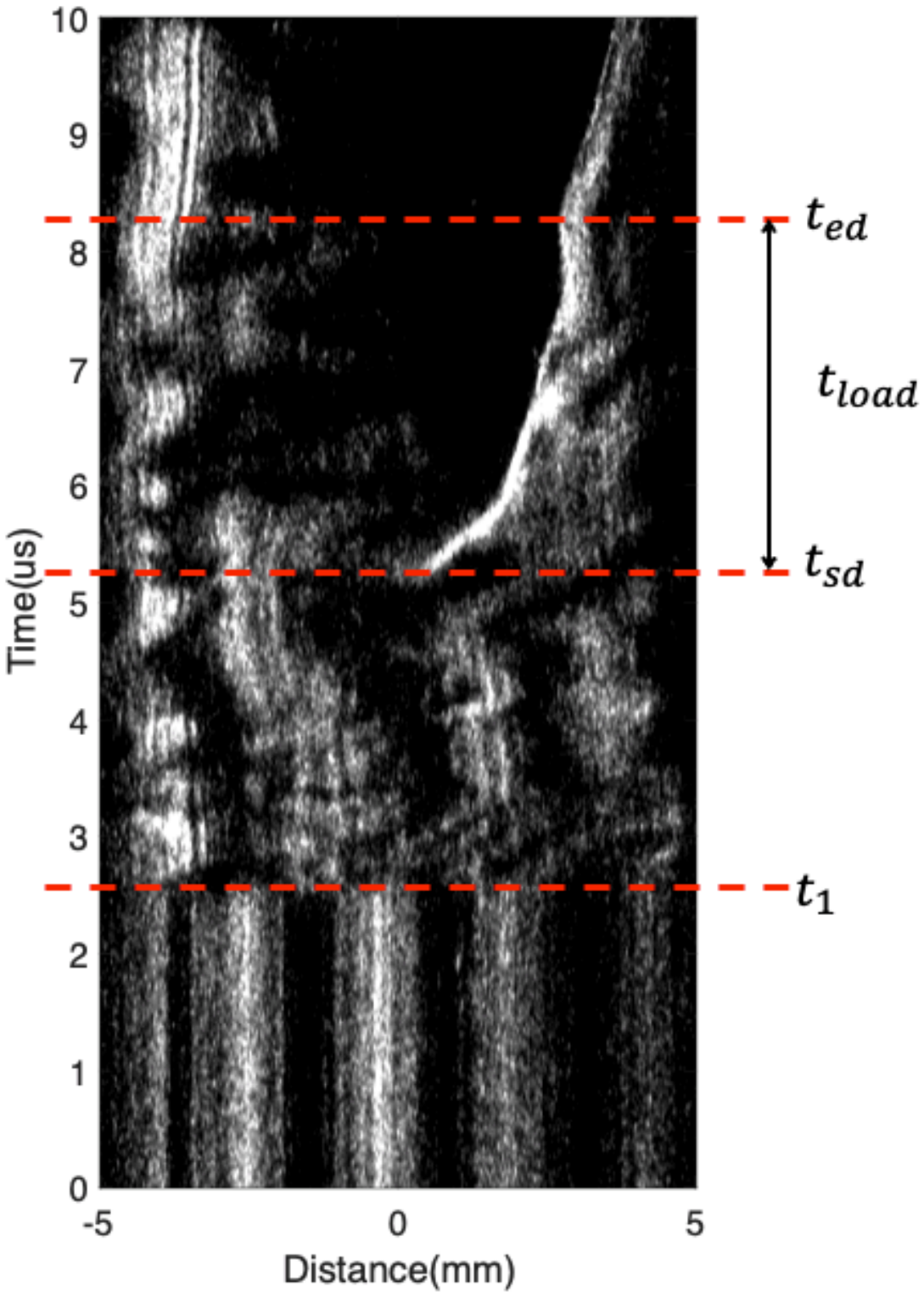

Figure 3.6 Raw experimental DL-ISI fringe image measured from Shot HJ2101. The time markers correspond to those in **Fig.3.4.**

As we can see in **Fig.3.7(a)**, the experimental fringe captured the correct crack loading period. However, it only displayed fringes away from the crack tip while losing the fringe information near the crack tip. There are two reasons which could lead to this phenomenon. First, the large surface gradient near the crack tip during the tensile wave loading period would yield the reflected laser beam moving out of the collimation lens (SL2 in **Fig.3.1**). Therefore, the laser beam position at x in the following relation,

$$\left| x - 2\frac{du(x,t)}{dx} \cdot f_{len} \right| > \frac{d_{len}}{2}, \tag{3.8}$$

could not be observed in the experiment. Here, $d_{len} = 50mm$ is the diameter of the collimation lens, and $f_{len} = 500mm$ is the focal length. The FEM fringe considered this surface warping effect is plotted in **Fig.3.7(c)**. Indeed, most of the fringe information near the crack tip is missing due to the large surface gradient. Here, we only considered the surface warping effect out of the first collimation lens. However, in the experiment, some reflected laser beams could also move out of the range of the second collimation lens (SL3 in **Fig.3.1**) or other optics. Therefore, the missing portion of the fringe will be larger in the experiment, as comparing **Fig.3.7(a) &(c)**.

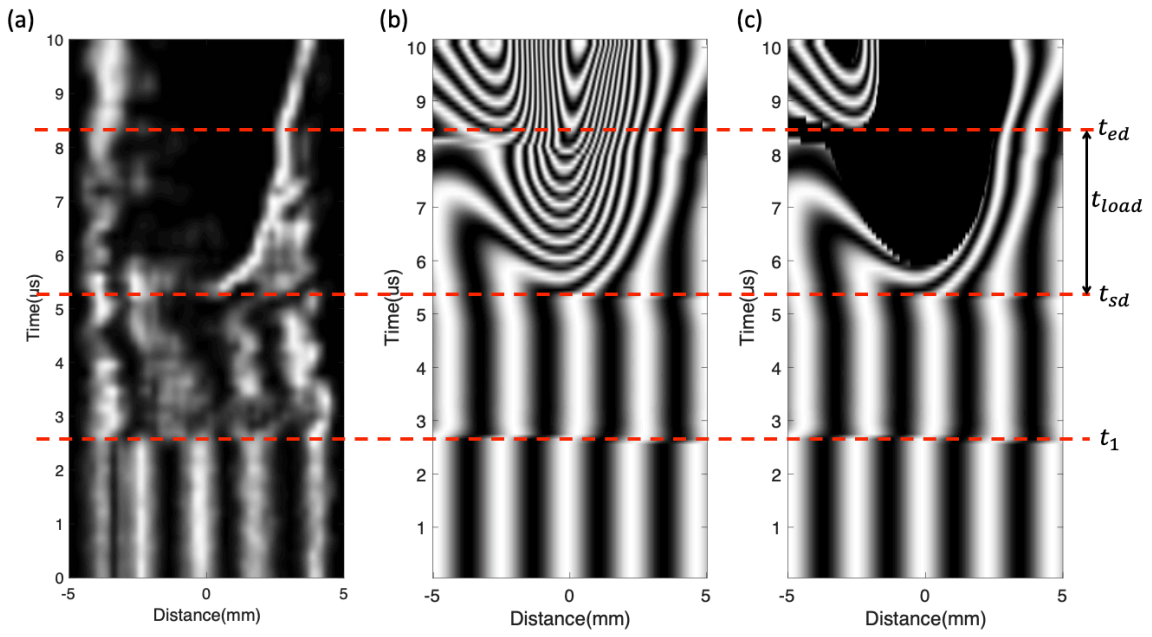

Figure 3.7 (a) Smoothed experimental DL-ISI fringe image; (b) Computational DL-ISI fringe image from FEM with a prefect-bonded cohesive law; (c) Computational DL-ISI fringe image considering surface warping effect.

Second, the compressive strain at the rear surface ahead of the crack tip is found to be ~6% from FEM. This compressive strain is higher than the critical buckling strain of the 200nm Al coating on polyurea substrate, $\varepsilon_{bc} = \frac{1}{4}\left(\frac{3E_{PU}}{E_{Al}}\right)^{2/3} \sim 4\%$, which could yield a buckling wavelength, $\lambda_{bc} = 2\pi h_{Al}\left(\frac{E_{Al}}{3E_{PU}}\right)^{\frac{1}{3}} \sim 2.3\mu m$. The buckled Al coating functioned as a diffraction grating and could generate diffractive lights recorded by the streak camera, as observed in **Fig.3.6**. Delamination or cracking of the Al coating was also possible to cause the incomplete fringe image.

3.4.2 Physics-based DL-ISI fringe inpainting with Conditional Generative Adversarial Nets (cGAN)

As discussed in the previous section, the experimental fringe information was missing when the reflected wave from the crack-plane arrived at the rear surface of the polyurea specimen due to the large surface gradient and the failure of the Al coating. Nevertheless, the boundary fringe was successfully measured in the experiment, whose characteristic shape is consistent with the FEM fringes. If we could inversely obtain the missing fringes based on this boundary fringe, we could understand the crack propagation history and hence measure the dynamic fracture toughness of polyurea.

This physics-based fringe inpainting is possible because of the recent development of Conditional Generative Adversarial Nets (cGAN) (Mirza and Osindero, 2014). Although the original idea of a GAN (Goodfellow et al., 2014) is used for unsupervised learning without giving specific labels, a cGAN can generate new data based on a given condition. For example, in our case, we would like to train a cGAN model to generate a full fringe image from the given condition of a partial fringe image. Since its original development, cGAN has been successfully used in image-to-image transitions like image semantic segmentation (Rezaei et al., 2017) and image inpainting (Isola et al., 2016). As for its application in Solid Mechanics, cGAN is capable of inversely identifying the material modulus distribution from the given strain distribution images (Ni and Gao, 2021) or predicting strain and stress distributions for complex composites (Yang et al., 2021a; Yang et al., 2021b). However, most current applications of cGAN in engineering have been limited to a computational framework. Here, we will apply cGAN on the physics-based

experimental fringe inpainting. To our knowledge, this is the first application of cGAN used for real experimental data cleaning.

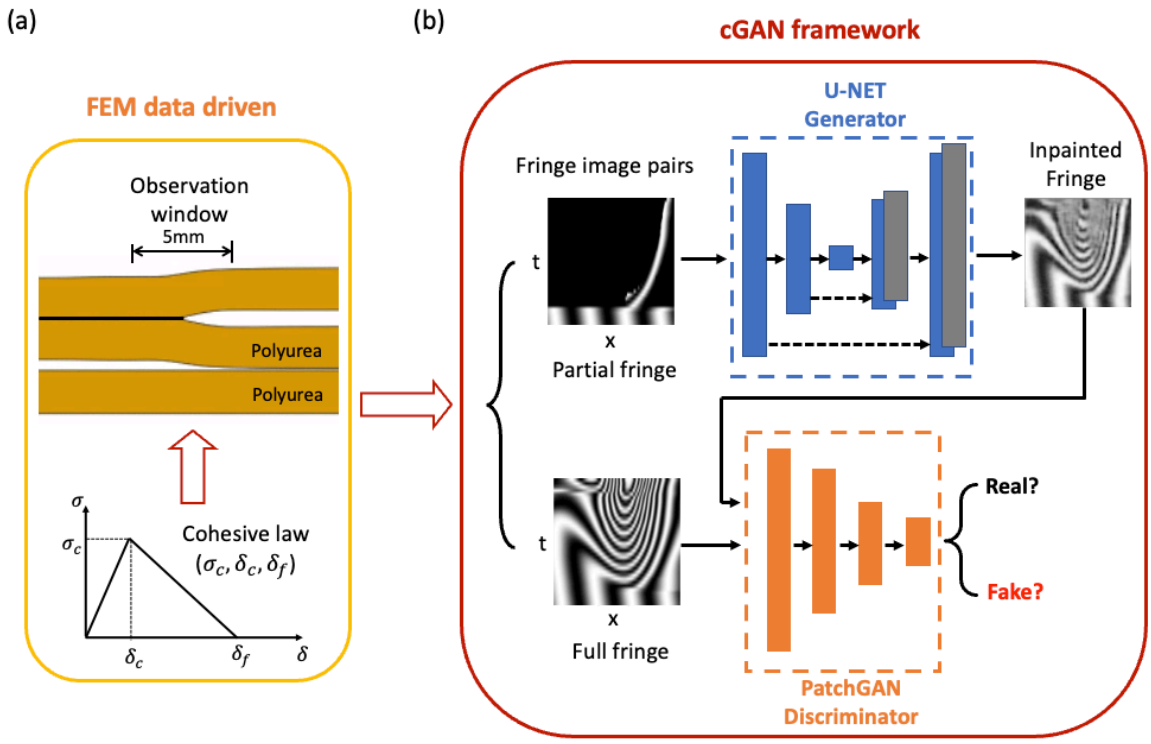

Figure 3.8 Schematics of the cGAN model consisted of a generator with U-NET architecture and a discriminator with PatchGAN architecture for the physics-based DL-ISI fringe inpainting.

As shown in **Fig.3.8**, the typical cGAN model consists of a generator with U-NET architecture (Ronneberger et al., 2015) and a discriminator with PatchGAN architecture (Isola et al., 2016). The U-NET with skip-connection techniques is used to generate the full fringe images from the input of the given missing fringe images, while the PatchGAN evaluates the generated fringe images by comparing with the input images patch by patch. During training, the generator generates new fringe images as authentic as the ground-true

fringe images while the discriminator learns to perform better to distinguish the new image from the ground truth. The performance of these two adversarial networks improves until reaching a Nash equilibrium when the generated fringe image is too real to be distinguished by the discriminator.

The cGAN model was trained on a dataset with 961 pairs of full and partial fringe images obtained from FEM with different 2-parameter (σ_c, δ_f) bilinear cohesive laws. The computational training set preparation has been described in detail in **Chapter 2**. To produce a training dataset as consistent as the experimental fringe, the displacement gradient at the rear surface satisfies **Eq.3.8** was removed to produce the partial fringe images as input images. Furthermore, the left portion of the computational fringe images was removed since the Al coating on the left side of the rear surface was damaged. Examples of input and ground-true fringe images are shown in **Fig.3.8**. The total dataset with 961 fringe images was randomly split into 90% train dataset and 10% test dataset. The training fringe images were rescaled to 128×128 pixels. The normalized L2 error is used as the cGAN model performance matrices as,

$$E_{L2} = \sqrt{\frac{\sum_{i,j}\left(I_{ij}^{pre} - I_{ij}^{true}\right)^2}{\sum_{i,j}\left(I_{ij}^{true}\right)^2}} \times 100\%, \tag{3.9}$$

where I_{ij}^{true} and I_{ij}^{pre} are the intensity at pixel i, j. The detailed model architectures for generator and discriminator are listed in **Table 3.B.1** and **3.B.2** in **Appendix 3.B**. The training was performed on the open-source platform TensorFlow V2.5 (Abadi et al., 2016). The Adam optimizer (Kingma and Ba, 2014) with a learning rate of 0.0002 was used to optimize the cGAN model. The batch size was set as 32 in our model.

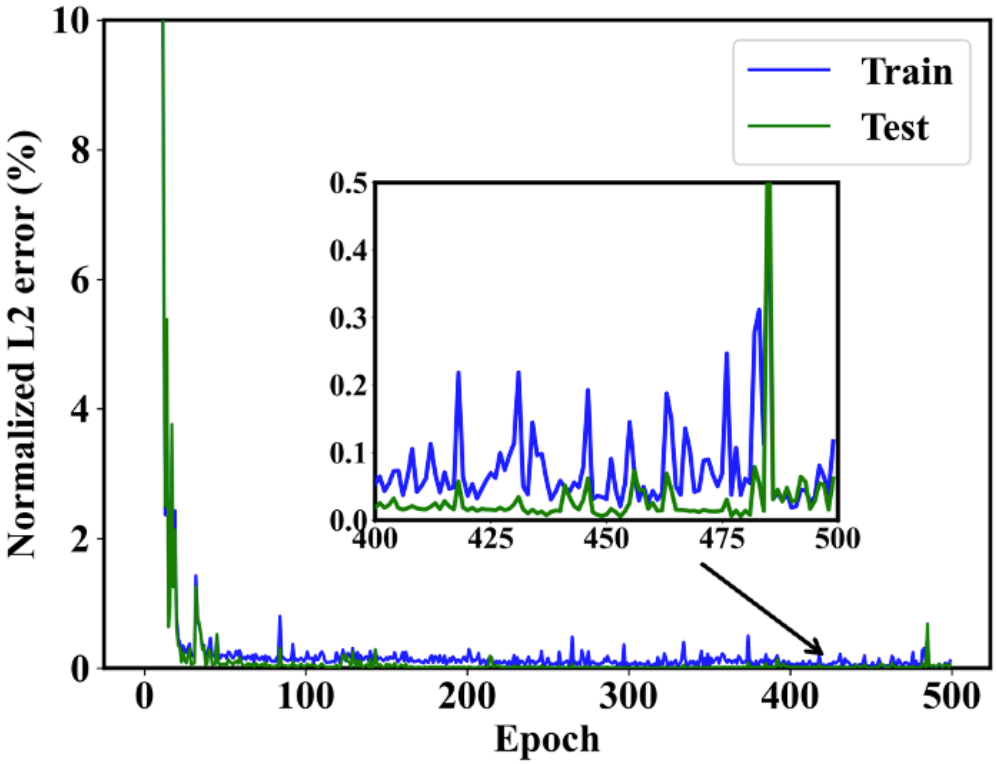

Figure 3.9 Training performance of the cGAN model as a function of train epoch.

The normalized L2 errors of train and test datasets as a function of train epochs are shown in **Fig.3.9**. The total training time for 500 epochs on a 32-core CPU is around 8 hours. As we can see, both errors rapidly reduced to 2% after 10 epochs and converged to 0.05% after 100 epochs. The errors of train and test datasets are similar, so no overfitting is observed. Because of the image-to-image mapping capability of the cGAN model, training 200 epochs on the current cGAN model with a 961 FEM dataset is sufficient to make a prediction with a 0.05% error. To visualize the cGAN model performance, the predicted fringe images from two randomly selected input fringe images from the test datasets after 200 epochs are shown in **Fig.3.10**. The pixel-wise L2 errors between prediction and ground-truth are also plotted. As we can see, the majority of pixels have an

error of less than 0.2%, and the pixels with the biggest errors are at the boundary of each fringe. These results illustrate the accurate performance of pixel-wise fringe inpainting from cGAN model. Besides its high accuracy, the well-trained cGAN model is also efficient in generating a new fringe image. For example, it takes around 5ms for the cGAN model to generate a new fringe image on a new input fringe image on a personal computer.

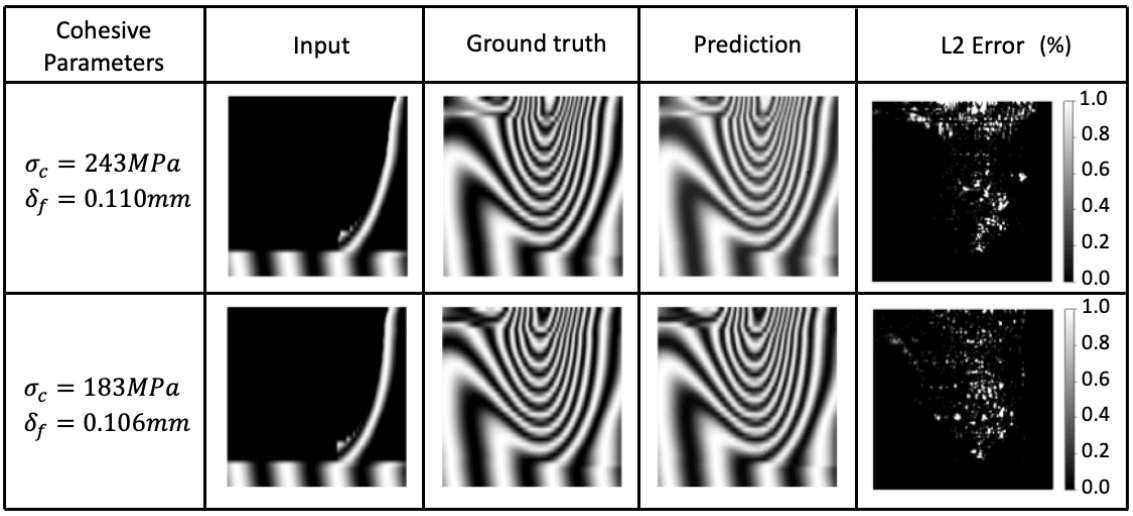

Figure 3.10 Input fringe images, ground-truth fringe images, predicted fringe images, and the normalized L2 errors of two randomly selected input images in the test dataset after 200 epochs of training.

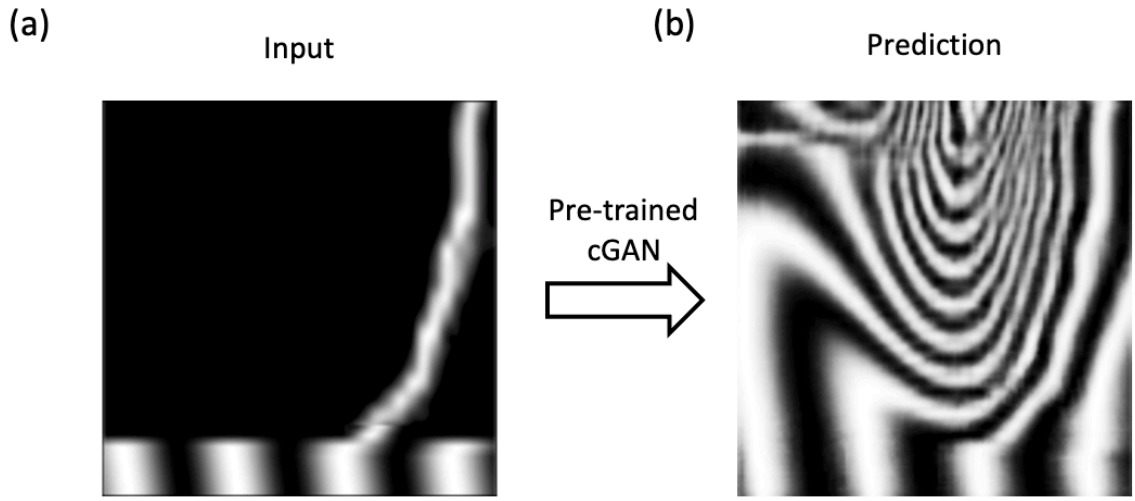

Figure 3.11 Fringe inpainting of experimental fringe image with initial fringe padding from pre-trained cGAN with 200 epochs.

After training the cGAN model on the FEM fringe dataset for 200 epochs, the filtered experimental DL-ISI fringe image (**Fig.3.7(a)**) was cropped with a maximum correlation window with FEM datasets and rescaled to 128×128 pixels as the input image to generate the inpainted fringe image. Compared with the FEM fringe image, the experimental fringe image does not have clear initial fringes due to the surface tilt effect. To be consistent with the FEM train dataset, we prepared an experimental fringe image input with initial fringe padding from FEM as well. Then, the padded fringe image was processed with histogram equalization with the FEM inputs. The processed experimental fringe is shown in **Fig.3.11(a)**. The inpainted fringe images from the input images are shown in **Fig.3.11(b)**. The missing fringes were able to be inpainted inversely from the characteristic boundary fringe measured in the experiment. It is worth noting that the generated fringe image becomes locally blurred and zigzag, especially where the fringe density is high, compared with the FEM dataset. It is because the characteristic fringe is

not as smooth as in the FEM dataset, which could produce noise when the cGAN model makes the prediction. Nevertheless, the pre-trained cGAN model with a computational dataset is capable of generating a physics-based full-field fringe image from the experimental data.

3.4.3 Cohesive parameters and dynamic fracture toughness of polyurea

Since we obtained the full-field fringe image during the crack loading process from the cGAN model, the cohesive parameters could be ideally determined through the deep learning framework proposed in **Chapter 2**. However, as discussed in the previous subsection, the inpainted fringe is locally noisier and zigzag compared with the FEM dataset, which could reduce the accuracy of CNN predictions. Here, we calculate the correlations between the inpainted fringe and each FEM fringe in the FEM dataset, and statistically determine the cohesive parameters as well as the fracture toughness. The CNN prediction is also then included for comparison. The correlation coefficient is defined as,

$$cor = \frac{\sum_{i,j}\left(I_{ij}^{exp} - \bar{I}^{exp}\right)\left(I_{ij}^{FEM} - \bar{I}^{FEM}\right)}{\sqrt{\sum_{i,j}\left(I_{ij}^{exp} - \bar{I}^{exp}\right)^2 \sum_{i,j}\left(I_{ij}^{FEM} - \bar{I}^{FEM}\right)^2}}, \tag{3.10}$$

where I_{ij}^{exp} and I_{ij}^{FEM} are the intensity at pixel i, j for experimental and FEM fringe image, respectively. $\bar{I}^{exp}$ and $\bar{I}^{FEM}$ are the mean values. The correlation coefficients are plotted in **Fig.3.12**. The correlation coefficients are in the range of 0.35~0.89. To determine the cohesive parameters as well as the standard deviations, the correlation coefficients with $\mathrm{cor} > 0.75$ are fitted into a bivariate normal distribution. The prediction results are summarized in **Table 3.3**. The predicted cohesive parameters with error bar are marked in

yellow in **Fig.3.12**. The dynamic fracture toughness of polyurea under an extremely high rate of crack-tip loading $\dot{K}\sim 10^7 MPa\sqrt{m}/s$ is determined as $G_c = 12100 \pm 1100 MPa$. The estimation of dynamic fracture toughness based on the linear elastic fracture mechanics (LEFM) theory is $G_c^{LEFM} = 13418.62 J/m^2$ (Details in **Appendix 3.A)**, which overestimates ~11%.

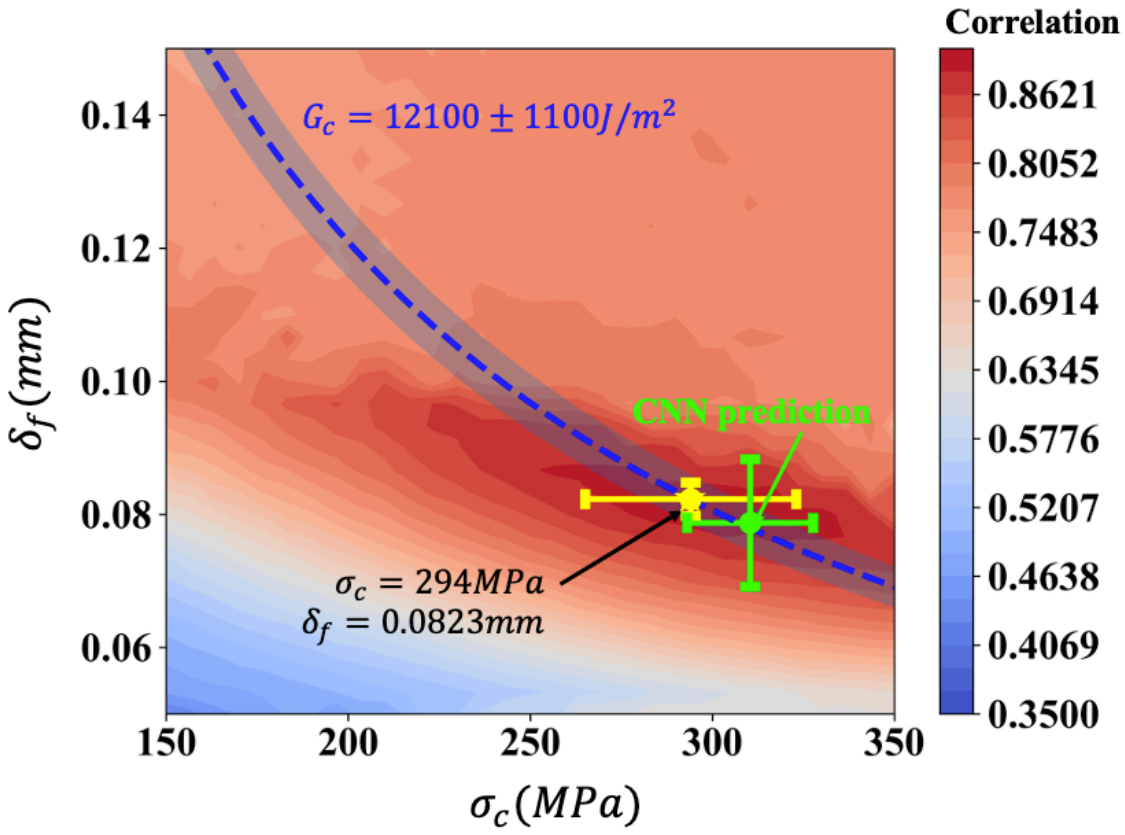

Figure 3.12 Correlation coefficients contour between the experimental fringe and 961 FEM fringes in the dataset. The cohesive parameters with error bar determined from bivariate normal distribution are marked in yellow. The dynamic fracture toughness is marked in blue dotted line with shaded error bar. The CNN predictions with error bars are marked in green.

A CNN model was also trained on the dataset with 961 FEM fringe images to predict the cohesive parameters on the experimental fringe image. The Absolute Percentage Error (MAPE) on the train and validation dataset is plotted in **Fig.3.C.1 in Appendix 3.C**. MAPE for both parameters steadily approach 1% as the train epoch increases. The train performance is better than the interfacial FEM dataset in **Chapter 2**. After training the CNN for 2000 epochs, prediction preformation of cohesive parameters on train and test datasets are plotted in **Fig.3.C.2**. Again, the CNN has good prediction performance on cohesive parameters in the test dataset. Then, the well-trained CNN model is used to predict the experimental cohesive parameters. The CNN prediction based on 7 independent trainings is summarized in **Table 3.3** and marked as green in **Fig.3.12**.

Table 3.3 Cohesive parameters predictions from the correlation and CNN methods

Correlation			CNN		
$\sigma_c(Mpa)$	$\delta_f(mm)$	$G_c(J/m^2)$	$\sigma_c(MPa)$	$\delta_f(mm)$	$G_c(J/m^2)$
294 ± 29	0.0823 ± 0.0025	12100 ± 1100	310 ± 17	0.0787 ± 0.0096	12200 ± 1700

As we can see, the CNN makes a reasonable prediction of the fracture toughness with only a 1% difference with the correlation method. However, prediction discrepancies have been made in the individual parameters. Furthermore, CNN has a more significant prediction variance than the correlation methods. It is due to the difference in fidelity between our train dataset and experimental test dataset, such that our training dataset is the 2D FEM dataset with low fidelity. However, the experimental inputs have high fidelity. Therefore, constructing the correlation between these two datasets plays a crucial role in

the multi-fidelity modeling method (Fernández-Godino et al., 2016). To this end, a multi-fidelity deep neural network (MFNN) (Meng and Karniadakis, 2020) has been developed, which can efficiently train the datasets with different levels of fidelity. For example, compared with the single-fidelity training, MFNN is capable of increasing the prediction accuracy on the material properties in the instrumented indentation when trained on a multi-fidelity dataset with both FEM and experiments (Lu et al., 2020). Therefore, as more experimental fringes are collected in future experiments, we could use MFNN to train the FEM fringes as well as the previous experimental fringes together to increase the accuracy of the predictions. Except for the error source from the multi-fidelity, other error sources on the predictions could come from the sensitivity of the DL-ISI fringe, cGAN, and CNN models. These errors may not be independent, thus, distinguishing the errors among these different sources is not feasible.

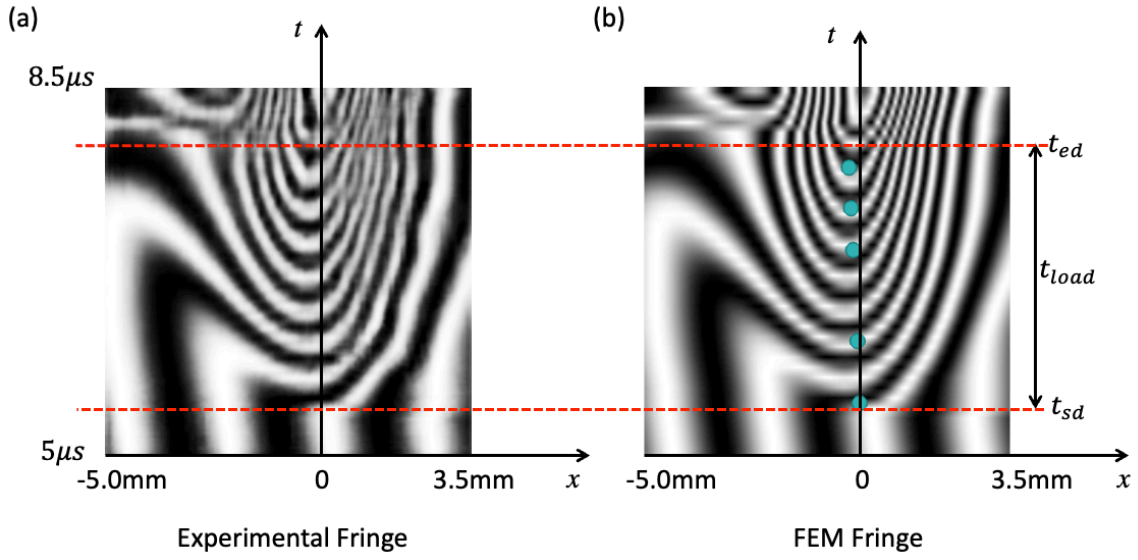

Figure 3.13 (a) Inpainted experimental fringe; (b) FEM fringe generated from FEM simulation with predicted cohesive parameters of $\sigma_c = 294.03MPa$ and $\delta_f = 0.0823mm$. The crack tip positions are labeled in green dots.

When the accurate cohesive parameters are determined, the crack growth history can be readily analyzed from the FEM. The FEM fringes generated from the simulation with the predicted cohesive parameters are plotted together with the experimental fringes in **Fig.3.13**. Two fringe images are very similar, with a correlation coefficient of 0.881. The crack-tip positions are labeled in green markers on the FEM fringe image. The maximum crack growth length during the first crack loading period is $250\mu m$. The fractography of the crack plane after the impact was obtained from optical microscopy and shown in **Fig.3.14**. A classical polymer crazing failure zone is observed on the opened crack plane. There seems to be a two-stage crack-growth process zone. Stage I crack has a relative wavy crack front with the average wavelength of 100~200 μm and the average crack growth distance of 200~250 μm. The crack growth distance is consistent with the FEM crack growth length during the first loading period. This wavy crack front with micro-scale wavelength could be caused by the local material inhomogeneity (Gao and Rice, 1989; Rice et al., 1994). Clusters with size of hundred nanometers were observed in bulk polyurea from our high-resolution AFM tapping-mode morphology images. However, in the micron-scale, the polyurea sample is considered as homogenous, and linear-elastic crack-front growth instability is not expected. It is not clear whether the waviness is a result of nearly incompressible and viscous process zone's meniscus instability or bluntness variability of the initial stationary crack tip. Nevertheless, this 3D crack advance process was not considered in our FEM simulations for computational efficiency. Stage II crack shown in the fractography could be propagated during the second loading period or damaged when the sample crashed into the catcher. The cohesive strength σ_c and the toughness of polyurea G_c under the crack loading rate are displayed on an Ashby diagram

(Ashby, 2012) in **Fig.3.15**. Under the dynamic loading, the cohesive strength of polyurea is found in the cohesive-property range of composites, which is far beyond the strength of any other polymers and rubbers.

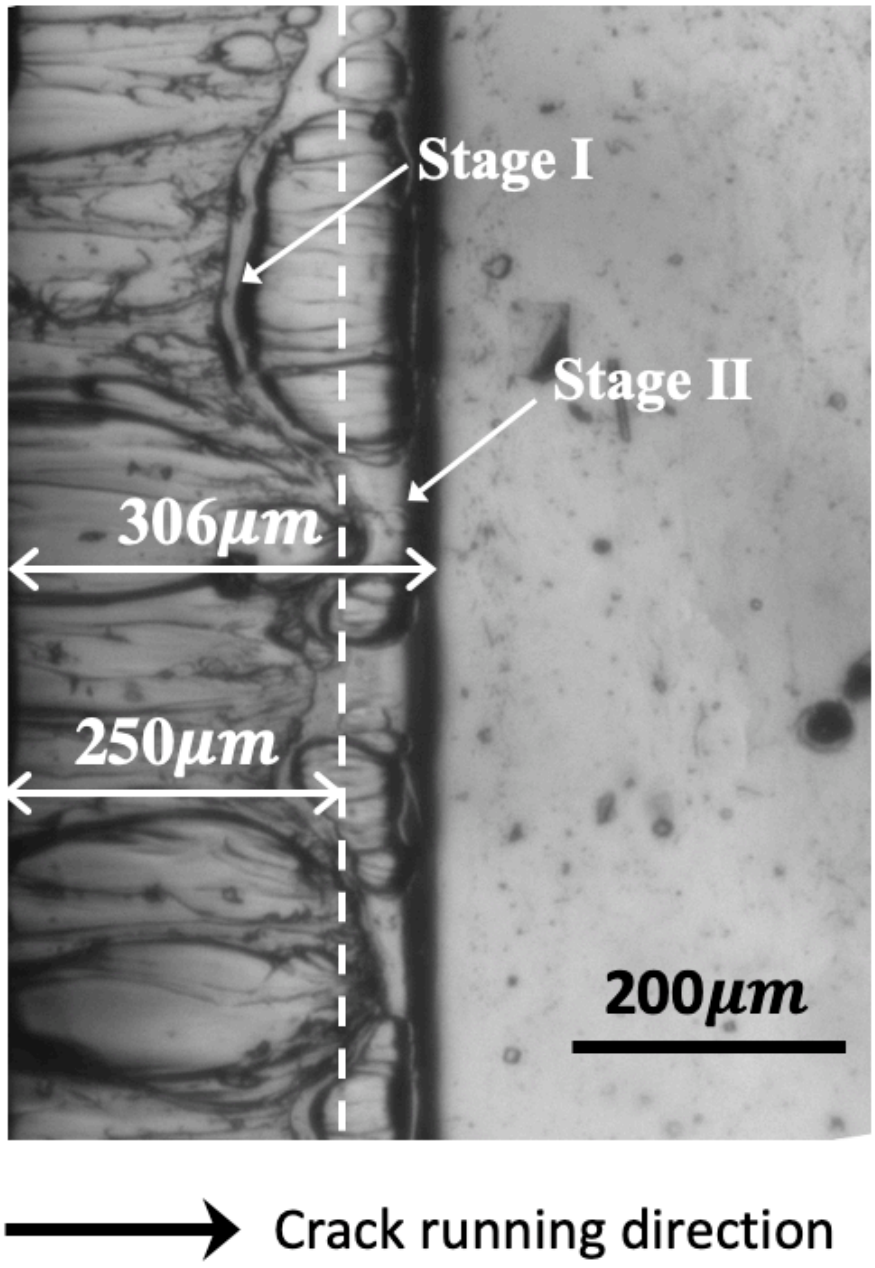

Figure 3.14 Fractography for Shots HJ2101.

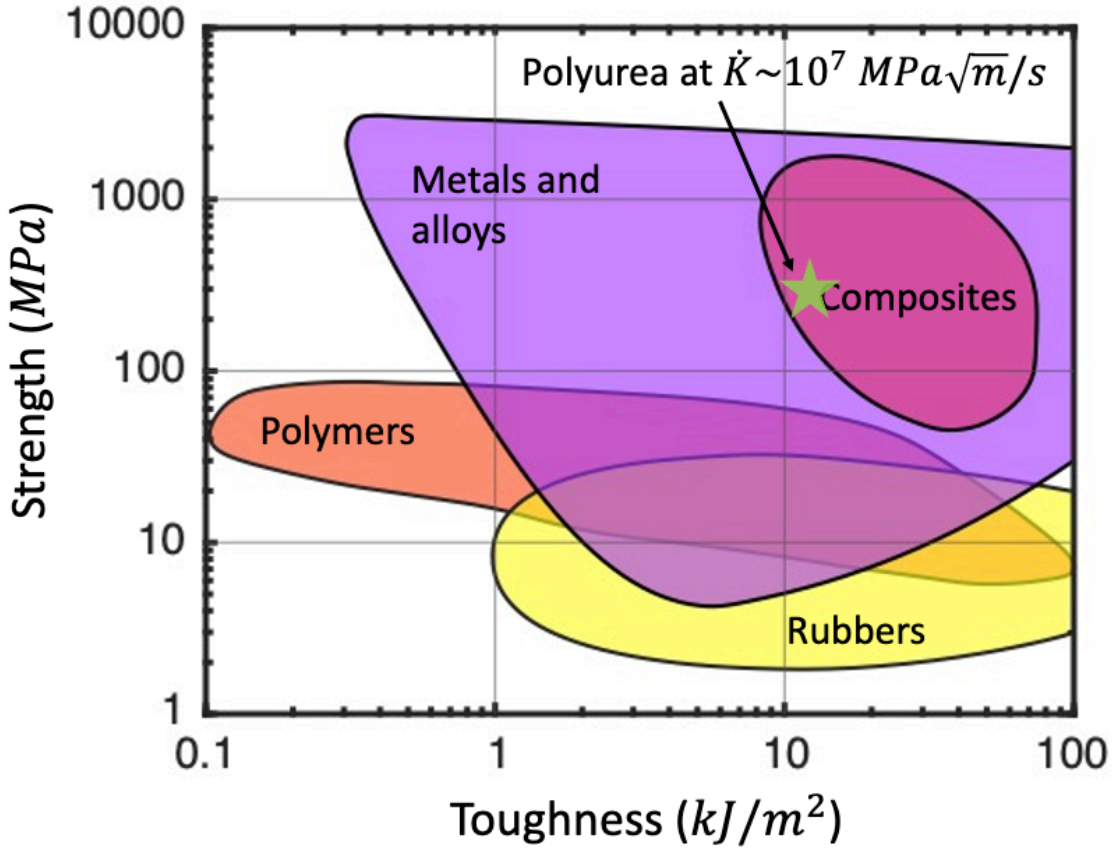

Figure 3.15 High dynamic fracture toughness of polyurea at a high crack-tip loading rate plotted on an Ashby diagram (Ashby, 2012).

3.5 Conclusion

In this Chapter, the dynamic toughness of polyurea PU1000 was successfully measured from a big-data-generating experiment with our newly invented DL-ISI, applying plane-wave loading of a mid-cracked specimen with plate impact. The experimental DL-ISI fringe inpainting is enabled from a state-of-art cGAN model pre-trained with a corresponding FEM dataset. The dynamic fracture toughness is measured as $G_c =$

$12100 \pm 1100 J/m^2$ under a very high crack-tip loading rate, $\dot{K} \sim 10^7 MPa\sqrt{m}/s$. Apparent dynamic toughening is found in polyurea where the cohesive strength under the crack-tip loading rate, $\sigma_c = 294MPa$, is found to be nearly three times higher than the spall strength ~105 MPa under the symmetric impact with the same impact speed. These experimental results fill the gap in the current understanding of copolymer's cooperative failure strength under extreme local conditions near the crack tip. The underlying strengthening mechanisms will be investigated through molecular-level experiments as well as mesoscale simulations in **Chapter 4**. We also believe the framework of this big-data-generating experiment could steer the future direction on experimental mechanics, which combines the innovative high-throughput experimental techniques with state-of-the-art machine learning algorithms for the next-level material design and characterization.

Appendix 3.A

Linear elastic fracture mechanics (LEFM) estimation of dynamic fracture toughness

From the linear elastic fracture mechanics (LEFM) theory, the Mode I crack-tip stress intensity factor as a function of time under a step loading of normal tensile wave can be expressed as (Freund, 1998),

$$K_I(t) = n(\nu)\sigma_0 C_l^{1/2} t^{1/2} \qquad (A.1)$$

where $n(\nu) = \frac{2}{1-\nu}\left(\frac{1-2\nu}{\pi}\right)^{\frac{1}{2}}$ with Poisson's ratio $\nu = 0.4$ is the blunt factor, $\sigma_0 = \frac{1}{2}\rho C_l V_0$ is the incident normal stress with density $\rho = 1070\ kg/m^3$ and impact velocity $V_0 = 204m/s$. $C_l = \left(\frac{E_G}{\rho(1-\nu^2)}\right)^{1/2} = 2100m/s$ is the longitudinal wave speed. At a critical time τ, the crack is assumed to initiate, the critical Mode I stress intensity factor K_{IC} can be expressed as,

$$K_{IC} = n(\nu)\sigma_0 C_l^{1/2} \tau^{1/2} \qquad (A.2)$$

Therefore, the toughness G_c under plane-strain condition is expressed as,

$$G_c = \frac{(1-\nu^2)K_{IC}^2}{E_G} \qquad (A.3)$$

Where $E_G = 3.96GPa$ is Young's modulus of the polyurea under tensile stress. From FEM, the incubation time of crack-growth initiation is $\tau = 0.8\mu s$. Therefore, the linear elastic fracture mechanics (LEFM) estimation of the toughness provides $G_c^{LEFM} = 13418.62J/m^2$.

Appendix 3.B

Detailed cGAN model

Table 3.B.1 Detailed U-Net Generator architecture.

Layer	Layer structure	Output shape
1	Input layer	(128, 128, 1)
2	Conv2D + LeakyReLU(alpha=0.2)	(64, 64, 64)
3	Conv2D + BatchNomalization + LeakyReLU(alpha=0.2)	(32, 32, 128)
4	Conv2D + BatchNomalization + LeakyReLU(alpha=0.2)	(16, 16, 256)
5	Conv2D + BatchNomalization + LeakyReLU(alpha=0.2)	(8, 8, 512)
6	Conv2D + BatchNomalization + LeakyReLU(alpha=0.2)	(4, 4, 512)
7	Conv2D + BatchNomalization + LeakyReLU(alpha=0.2)	(2, 2, 512)
8	Conv2D + BatchNomalization + LeakyReLU(alpha=0.2)	(1, 1, 512)
9	UpSampling2D + Conv2D + BatchNomalization	(2, 2, 1024)
10	UpSampling2D + Conv2D +BatchNomalization	(4, 4, 1024)
11	UpSampling2D + Conv2D +BatchNomalization	(8, 8, 1024)
12	UpSampling2D + Conv2D +BatchNomalization	(16, 16, 512)
13	UpSampling2D + Conv2D +BatchNomalization	(32, 32, 256)
14	UpSampling2D + Conv2D +BatchNomalization	(64, 64, 128)
15	Output layer	(128, 128, 1)

Table 3.B.2 Detailed PatchGAN Discriminator architecture.

Layer	Layer structure	Output shape
1	Concatenate layer	(128, 128, 2)
2	Conv2D + LeakyReLU (alpha=0.2)	(64, 64, 64)
3	Conv2D + BatchNomalization + LeakyReLU (alpha=0.2)	(32, 32, 128)
4	Conv2D + BatchNomalization + LeakyReLU (alpha=0.2)	(16, 16, 256)
5	Conv2D + BatchNomalization + LeakyReLU (alpha=0.2)	(8, 8, 512)
6	Conv2D	(8, 8, 1)

*Layer structure uses the abbreviate terminology in TensorFlow 2.5.

Appendix 3.C

Train and predict performance of CNN model on the polyurea FEM dataset

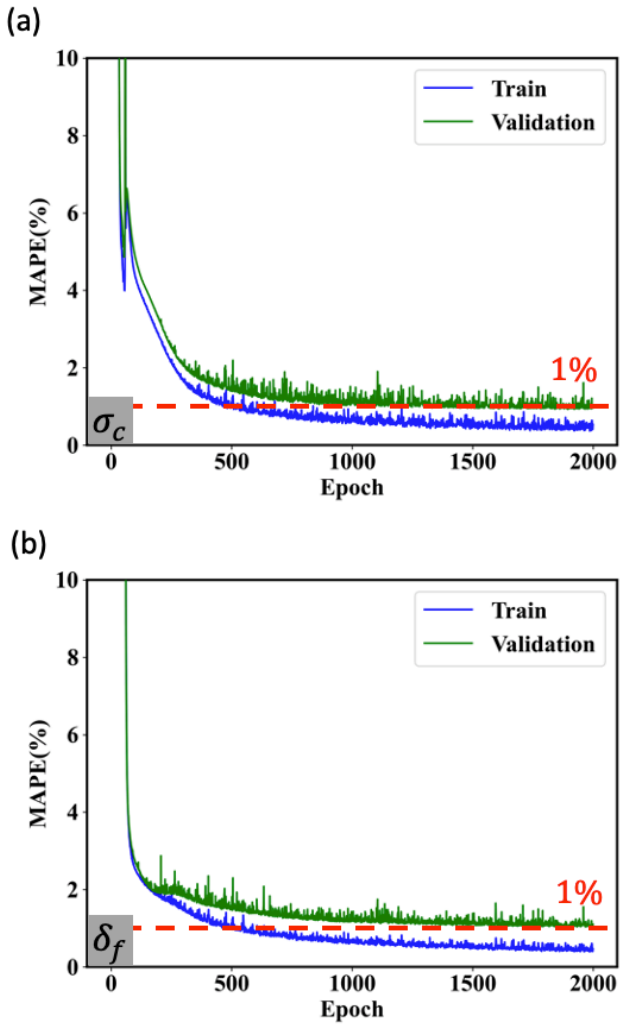

Figure 3.C.1 The Mean Absolute Percentage Error (MAPE) of training and validation datasets as a function of train epoch for (a) σ_c, and (b) δ_f with total number of 961 FEM datasets.

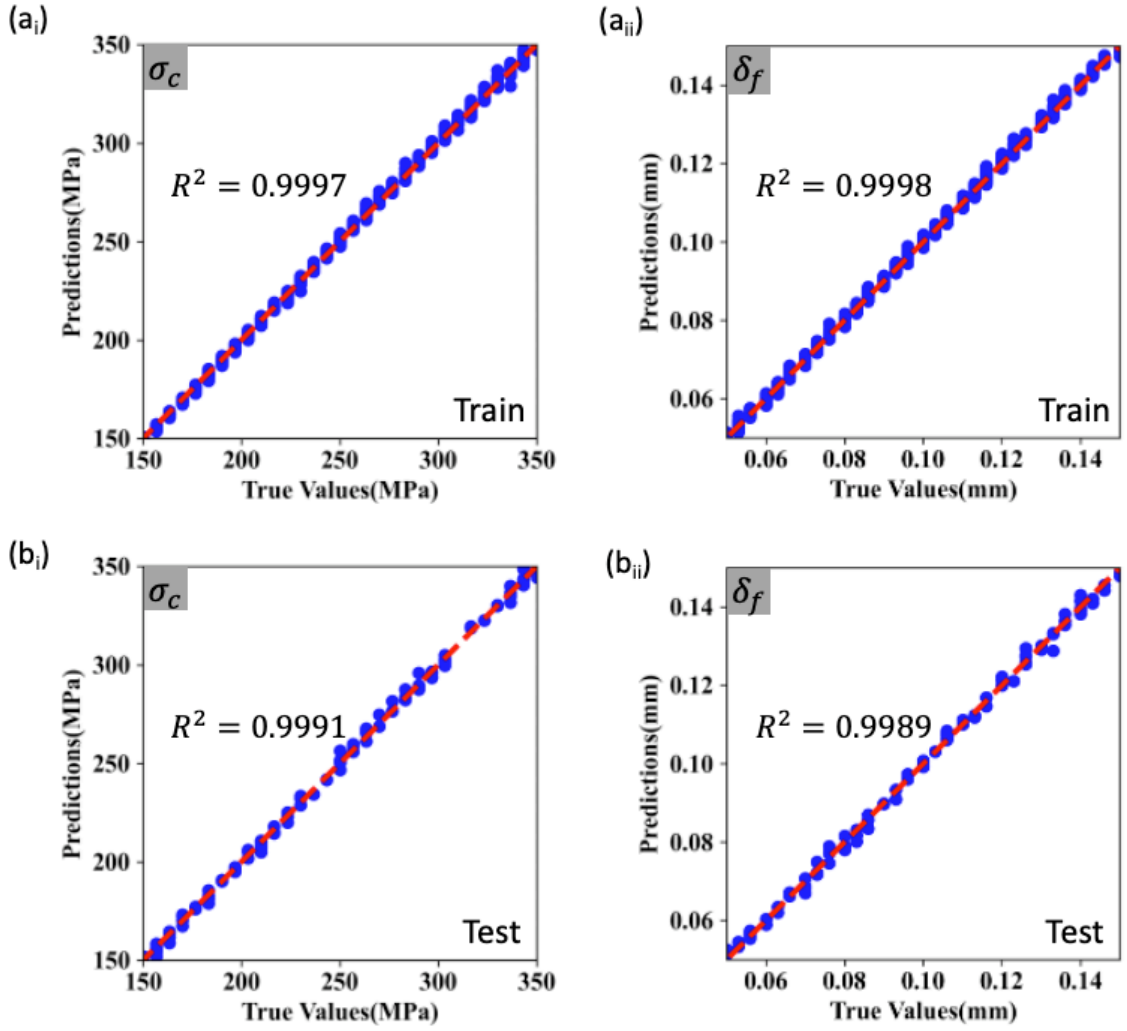

Figure 3.C.2 Prediction preformation of cohesive parameters on training datasets for (a_i) σ_c, and (a_{ii}) δ_f, and testing datasets for (b_i) σ_c, and (b_{ii}) δ_f.

Appendix 3.D

DL-ISI fringe sensitivity on the detailed cohesive laws

Cohesive law	Bilinear	Trapezoid	Exponential
Schematics	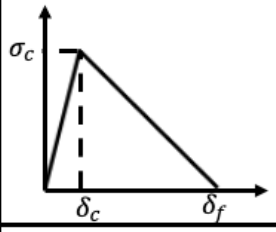	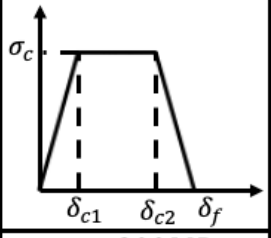	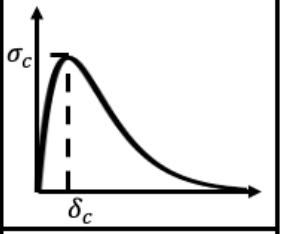
Cohesive parameters	$\sigma_c = 300MPa$ $\delta_f = 0.08mm$ $\delta_c = 0.2\delta_f$	$\sigma_c = 300MPa$ $\delta_f = 0.053mm$ $\delta_{c1} = 0.25\delta_f$ $\delta_{c2} = 0.75\delta_f$	$\sigma_c = 300MPa$ $\delta_f = 0.015mm$
Fracture toughness	$G_c = 12000J/m^2$		
DL-ISI fringes	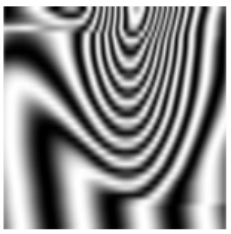	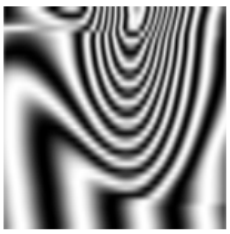	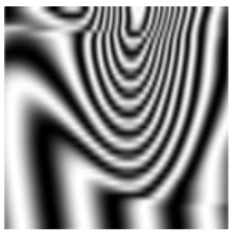
Correlation	1.0	0.9909	0.9807
Wall time	10.8s	9.8s	18.3s

Figure 3.D.1 DL-ISI fringe images from FEM simulations with 3 different cohesive laws: bilinear, trapezoid, and exponential laws with the same fracture energy.

Chapter 4

Nanophase fragmentation and self-healing of a block copolymer under deformation: *in-situ* AFM experiments and mesoscale simulations

Note: Part of the experimental results in this chapter has been presented by the author and is to be published in the Society of Experimental Mechanics (SEM) 2021 conference proceedings. The *in-situ* AFM loading device was designed and manufactured in collaboration with Catherine Machnicki and John Hegarty. The polyurea thin film was made by Catherine Machnicki.

4.1 Introduction

Polyurea is a multiblock copolymer that possesses exceptional chemo-mechanical properties like fast reactivity for casting and ballistic resistance under the dynamic impact (Barsoum, 2015; Bogoslovov et al., 2007; Grujicic et al., 2015). During the linear polymerization, thermodynamic incompatibility between the polytetramethylene oxide and diisocyanate enables the unique bicontinuous nanostructures consisting of hard arms with

high aspect ratio dispersed in a continuous soft medium, as observed in Atomic Force Microscopy (AFM) tapping-mode phase images (Das et al., 2007; Grujicic et al., 2014a; Kim et al., 2021; Wisse et al., 2006). This interesting bicontinuous nanostructure is believed to contribute to the unusual dynamic fracture toughness of polyurea, as discussed in **Chapter 3**. However, it is not well understood how the partitioning of load and deformation carrying capacities between hard and soft segments, which enables the spreading of inelastic finite deformation without localization. To get some insights on inelastic deformation mechanisms of the nanophase aggregates, small- and wide-angle X-ray scattering (SAXS/WAXS) experiments caused by nano and microstructural evolution was observed during the tensile deformation of polyurea (Choi et al., 2012; Pathak et al., 2008; Rinaldi et al., 2011). Pathak et al. (Pathak et al., 2008) found that under the quasi-static loading, polyurea develops strong anisotropy in average interdomain spacing while under loading with a relatively high strain rate, polyurea develops isotropy in domain spacing. Subsequently, Rinaldi et al. (Rinaldi et al.) found from their *in-situ* SAXS that the hard domain will disassociate at the strain ~0.4 under the quasi-static loading, and this breakage is believed to be the governing mechanism of energy dissipation during tensile loading. However, the X-ray scattering data primarily provided average hard domain and intermolecular spacings and their average anisotropic orientations but could not provide information on nanoscale inhomogeneous deformation characteristics of supramolecular interactions and configurational motions of inelastic deformation carriers. Therefore, tracing the nano-structural evolution with a nanometer-scale spatial resolution is desired to uncover the interplay between the hard/soft-phase load/deformation sharing characteristics

and dynamic-bond characteristics of supramolecular interactions in a submicron-size observation window.

However, we have two significant experimental difficulties. One is drifting off the *in-situ* observation sight due to micron-scale displacements made by specimen deformation and loading-frame motion. The other is the loss of inter-frame image correlations caused by breaking and reforming dynamic-bond characteristics of the supramolecular interactions. Various *in-situ* AFM loading devices have been previously designed to avoid the examination-sight drifting of the observation window during the loading process, employing either mechanical (Bamberg et al., 2006; DebenUK, 2021; Tambe and Bhushan, 2004) or electrical control schemes. In the mechanical control scheme, typically, a twin-screw composed of left- and right-handed screws of the same pitch were threaded on a single driving shaft and driven by a stepper motor to stretch the specimen symmetrically, keeping the specimen centered in the field of view. The mechanical passive control device allowed observation of specimen deformation or cracking processes approximately near the stationary-point vicinity, within an observation window of $3\mu m \times 3\mu m$ (Bamberg et al., 2006) or $20\mu m \times 20\mu m$ (Tambe and Bhushan, 2004). However, the devices could not keep inter-frame correlations to trace the same material points. The uncertainty of the displacement that makes the material points move out of the observation window was too large to track the Lagrangian material deformation characteristics.

Here, we designed and manufactured a twin-screw-driven *in-situ* AFM loading device and analyzed the uncertainty of the device's material-point traceability by investigating AFM topography's Digital Image Correlation (DIC) within $10\mu m \times 10\mu m$ windows and AFM tapping phase's spectral evolution within $1\mu m \times 1\mu m$ windows. Then,

we studied the loading device characteristics by analyzing the DIC of AFM topography images of the sample under several stepping increments of small strains within $10\mu m \times 10\mu m$ windows. Then, we investigated deformation characteristics of the phase segregated nanostructures with high-resolution *in-situ* AFM-tapping-mode phase images and their spectral characteristics within $1\mu m \times 1\mu m$ windows during stress-relaxation at various strain levels up to 265% using the home-made *in-situ* AFM loading device. The nanophase relaxation test removes the uncertainty of the observation-sight motion caused by the loading-device operation since the device operation was frozen during the entire relaxation process. However, material drifting could be possible due to the local domain evolution during the relaxation process. The study of transient nanophase relaxation at different strain levels could help our understanding of the dynamic and self-healing properties of segmented block copolymers.

Coarse-grained mesoscale simulations were also conducted to assist our understanding of the load partitioning roles and deformation carrying capacities between hard and soft segments in the domain evolution process. The current simulation studies of polyurea can be categorized into two parts, the all-atom simulations (Grujicic et al., 2011a; Grujicic et al., 2015; Grujicic et al., 2012; Heyden et al., 2016; Manav and Ortiz, 2021) and the coarse-grained simulations (Agrawal et al., 2014; Agrawal et al., 2016; Arman et al., 2012; Grujicic et al., 2014b; Liu and Oswald, 2019; Yao et al., 2020). All-atom simulations (Heyden et al., 2016) with periodical simulation box size usually smaller than 5nm could found the Hugoniot curve agrees well with the experimental results from plate impact experiments (Jiao and Clifton, 2014). However, the length and time scales of all-atom simulations are limited. To study the structural evolution of the hard domain during

deformation, we need a simulation box with a size at least larger than the characteristic length scale of polyurea. Therefore, the coarse-grained simulation method is usually used to study the structural property of polyurea. Generic Kremer-Grest (KG) bead-spring model (Cui and Brinson, 2013; Kremer and Grest, 1990) or dissipative particle dynamic (DPD) method have been used to study the phase-separated morphologies of polyurea (Sami et al., 2014). Later, the iterative Boltzmann inversion (IBI) method was used to obtain the coarse-grained potential parameters from equilibrium ensembles (Agrawal et al., 2014; Liu and Oswald, 2019). However, none of the current coarse-grained models could address the fragmentation process of the hard domain due to the dynamic hydrogen bonding process which is observed in our AFM experiments. Therefore, in this chapter, we developed a systematic coarse-grain simulation method that could reveal the dynamic bonding process during deformation.

4.2 Experiments

4.2.1 *in-situ* AFM loading device with displacement invariance control

A homemade *in-situ* AFM loading device driven by twin screws to self-align observation sights has been designed and assembled. The schematics of the device mounted on a base (1) are illustrated in **Fig.4.1**. A left- and right-hand threaded leadscrew (3) with pitch size 0.8mm is fabricated from a brass rod with a diameter of 4mm. A stepper motor (8) with 200 steps per rotation and operation torque 1.6 in.-oz. is used to precisely control the loading strains by transmitting the torque through one pair of gears (7) with the same teeth number. The motor is controlled by an A4988 motor driver, which is programmed by an

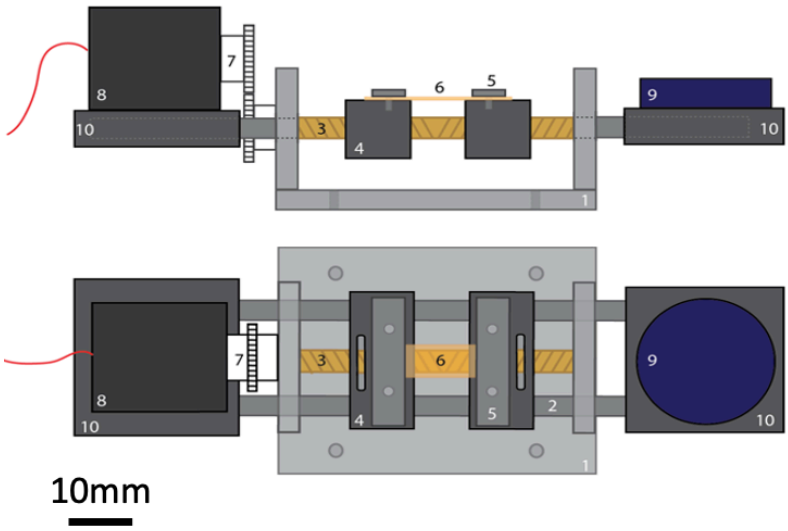

Item No.	Part Description	QTY.
1	Base	1
2	Guide Rod	2
3	Left/Right Threaded Lead Screw	1
4	Sample Holder	2
5	Sample Clamp	2
6	Thin Film	1
7	Gear	2
8	Stepper Motor	1
9	Counter Weight	1
10	Suspended Base	2

Figure 4.1 Schematics of *in-situ* AFM loading device with displacement invariance control.

Arduino chipboard. The finest strain resolution is calculated as 0.027%/step if the initial sample length is 30mm. Special beam spring anti-backlash base block (4) has been manufactured to reduce the backlash problem between the dual leadscrew and the sample holders sliding on two guide rods (2). A guide rod is not drawn in the side view to show the twin-screw clearly. A counterbalance weight (9) sits on a holding block (10) to balance the device on the AFM stage. A thin-film sample (6) is fixed to the holders firmly by clamps (5). A cushion block with knurl could be applied to remove potential slip between

the sample and the grips under large deformation. The maximum dimensions for the specimen are $30mm \times 10mm \times 1mm$. Our device is flexible to change the dual leadscrew with different pitch sizes and change the pair of gears for different accuracy requirements. In this chapter, as the device was primarily used to investigate the device-kinematics control and the sample's displacement fields in the observation window, an optical-gauge load cell was not applied in the device to measure the stress in the sample.

4.2.2 Polyurea thin film synthesis

Polyurea films were prepared by linear polymerization of 4,4'-methylene diphenyl diisocyanate (MDI) (Isonate 143L; Dow Chemical) and polytetramethylene oxide-di-p-aminobenzoate (Versalink P-1000; Air Products). Briefly, Versalink P-1000 was heated to approximately 80° C or until the viscosity of the oligomer was sufficiently decreased to allow for pouring. This was then added to a 500 mL beaker followed by the rapid addition of MDI in a 1:4 ratio (MDI to P-1000) by weight. Note that MDI was weighed with a 5% excess, as recommended by the manufacturer, to account for a possible side reaction between the diisocyanate moieties and the moisture in the ambient air. The mixture was stirred with a glass rod for 1 min and then degassed until visible bubbles were gone, for a maximum time of 10 minutes. Following degassing, approximately 5 mL of the curing mixture was added to a mold consisting of a Teflon™ plate with 200 μm thick tape around the edges for height guidance, producing film dimensions of 2.5 in × 4.5 in × 200 μm. With a glass rod or straight edge, the polyurea was spread across the Teflon™ mold. The casted polyurea was cured for at least 24 hours at room temperature in a desiccator cabinet

before use. The film was then cut into pieces for the AFM device or in a dog bone shape for tensile testing.

4.2.3 Digital Image Correlation (DIC) analysis of the *in-situ* loading system

We utilized a DIC of sequential AFM topography images of scan size 10μm×10μm to analyze the observation-sight displacement drifting made by successive loading steps of the stepper motor. We employed a q-factor-based digital image correlation algorithm (qDIC) (Landauer et al., 2018) for the displacement analysis, and the AFM DIC had ~5nm displacement resolution. **Fig.4.2(a_i)&(a_{ii})** show two selected frames of AFM surface-topography images before and after the specimen was stretched in two steps of the stepper motor. The end-to-end stretching displacement of the 5mm long specimen with 5mm width and 200μm thickness was 16μm between the two frames. The maximum square correlation window size was first identified approximately, and one image was translated close to the other image before they were correlated to get the additional fine adjustment of the total correlation displacement. The DIC analysis results of horizontal and vertical displacements are shown in **Fig.4.2(b_i)&(bii)**, respectively. The maximum correlation window size was 6.25μm ×6.25μm, and the two well recognizable images are marked with blue boxes. The observation-sight displacement was 0.10μm in the stretching direction and 3.53μm in the lateral direction between the two surface-topography images. From the DIC analysis of the *in-situ* loading system, the 0.10μm displacement of the observation sight in the stretching direction could be caused by the sample's stretching deformation and a 31.3 μm center-position misalignment of the AFM scanning window's center in the stretching direction.

However, 3.53 μm displacement in the lateral direction is too large to be made by a Poisson contraction and a center-position misalignment. Such a relatively large lateral displacement is likely made by relative shear and rotation between the specimen holders.

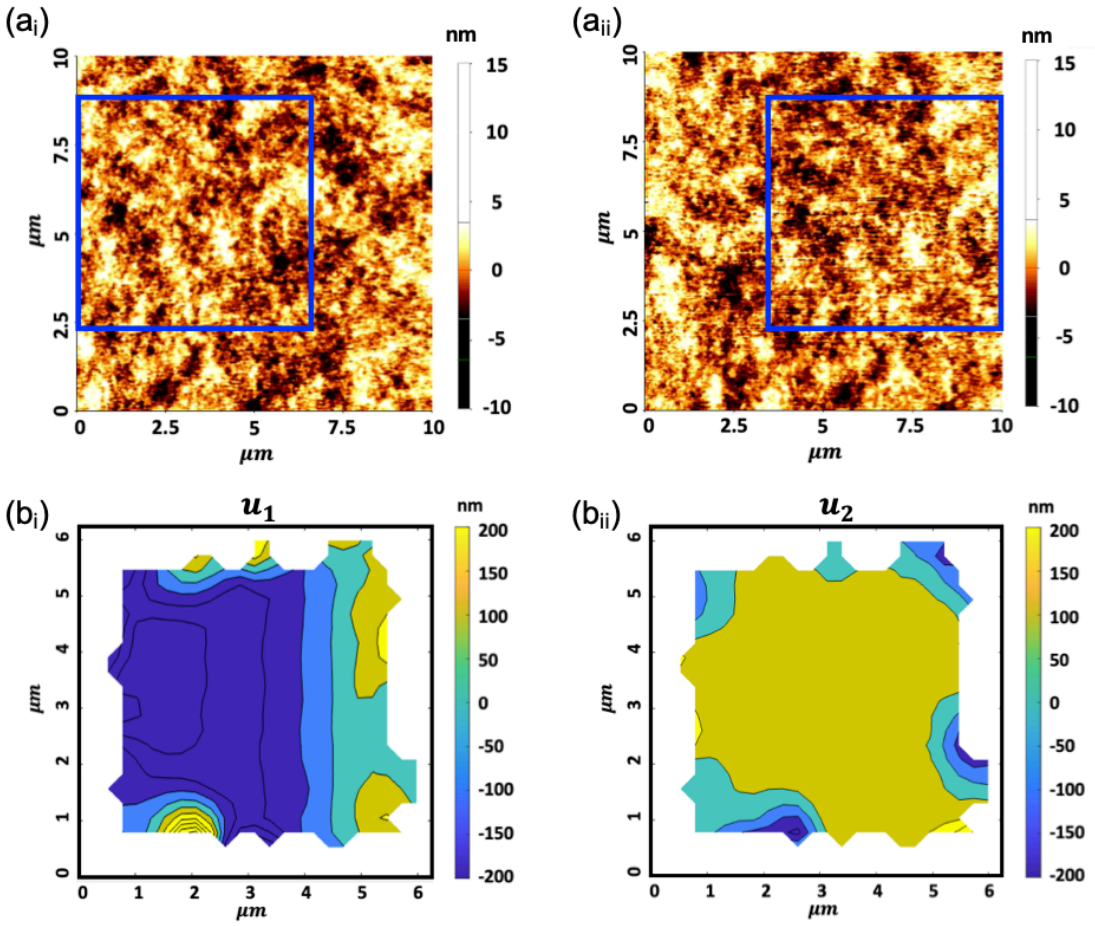

Figure 4.2 Sequential AFM topography images of scan size $10\mu m \times 10\mu m$ of a PU-1000 sample under tension in the vertical direction with tensile strains, (a_i) $\varepsilon = 0.32\%$ and (a_{ii}) $\varepsilon = 0.65\%$. The displacement plots obtained from DIC for horizontal (b_i) and vertical (b_{ii}) displacements.

The DIC analysis reveals that the twin-screw driving can keep the AFM observation site within the submicron-size window with ~10nm displacement/step-loading in the stretching direction if the center positioning accuracy of the AFM scanning window is

within ~10μm and the specimen length is reduced to 3mm. Analysis indicates that a similar control accuracy can be achieved with a slider's proper design to limit the sample holder's rotation. The DIC analysis also showed a sudden jump of observation-sight displacement at a large stretching step, presumably caused by a partial slip of the sample at a frictional grip. Besides, the DIC of AFM surface-topography images kept strong correlations, while the tapping-phase images quickly lost their correlations at a large strain. However, in our nanophase stress-relaxation experiment, these uncertainties of the observation window motion caused by the loading device are removed since the device operation was frozen during the entire relaxation process. Therefore, using the current *in-situ* AFM loading device with displacement invariance control to study the nanophase evolution of polyurea is valid. Here, we acquired sequential AFM-tapping-mode phase images of polyurea's nanophase evolution during relaxation under various fixed tensile strains from 0% up to 265%.

4.2.4 AFM tapping-mode imaging of polyurea nanophases under stress relaxation

The AFM tapping-mode phase and topography images were captured using XE-Bio AFM from Park Systems. Schematics of *in-situ* AFM tapping phase imaging of polyurea thin film under stretch are shown in **Fig.4.3(a)**. Immediate after a rapid step loading to each fixed strain ε(t) with strain rate ~$0.11s^{-1}$, the images with $1\mu m \times 1\mu m$ scan size were acquired successively at the same observation sight until reaching equilibrium morphologies. The time between step loading and AFM data acquisition is approximately 10s which includes the time needed to shut down the motor and approach the tip.

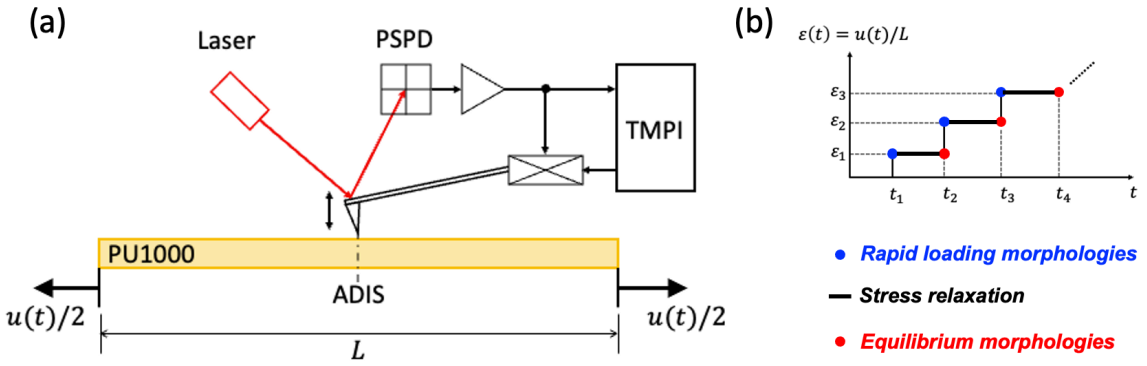

Figure 4.3 (a) Schematics of *in-situ* AFM tapping-mode phase imaging of polyurea thin film under symmetric displacement $u(t)$. PSPD is the abbreviation of Position-sensitive Photo Diode; TMPI is the abbreviation of Tapping Mode Phase Imaging; ADIS is the abbreviation of Displacement Invariance Sight. (b) Multi-step loading history from rapid loading to equilibrium through stress relaxation. The blue points represent the morphologies right after rapid loading; the red points represent the equilibrium morphologies at each fixed strain $\varepsilon(t)$.

The multi-step loading history is illustrated in **Fig.4.3(b)**. Images were taken at a fast-scanning frequency of 2Hz under ambient conditions, and the image pixel resolution was 256×256. Therefore, each image acquisition took roughly 2 minutes. The SuperSharpSilicon™ Non-Contact/Tapping-mode probes with reflective coatings (SSS-NCHR) from Nanosensors™ were used. This probe has a curvature radius of 2nm and a spring constant of 42 N/m. Compared with regular tapping-mode probes with a radius of curvature of 10nm, the SSS-NCHR tip could resolve the nanophases with higher resolution. The set-point ratio was tuned ~0.5 to get high-resolution phase images. The slow-scanning direction was aligned in the tensile direction to avoid vibration noise from the suspended

thin film. The controlling motor system was turned off during AFM scanning to prevent any electrical noises.

4.3 Simulation methods

In this section, the detailed coarse-grain simulation methods will be explained. Since the generic KG bead-spring model requires a relatively small timestep to ensure numerical convergence, we imposed a two-step simulation procedure to accelerate the simulation speed. In the first step, we applied the framework of dissipative particle dynamics (DPD) (Hoogerbrugge and Koelman, 1992) to obtain an equilibrated phase-separated structure with physical interaction parameters within a relatively short time. In the second step, we switched the DPD potential to more physical potentials and equilibrated the structure for next-step simulations.

4.3.1 Modeling of self-assembly morphology from Dissipative Particle Dynamics (DPD)

In our mesoscale molecular dynamics simulations, the phase separation processes of the copolymer were carried out based on the framework of DPD simulation. Since its original development (Hoogerbrugge and Koelman, 1992), DPD has been successfully applied to study the phase separation process of complex fluids including copolymers by correlating the conventional Flory-Huggins (FH) theory (Groot and Madden, 1998; Groot and Warren, 1997; Huang and Alexander-Katz, 2019). In the DPD framework, the polymers are

represented by generic bead-spring models. The equations of motion of each polymer bead read,

$$m_i \frac{d^2 r_i}{dt^2} = f_i = f_i^{int} + f_i^b, \tag{4.1}$$

where m_i, r_i, and f_i are the mass, coordinates, and force of the i th bead, respectively. f_i^{int} is the interaction force between beads as,

$$f_i^{int} = \sum_{i \neq j} F_{ij}^C + F_{ij}^D + F_{ij}^R, \tag{4.2}$$

F_{ij}^C is the soft interaction force along the bead center between two beads as follows,

$$F_{ij}^C = a_{ij} \omega(r_{ij}) \hat{r}_{ij}, \tag{4.3}$$

where a_{ij} is the maximum repulsion and $\hat{r}_{ij}$ is the unit directional vector between two beads. $\omega(r_{ij})$ is the weight function with r_c the cut-off distance as,

$$\omega(r_{ij}) = \begin{cases} 1 - \dfrac{r_{ij}}{r_c}, & r_{ij} < r_c \\ 0, & r_{ij} > r_c \end{cases}. \tag{4.4}$$

F_{ij}^D is the dissipative force which is proportional to the relative bead velocity v_{ij}, effectively dissipates the kinetic energy as,

$$F_{ij}^D = -\gamma \omega^2(r_{ij}) (\hat{r}_{ij} \cdot v_{ij}) \hat{r}_{ij}, \tag{4.5}$$

where γ is the viscosity coefficient. To compensate the dissipated energy, a random force F_{ij}^R is applied to reach thermal equilibrium as,

$$F_{ij}^R = \sigma \omega(r_{ij}) \xi_{ij} \Delta t^{1/2} \, \hat{r}_{ij}, \tag{4.6}$$

where ξ_{ij} is a random variable and Δt is the time step. σ is related to γ as $\sigma^2 = 2\gamma k_B T$ to satisfy the fluctuation-dissipation requirement (Hoogerbrugge and Koelman, 1992). Here, k_B is the Boltzmann constant and T is the temperature. In this chapter, reduced units were adopted in the simulations where the unit thermal energy $\epsilon = k_B T$, and cutoff radius r_c are

set as unity. The standard values with $\sigma = 3.0$ and $\gamma = 4.5$ were used. $f_i^b = \sum_{i \neq j} F_{ij}^b$ is the spring force between two connected beads as,

$$F_{ij}^b = K_{harm}\left(1 - \frac{r_{ij}}{r_0}\right)\hat{r}_{ij}, \tag{4.7}$$

where bond strength $K_{harm} = 4\epsilon$ and equilibrium bond length $r_0 = 0.86r_c$ were used (Groot and Madden, 1998). The conservative force parameter a_{ij} can be directly corelated with Flory–Huggins (FH) parameters χ between two beads as (Groot and Madden, 1998),

$$a_{ij} = a_{ii} + 3.27\chi, \tag{4.8}$$

where $a_{ii}\rho = 75k_BT$ is the conservative force parameter between beads of the same type. Here, $\rho = 3$ is chosen as the bead number density. As a convention in the DPD method, we assume a_{ii} is the same between two beads of the same type since the phase separation process is dominated by the interaction potential between two different types of beads, i.e., FH parameter χ. The FH parameter between soft and hard domains for polyurea, χ_{PU}, was calculated as 5.42 from quantum mechanical calculations on their solubility (Grujicic et al., 2011b).

To keep the similar volume of DPD beads, we divided each repeated polyurea chain into 2 hard beads (H) and 7 soft beads (S) with each bead volume $V_b = 270A^3$, as shown in **Fig.4.4(a)**. Therefore, the reduced distance unit r_c can be linked to physical length as $r_c = (\rho V_b)^{1/3} = 0.929nm$. The mass ratio between each hard bead, m_H, and soft bead, m_S, is 1.4:1. The physical density was calculated as $1.045g/cm^3$, which is within the range of 1.04~1.07 g/cm^3 measured in experiments. The simulation cell size was $50r_c \times 50r_c \times 50r_c$ with a total of 375,000 beads. The monodisperse copolymer model was prepared by keeping the degree of polymerization (DP), $N = 8$, while the polydisperse model was built from a lognormal distribution according to the experimental measurement

(Li et al., 2019). The resultant polydisperse model had the number average molecular weight, $M_n = 12693 g/mol$, and the weight average molecular weight $M_w = 19303 g/mol$, with the Polydispersity Index (PDI), $PDI = 1.52$. The number of chains as a function of DP for the polydisperse model is shown in **Fig.4.4(b)**. Periodical boundary conditions were employed in three directions. The simulations were carried out on the Large-scale Atomic/Molecular Massively Parallel Simulator (LAMMPS) (Plimpton, 1995), where the velocity-Verlet integration algorithm was used to solve the equations of motion. The Nose-Hoover thermostat was applied to maintain the constant temperature condition. The simulation time step was 0.02, and the total simulation time was 20000τ. This simulation time was sufficiently long to reach equilibrium configuration verified by checking the convergence of radius of gyration of each chain.

The equilibrium morphologies from the DPD simulation for the polydisperse model and monodisperse model are shown in **Fig.4.4(c)&(d)**, respectively. The red beads represent the soft matrix, while the blue beads represent the hard domain. For clear visualization, the radius of hard beads was set to be twice the radius of soft beads. To quantify the structural properties like the average interdomain spacing of polyurea, the radial distribution functions $g(r)$ of the hard domains for these two models are plotted in **Fig.4.4(e)**. Both models show a secondary peak on $g(r)$ at $r = 7.25 r_c$ $(6.74 nm)$. This characteristic distance represents the averaged interdomain spacing, which is close to the experimental measurement from SAXS, $d_{SAXS} = 7.14 nm$ (Choi et al., 2012). Interestingly, the effect of polydispersity has a bare effect on the average interdomain structure as g(r) are almost identical for these two models. That is to say, the statistical structural morphology is mainly dependent on the interaction parameter χ. However, the

polydispersity may contribute to the hierarchical clustering observed in a 500nm × 500nm AFM tapping phase image. Unfortunately, the current simulation box with ~ 50nm size could not reveal this aspect.

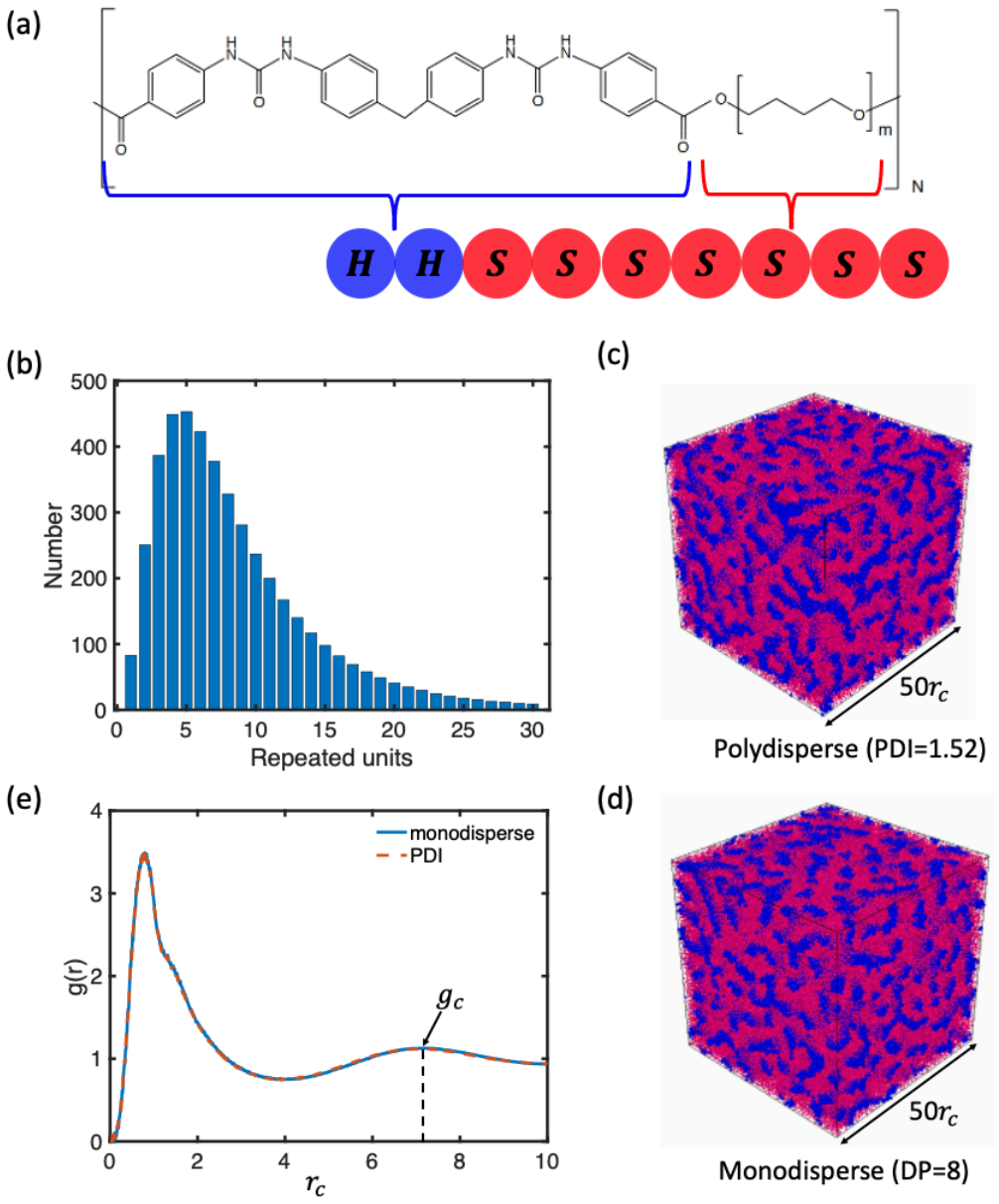

Figure 4.4 (a) Coarse-grained bead mapping scheme of polyurea; (b) The chain distribution in the built polydisperse model with PDI=1.52; the equilibrium morphology for (c) polydisperse and (d) monodisperse model after DPD simulation; (e) the radial distribution functions $g(r)$ of the hard domains for these two models.

4.3.2 Potential switch for the nanodomain evolution process

DPD ensemble could obtain the equilibrated copolymer morphology faster than the conventional MD method due to its soft interaction potential. However, the soft potential could not represent the correct forcefield between polymer beads. Therefore, to study the deformation mechanisms of the copolymer, it is desired to switch to more physical potentials once the equilibrated morphology was obtained from the DPD method. Here, after obtaining equilibrium structure from the DPD method, we switched the non-bonded interaction potential from DPD to standard Lennard-Jones (LJ) potential with cutoff distance $r_c^{lj} = 2.5\sigma$,

$$U_{LJ}(r) = 4\epsilon\left[\left(\frac{\sigma}{r}\right)^{12} - \left(\frac{\sigma}{r}\right)^{6}\right]. \tag{4.9}$$

To match with physical units obtained from all-atom simulations (Agrawal et al., 2016), $\epsilon_{SS} = 0.25\ Kcal/mol$ was chosen for the energy well depth between soft beads, and $\epsilon_{HH} = 1.0Kcal/mol$ for hard beads. Hence, $\epsilon_{SH} = \sqrt{\epsilon_{SS}\epsilon_{HH}} = 0.5Kcal/mol$. To keep the density after the potential switch, $\sigma = 0.7r_c$ was chosen for all beads. The fundamental units were chosen as, $r_c = 1$ for length, $\epsilon = k_BT = 1$ for energy, $m_s = 1$ for mass, and $k_B = 1$ for Boltzmann constant. Therefore, the unit energy is $0.6Kcal/mol$, and the unit length is $0.929nm$. The potential between bonded beads was switched to the combination of finite extensible nonlinear elastic (FENE) potential and Weeks-Chandler-Andersen (WCA) potential, as

$$U_{bond}(r) = -\frac{1}{2}K_{FENE}r_\infty^2\, ln\left[1 - \left(\frac{r}{r_\infty}\right)^2\right] + 4\epsilon\left[\left(\frac{\sigma}{r}\right)^{12} - \left(\frac{\sigma}{r}\right)^{6}\right] + \epsilon. \tag{4.10}$$

The convention value $K_{FENE} = 30\epsilon/\sigma^2$, and $r_\infty = 1.5\sigma$ were adopted here (Kremer and Grest, 1990). According to the Fourier transform infrared spectroscopy (FTIR) measurement (Li et al., 2018), 56% of carbonyls in the hard domains are linked with hydrogen bonds. These hydrogen bonds facilitate the formation of hard domains, which act as the physical crosslinkers in the copolymer. To simulate the dynamic hydrogen bonds in polyurea, an additional morse potential was applied between hard beads as,

$$U_{morse}(r) = D_0\left[e^{-2\alpha(r-r_0^{morse})} - 2e^{-\alpha(r-r_0^{morse})}\right], r < r_{cut}^{morse}, \quad (4.11)$$

where $D_0 = 14Kcal/mol$ was chosen according to quantum mechanical calculation (Yilgor et al., 2002). It is worth noting that hydrogen bonds are typically directional, which means there are preference angles between acceptors and donors when forming the hydrogen bonds. However, molecular-level details such as exact locations of the acceptors and donors at the fine time scale is typically averaged over a coarse time step in the coarse-grain simulations. The dynamic hydrogen bonding process of breakage and re-formation occurs within an ultra-fast time scale, typically in a lifetime of picosecond (Keutsch and Saykally, 2001), which is one order of smaller than the unit time, ~10ps in our coarse-grain simulations. Furthermore, much of the admissible bond direction is limited by the neighboring covalent bonds. Therefore, it is reasonable to assume in our simulations that the directionality and the probability of the dynamic hydrogen bonding process is averaged out by the Morse potential. All potential parameters in the mesoscale simulation are listed in **Table 4.1**.

The system was first equilibrated under an isothermal–isobaric (NPT) ensemble with zero pressure for $10^3\tau$ with time step 0.01τ. The physical unit for time τ is $\sigma\sqrt{m_s/\epsilon} = 7.31ps$. Then, the chemical crosslinking process was conducted by creating

one additional FENE bond between 10% of total hard beads within $10^3\tau$. The crosslinked system was relaxed for $10^4\tau$ to reach equilibrium with time step 0.001τ. When simulating the uniaxial tensile test, constant strain rate $10^{-3}\tau^{-1}$ ($\sim 10^8 s^{-1}$) was applied on the deformation direction, while zero pressure condition was enforced on the other two directions in the NPT ensemble.

Table 4.1 Coarse-grain simulation potential parameters for polyurea

(1) Between bonded beads: WCA+FENE potential

FENE bond stiffness between S-S beads	K_{SS}	$30\epsilon_{HH}/\sigma^2$
FENE bond stiffness between H-H beads	K_{HH}	$30\epsilon_{SS}/\sigma^2$
FENE bond stiffness between H-S beads	K_{HS}	$30\epsilon_{HS}/\sigma^2$
The maximum extensive distance for FENE	R_0^{FENE}	1.5σ
WCA cohesive energy between S-S beads	ϵ_{SS}	0.42ϵ
WCA cohesive energy between H-H beads	ϵ_{HH}	1.67ϵ
WCA cohesive energy between H-S beads	ϵ_{HS}	0.8375ϵ
WCA distance	σ	$0.70r_c$

(2) Between non-bonded beads: LJ potential

LJ cohesive energy between S-S beads	ϵ_{SS}	0.42ϵ
LJ cohesive energy between H-H beads	ϵ_{HH}	1.67ϵ
LJ cohesive energy between H-S beads	ϵ_{HS}	$0.8375\ \epsilon$
LJ distance	σ	$0.70r_c$
LJ cutoff	r_{cut}^{LJ}	$2.5r_c$

(3) Between Hard beads: Morse potential

Morse potential strength	D_0	23.3ϵ
Morse potential width	α	$3r_c^{-1}$
Morse potential equilibrium distance	r_0^{morse}	$0.79r_c$
Morse potential cutoff	r_{cut}^{morse}	$1.20r_c$

4.4 Results and Discussions

4.4.1 Strain induced anisotropic hard-domain coarsening in equilibrium morphologies

Figure 4.5 shows six *in-situ* AFM tapping-mode phase images of fully relaxed nanostructures of a thin polyurea film in equilibrium with scan size $1\mu m \times 1\mu m$ under a few fixed stretching strains ranging from 0% to 264%. The sample was stretched rapidly with a strain rate $\sim 0.11 s^{-1}$ to each strain level, and the strain was held fixed while the stress was partially relaxed, and the nanophases reached equilibrium at the strain level. Each image was acquired at least 30 minutes after the sample was stretched to the strain level to ensure the nanophases were fully relaxed to reach the equilibrium at the strain level, except for **Fig.4.5(b)**, where the image was scanned at 18 minutes after the stretch. **Fig.4.5(a)** shows the AFM tapping-phase image of the undeformed nanostructures, revealing morphological phases of the nanostructures. The bright region represents the hard domain, which is rod-shaped with ~15 nm diameter and a couple of hundred-nanometer lengths. The dark region represents the soft diamine group matrix. As the stretch strain increased, the nanostructures evolved during the relaxation process; the more coarsened hard domains, the more aligned towards the stretch direction at large strains, as seen in **Fig.4.5(b)-(f)**. *In-situ* WAXS/SAXS study (Rinaldi et al., 2011) also suggested such nano-structural evolution.

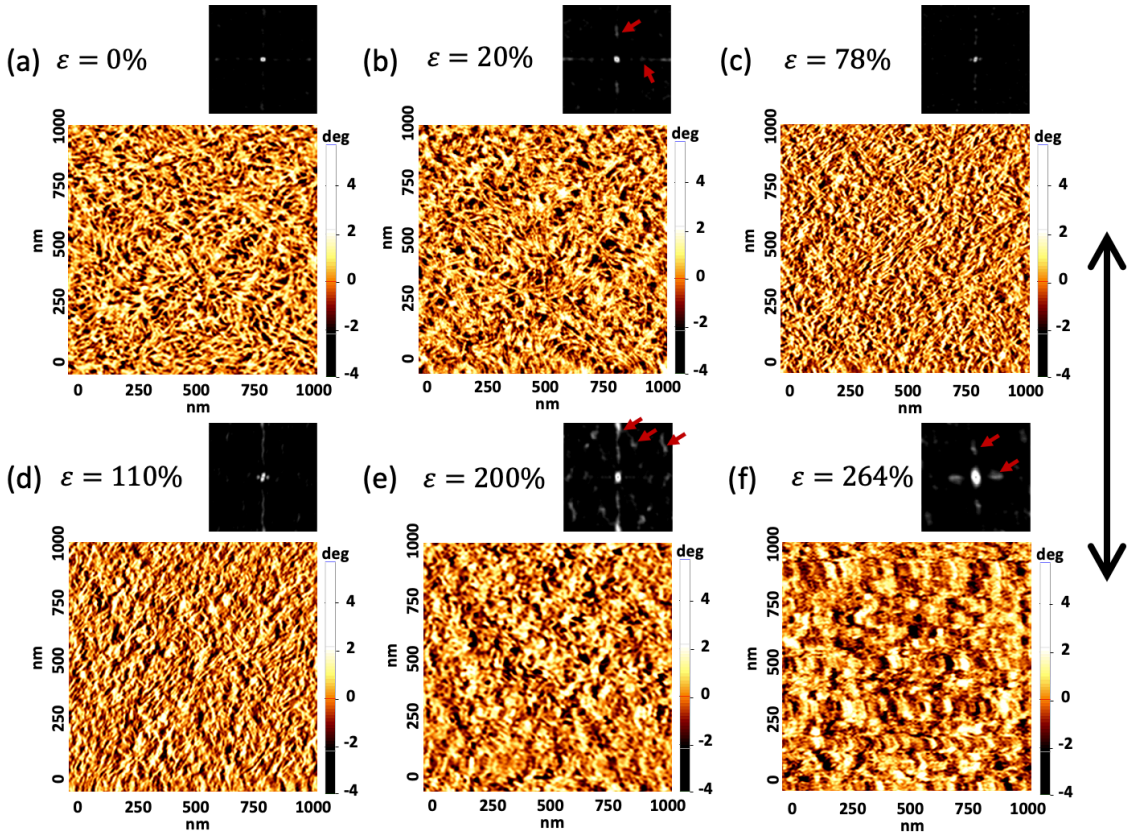

Figure 4.5 AFM tapping-mode phase images of a polyurea thin film under various strains at equilibrium with scan size $1\mu m \times 1\mu m$ for (a) $\varepsilon = 0\%$, (b) $\varepsilon = 20\%$, (c) $\varepsilon = 78\%$, (d) $\varepsilon = 110\%$, (e) $\varepsilon = 200\%$, and (f) $\varepsilon = 264\%$. The loading direction is indicated by the black arrow. The image-autocorrelation of each phase image with size $500nm \times 500nm$ is plotted. Distinct long-range peaks in autocorrelation images are indicated by red arrows.

To quantify the anisotropic hard-domain-size coarsening as well as detect the domain-clustering phenomenon as strain increases, we calculated the image autocorrelation of each phase image as,

$$A(\xi, \eta) = \iint \bar{I}(x, y)\bar{I}(x - \xi, y - \eta)dxdy, \tag{4.12}$$

where $\bar{I}(x, y)$ is the zero-mean intensity at image position (x, y), and (ξ, η) is the position at the autocorrelation displacement. The image autocorrelations are plotted in **Fig.4.5** as

well. For visualization purposes, $-250\text{nm} < \xi, \eta < 250\text{nm}$ is chosen in all autocorrelation images in this chapter to distinguish the central peak. The average domain size was then identified as half of the central peak's diameter.

As shown in the autocorrelation plots, strong directional-size anisotropy of hard domains is observed in the stretch and transverse directions as the strain increases. The identified directional domain-size evolution in the stretch and transverse directions is plotted in **Fig.4.6**. The average domain size increased from 11nm to 26nm in the stretch direction, while the average domain size in the transverse direction remained 10~13nm, as the strain increased to 200%. In addition to the coarsening of individual hard domains, the nanophases formed clusters in equilibrium at each strain level when the polyurea deforms beyond yielding ($\varepsilon > 15\%$). The clustering periodicity can be revealed by the long-range peaks in the autocorrelation images. As indicated by the red arrows in **Fig.4.5(b)**, secondary peaks ~130nm away from the center are distinctly observed in both directions, which characterizes the average inter-clustering spacing. As strain increased to 200%, more distinct peaks with different long-range distances are observed, as shown in **Fig.4.5(e)**, which indicates the hierarchical clusters with different average sizes existed in polyurea under larger strains. This hierarchical clustering phase morphology is probably due to the chemical crosslink agents in Isonate 143L, where polyurea tends to stiffen itself at large strain. It is worth noting that at $\varepsilon = 264\%$, the autocorrelation peak is almost twice broader than the peak at $\varepsilon = 200\%$ in both directions, as seen in **Fig. 4.5(f)**. It is probably due to the strain-induced crystallization of soft chains at large strains. Therefore, the central peak could not just represent the hard domain size when $\varepsilon > 200\%$.

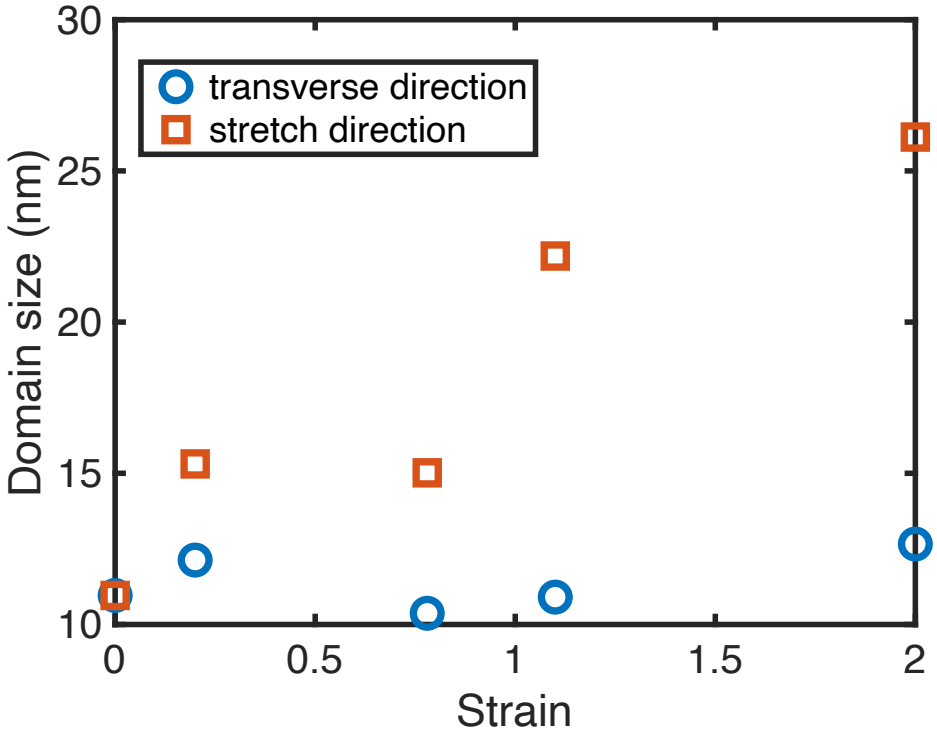

Figure 4.6 Anisotropic domain size evolution in the stretch and transverse directions at various strains identified by image autocorrelation.

4.4.2 Nanophase fragmentation and self-healing processes during stress-relaxation at fixed strains

From equilibrium phase morphologies, we have observed anisotropic hard domain coarsening in the stretch and transverse directions. However, the process of the domain anisotropic coarsening is unclear. For example, does the anisotropy come from the alignment and stretch of the hard domains along the loading direction or come from the unique fragmentation and self-healing process? To uncover the instinct domain coarsening

mechanisms, in this section, we will discuss the *in-situ* hard domain evolution process during the stress-relaxation process.

Figure 4.7 displays *in-situ* AFM tapping-mode phase images in the process of nanophase stress-relaxation at nine incremental fixed stretch strains up to 200%. The corresponding autocorrelation plots and 2D Fast Fourier Transform (FFT) images are shown in the left and right of each phase image. The loading strain rate of the device is $\sim 0.11 s^{-1}$, and the strain was held during nanophases relaxation once each desired strain level was reached. The thin film was then successively scanned at the same observation sight every 2 minutes. The slow scan direction was always from bottom to top. **Fig.4.7(a)** shows the sequential relaxation images at strain $\varepsilon_1 = 5\%$, which is way below the yielding strain $\varepsilon_y \sim 15\%$. As we can see, upon rapid loading, the polyurea reached equilibrium morphology quickly as there was no distinct change of FFT pattern as relaxation proceeded. As strain increased to $\varepsilon_2 = 15\%$ (**Fig.4.7(b)**), in the beginning 0.5 min, hard domains look as if they form fibril structures (**Fig.4.7(b$_i$)**). However, it is found material-point drifting within the observation window during the relaxation process can generate such artificial fibril-structure image. Details of the artificial fibril-structure image formation caused by material drifting with respect to the observation window is investigated and presented as follows.

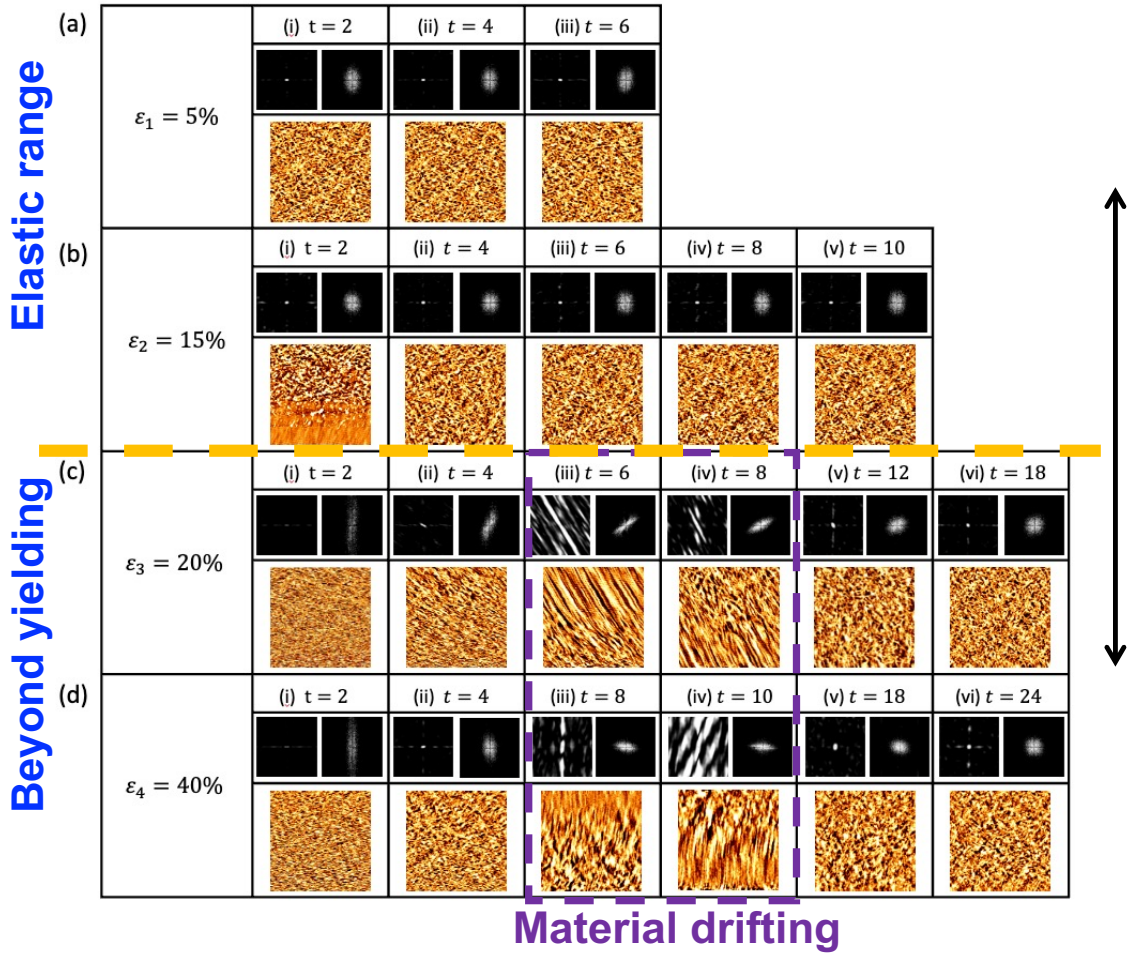
Elastic range
Beyond yielding
Material drifting
(a)
$\varepsilon_1 = 5\%$
(i) t = 2
(ii) $t = 4$
(iii) $t = 6$
(b)
$\varepsilon_2 = 15\%$
(i) t = 2
(ii) $t = 4$
(iii) $t = 6$
(iv) $t = 8$
(v) $t = 10$
(c)
$\varepsilon_3 = 20\%$
(i) t = 2
(ii) $t = 4$
(iii) $t = 6$
(iv) $t = 8$
(v) $t = 12$
(vi) $t = 18$
(d)
$\varepsilon_4 = 40\%$
(i) t = 2
(ii) $t = 4$
(iii) $t = 8$
(iv) $t = 10$
(v) $t = 18$
(vi) $t = 24$

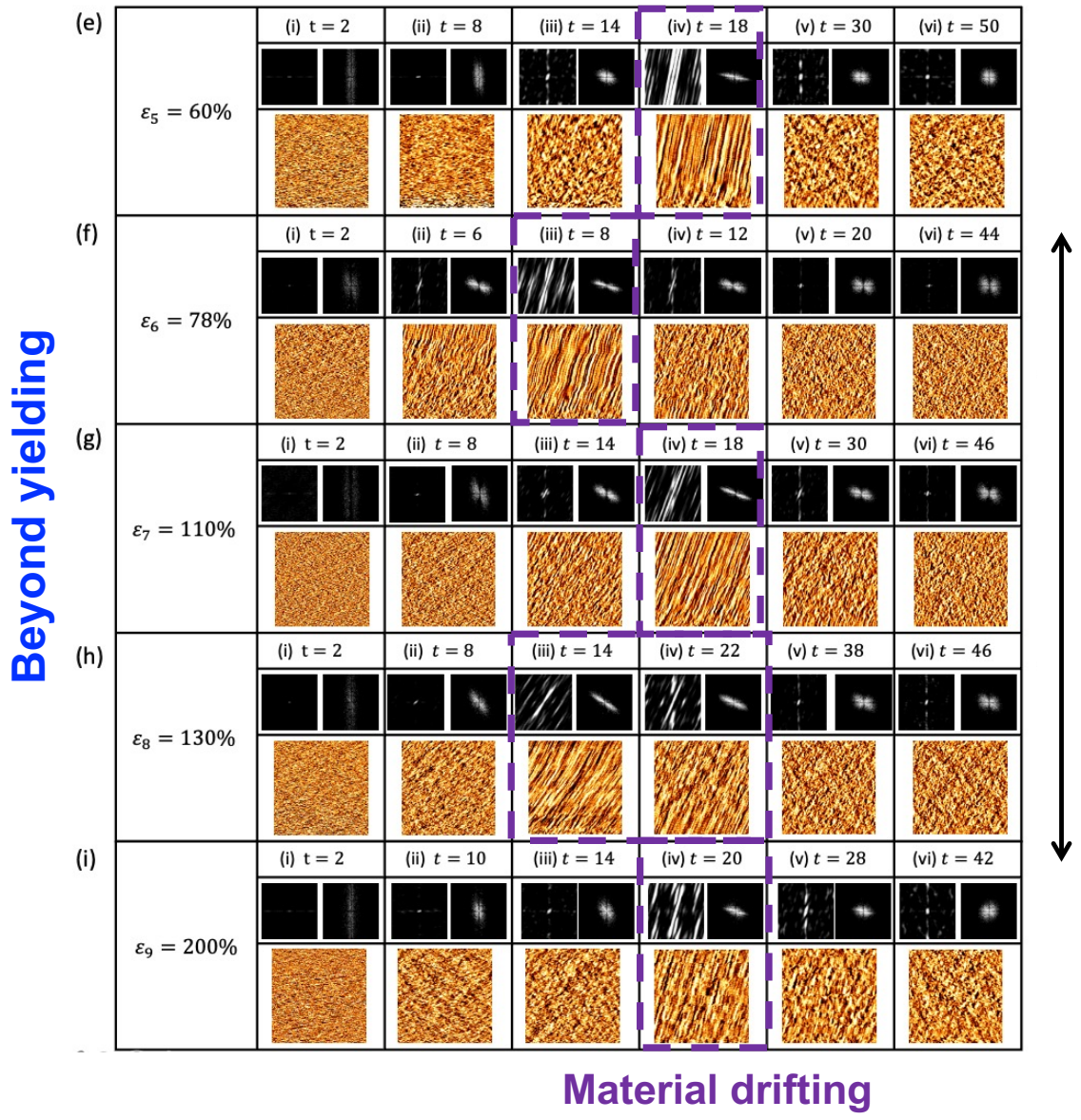

Figure 4.7 *in-situ* AFM tapping-mode phase images of a polyurea thin film under stress-relaxation process at various fixed strains for (a) ε = 5%, (b) ε = 15%, (c) ε = 20%, (d) ε = 40%, (e) ε = 60%, (f) ε = 78%, (g) ε = 110%, (h) ε = 130%, and (i) ε = 200%. The loading direction is indicated by the black arrow. The unit of time is minute. The autocorrelation image of each phase image is plotted in the left of the second row, and the 2D FFT image is plotted in the right. Images due to material drifting are marked with dotted squares.

As strain increased beyond yielding to $\varepsilon_3 = 20\%$, the nanodomain fragmentation and self-healing processes were observed. As shown in **Fig.4.7(c)**, surprisingly, at $t = 2$ min, the original rod-shaped hard domains were fragmented into smaller rod-shaped segments with the long axis densely aligned perpendicular to the loading direction, as shown in **Fig.4.7(c$_i$)**. The average long axis length of fragments is detected from image autocorrelation as $L_{long}^{frag} \cong 12nm$, which is similar to the average domain size of the undeformed sample in **Fig.4.7(a)**. The short axis length of fragments could not be precisely detected since it is smaller than the AFM phase image resolution, i.e., $L_{short}^{frag} < 3.9nm$. This fragmentation phenomenon during relaxation was not observed when the stretch strain was less than 20%. These results suggest that the fragmentation of hard domains starts if the polyurea goes beyond the elastic range, which is ~15%. However, *in-situ* SAXS on the same polyurea product showed the disassociation of hard domain happens at the strain ~0.4 where the interdomain spacing in the tensile direction starts to decrease (Rinaldi et al., 2011). As the relaxation process continued, the fragmented segments tended to coarsen and align in a preferred angle towards the tensile direction, as shown in **Fig.4.7(c$_{ii}$)**. As mentioned above, **Fig.4.7(c$_{iii}$)** exhibits fibril-structure image which was found in every strain level beyond yielding.

To understand the nature of imaging these fibril-bundle structures, two-way AFM scans, which alternated the slow-scan directions, were performed on a new sample at four different fixed strains. The results are shown in **Fig.4.8.** We found the fibril-bundle structures were still existing but did not propagate between sequential scans. For example, at $\varepsilon = 100\%$, **Fig.4.8(c$_{iv}$)** shows the fibril structure with the bottom-to-top scan but the subsequent scan (**Fig.4.8(c$_v$)**) with top-to-bottom scan does not. These results suggest that

the material drifting phenomena during the relaxation process cause the artificial imaging of these fibril-bundle structures. Particular material drifting speed and direction happened to match the AFM slow-scan frequency (2Hz in our case). The material drifting speed that caused these structures is around 8.33nm/s. As the relaxation process damps, the AFM can capture the clear phase morphology. At equilibrium, the two-way scans show identical phase images. This result suggests stress relaxation caused by domain fragmentation and the self-healing processes happens until it reaches phase equilibrium approximately in 30 minutes.

To quantify the morphology-anisotropy variation as well as identify the material drifting in the nanophase evolution process, we calculated the second spectral moment of FFT images of both one-way (**Fig.4.7**) and two-way scans (**Fig.4.8)**. The second spectral moment tensor $\mathfrak{I}$ is defined as,

$$\mathfrak{I}_{ij} = \frac{\iint \left(k_r k_r \delta_{ij} - k_i k_j\right) \hat{I}(k_1, k_2) dk_1 dk_2}{\iint \hat{I}(k_1, k_2) dk_1 dk_2} \tag{4.13}$$

where k_1, k_2 are the positions in the reciprocal space of the FFT. $\hat{I}(k_1, k_2)$ is the FFT image intensity at reciprocal space (k_1, k_2). The indices in **Eq.4.13**, i, j, implies 1 or 2, and k_r is summed over 1 and 2. We further defined the three tensor invariants, the mean value $\mathfrak{I}_{mean}$, deviatoric value $\mathfrak{I}_{dev}$, and principal axis rotation θ_p as,

$$\mathfrak{I}_{mean} = \frac{1}{2}(\mathfrak{I}_{11} + \mathfrak{I}_{22}) \tag{4.14a}$$

$$\mathfrak{I}_{dev} = \sqrt{\left(\frac{\mathfrak{I}_{11} - \mathfrak{I}_{22}}{2}\right)^2 + \mathfrak{I}_{12}^2} \tag{4.14b}$$

$$\theta_p = \frac{1}{2} tan^{-1} \frac{\mathfrak{I}_{12}}{\mathfrak{I}_{dev}}. \tag{4.14c}$$

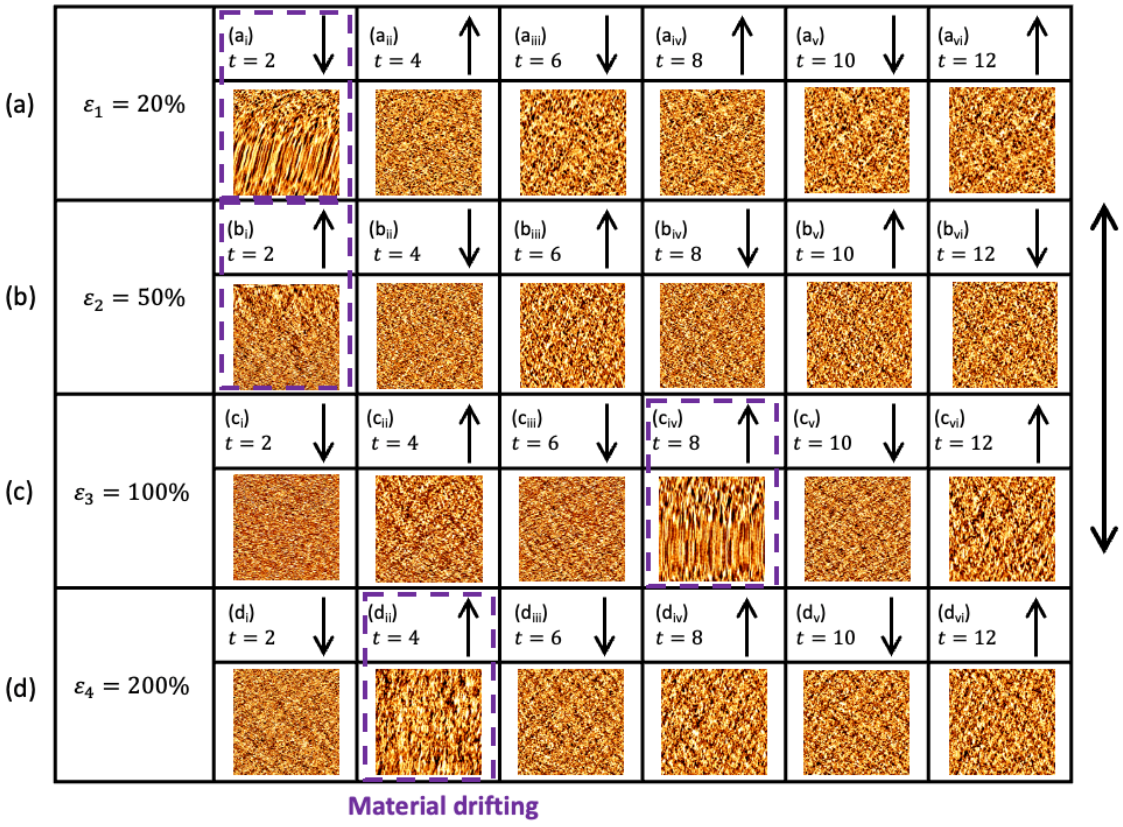

Figure 4.8 Two-way scans of *in-situ* AFM tapping-mode phase images of a polyurea thin film under stress-relaxation process from 0 to 12 mins at various fixed strains for (a) $\varepsilon = 20\%$, (b) $\varepsilon = 50\%$, (c) $\varepsilon = 100\%$, and (d) $\varepsilon = 200\%$. The loading direction is indicated by the black arrow. The unit of time is minute. Each slow-scan direction is indicted on top of each scan. Images due to material drifting are marked with dotted squares.

The time variance of $\mathfrak{I}_{mean}$, $\mathfrak{I}_{dev}$, and θ_p of 4 different strains under one-way and two-way scans are shown in **Fig.4.9** and **Fig.4.10**, respectively. For the two-way scans, the average invariants of $\mathfrak{I}_{ij}$ between two sequential scans are plotted. As shown in **Fig.4.9**, since phase morphology upon rapid loading is highly anisotropic due to the hard-domain fragmentation, $\mathfrak{I}_{mean}$ and $\mathfrak{I}_{dev}$ are very large during the fragmentation process. As the hard domains recombine into coarsened nanostructures, the interdomain spacing becomes

more isotropic. Hence, both $\mathfrak{I}_{mean}$ and $\mathfrak{I}_{dev}$ are reduced. Once the artificial fibril-bundle structures appear due to material drifting, both $\mathfrak{I}_{mean}$ and $\mathfrak{I}_{dev}$ increase the FFT patterns show strong shape anisotropy, as shown in **Fig.4.9(a)&(b)**. Interestingly, the principal axis rotation, θ_p, which characterizes the angle between the fibril and the stretch direction, is always $\sim \pm 22$ degree, where a positive value means the fibril rotates towards the left from the stretch direction, as shown in **Fig.4.9(c)**.

As we see in **Fig.4.10**, the local averaged invariants of $\mathfrak{I}_{ij}$ between two alternating-direction scans during the relaxation process have similar trends with the one-way scans but are smoother. However, the material-drifting effect is so strong that the two-way scan averaging could not annihilate the anisotropy spike of the artificial fibril-bundle-structure image, as shown in **Fig.4.10(a)&(b)**. Interestingly, regardless of the scanning direction, θ_p, is always approximately 22^o when the hard domains reach phase equilibrium at various fixed strains, as shown in **Fig.4.10(c)**. We believe this characteristic angle $\theta_p^c = 22^o$ is determined by the elastic-modulus ratio between the soft and hard domains, minimizing the strain energy for the configurational variation.

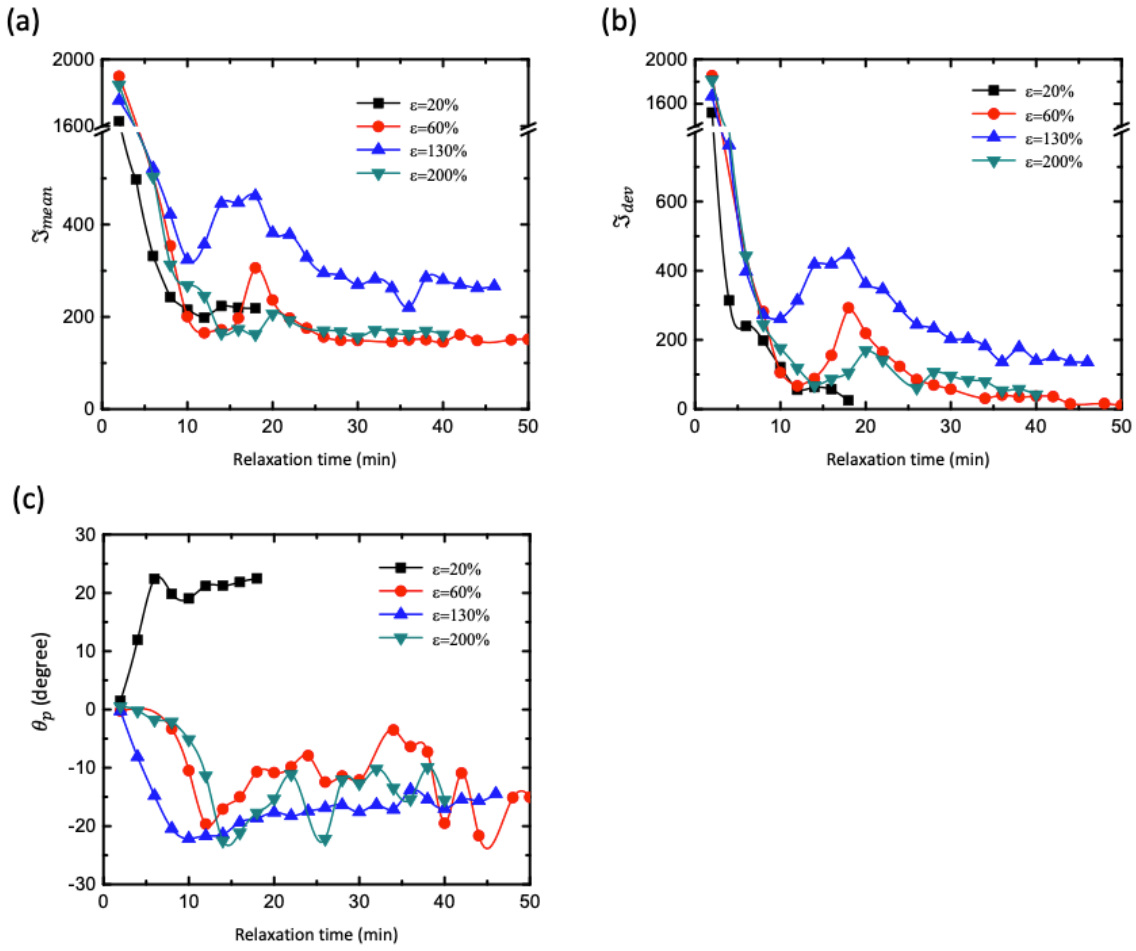

Figure 4.9 The time variation of (a) mean value of $\Im$ tensor, $\Im_{mean}$; (b) deviatoric value of $\Im$ tensor, $\Im_{dev}$; and (c) principal axial rotation of $\Im$ tensor, θ_p, for the FFT images of *in-situ* AFM tapping-mode phase images with one-way scans of 4 different strains selected in **Fig.4.7**.

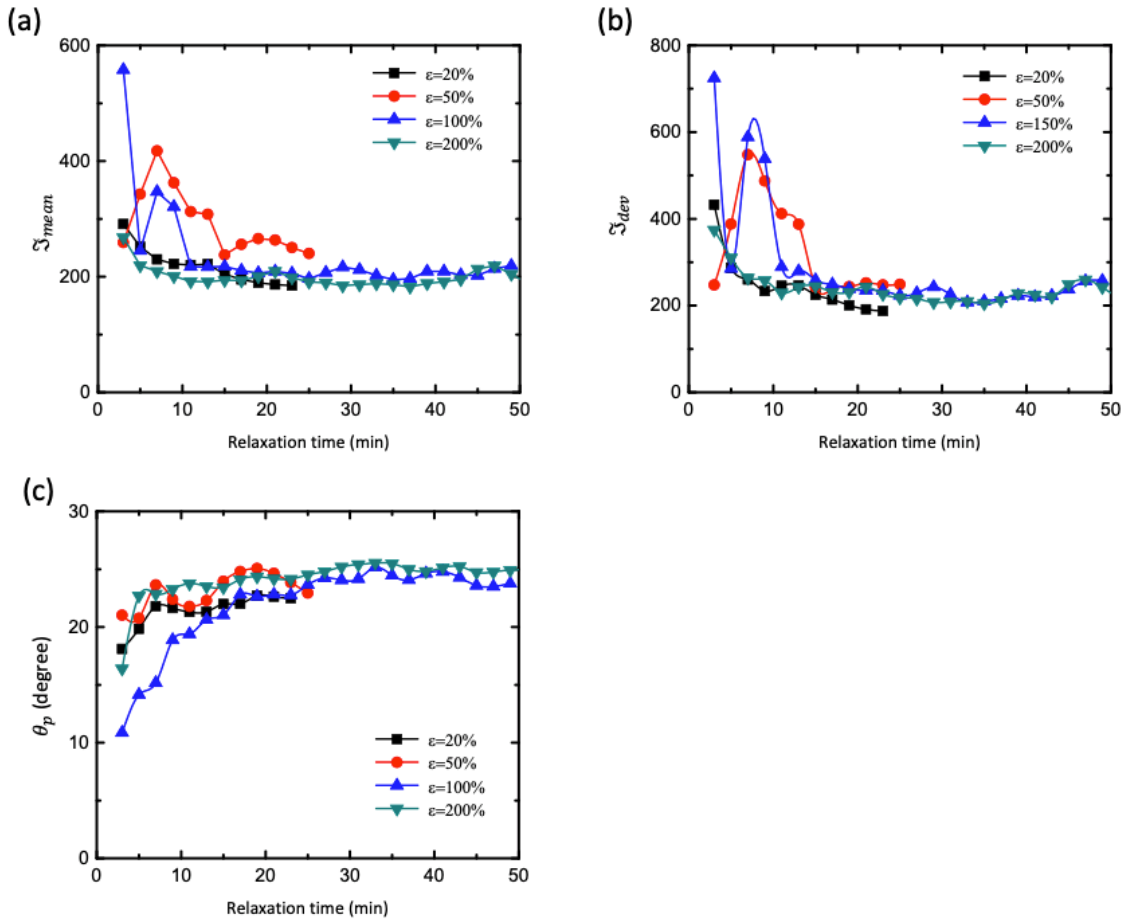

Figure 4.10 The time variation of (a) mean value of $\Im$ tensor, $\Im_{mean}$; (b) deviatoric value of $\Im$ tensor, $\Im_{dev}$; and (c) principal axial rotation of $\Im$ tensor, θ_p, for the FFT images of *in-situ* AFM tapping-mode phase images with two-way scans of 4 different strains in **Fig.4.8**.

4.4.3 Load carrying capacities between hard and soft domains during tensile deformation

We found the hard domains first fragment once the tensile strain is over yield strain in the *in-situ* AFM experiments. However, we could not record this domain fragmentation process in the AFM study since it occurs in the nanosecond timescale. Therefore, mesoscale simulation was performed, which also helps us understand the partitioning of

the load-carrying capacities between hard and soft domain to understand why polyurea exists dynamic toughening.

The simulated cross-sectional 2D morphologies of polyurea at different strains under tensile deformation are illustrated in **Fig.4.11(a)**. To characterize the hard domain orientation anisotropy, we calculated the 2D orientation-order parameter $\phi(\chi)$ at each strain, which is defined as,

$$\phi(\chi) = 2 < cos^2\chi > -1, \tag{4.15}$$

where χ is the angle between each hard domain and the stretch direction. The notation <> means the values are averaged across all hard domains. Random orientation of hard domains yields $\phi(\chi) \cong 0$. When $\phi(\chi) > 0$, the hard domains are statistically aligned towards the tensile direction with $\phi(\chi) = 1$ the perfectly aligned case. On the other hand, when $\phi(\chi) < 0$, the hard domains are statistically aligned towards the transverse direction.

Fig.4.11(b) shows the $\phi(\chi)$ for each strain in **Fig.4.11(a)**. At the undeformed state, the hard domains were almost randomly orientated since $\phi(\chi) = -0.08$. As strain increases, the hard domains first tended to align towards the stretch direction, just like regular fiber-reinforced polymer. When the strain increased to ~40%, $\phi(\chi)$ reached its maximum value. As the strain reached ~80%, $\phi(\chi)$ became a negative value. The domains had more tendency to align along the transverse direction as strain further increased. This morphology is consistent with those observed in the AFM experiments. This morphology came from the domain self-healing due to the dynamic hydrogen bonds. The Poisson contraction in the transverse direction bridged the fragmented hard domains together, resulting in this new morphology with hard domains densely distributed along the transverse direction.

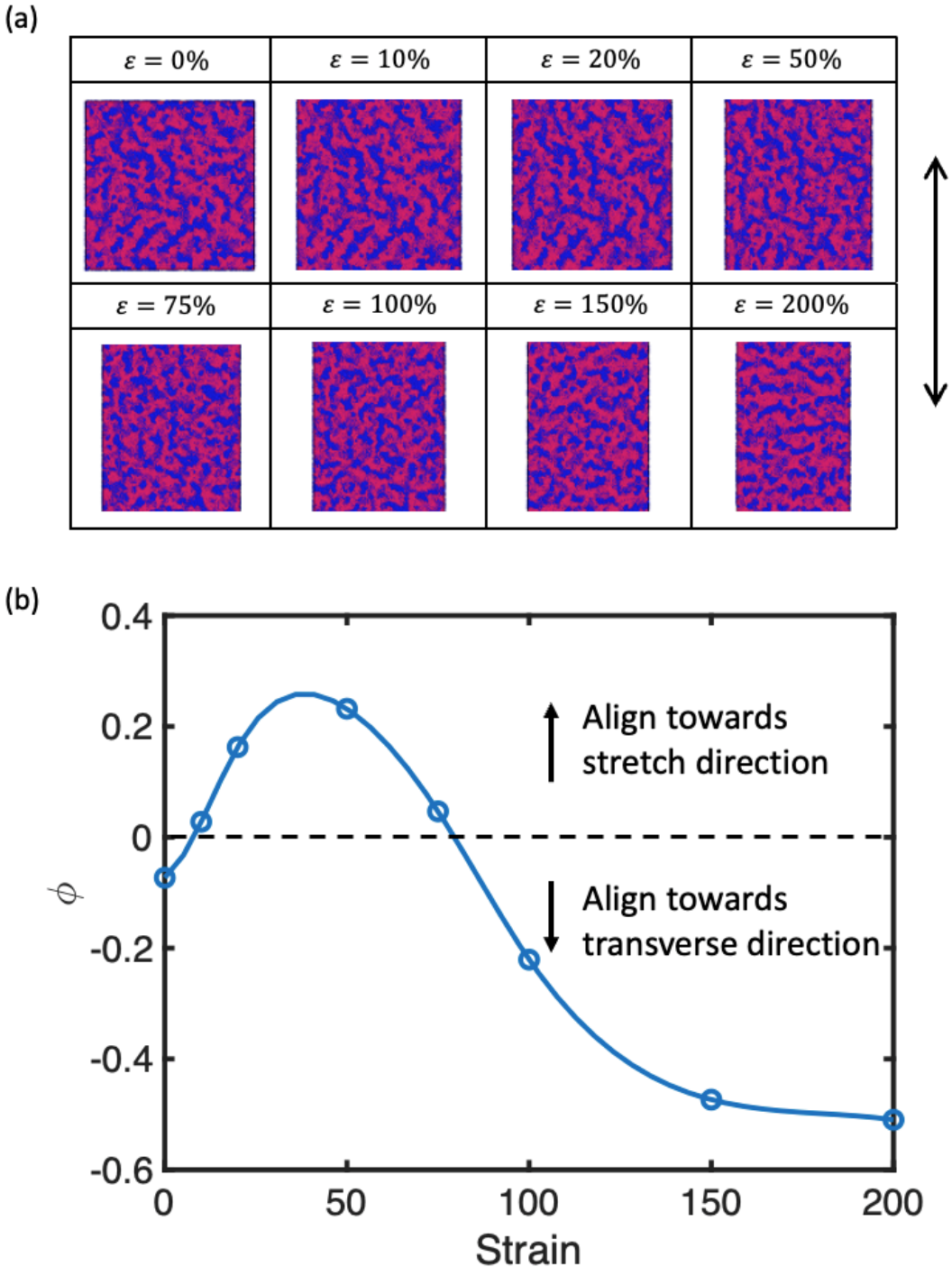

Figure 4.11 (a) Morphologies of polyurea at different strains under tensile deformation from mesoscale simulation. The red beads represent the soft domains, and the blue beads represent the hard domains. The stretch direction is indicated by the black arrow. (b) 2D order parameter ϕ as a function of 8 strains in (a).

To study the load-carrying capacities between the hard and soft domains, we calculated the total stresses in all hard and soft beads via virial theorem. The stresses in tensile and transverse directions are plotted in **Fig.4.12(a)&(b)**, respectively. At the undeformed state, the stresses in the hard domains are tensile, while the soft domains are compressive. As the strain increases, both stresses become in the stretch direction become tensile and increase monotonically. At a critical strain ($\varepsilon^{switch} = 18.6\%$), the stress in the soft domains surpasses the stress in the hard domain, which indicates most of the loading is carried by the soft domains. ε^{switch} is close to the polyurea's yield strain. This phenomenon indicates that the loading-carrying capacity of hard domains loses due to the dissociation of hard domains beyond the yielding strain, which is also consistent with the AFM observations. Even the hard domains will be self-healing later, they do not recover the load-carrying capacity anymore since they are aligned transverse to the loading direction. Our mesoscale simulation study indicates that the hard-domain fragmentation and the self-healing processes can switch the load-carrying capacity from hard domains towards soft domains under dynamic tensile loading, allowing large deformation of the soft domain. The soft-domain large deformation with nanoscale voids made by hard-domain fragmentation prevents high-strain-rate dynamic embrittlement of the polymer nanocomposite. In addition, random distribution of the hard-domain fragments resists deformation localization, exhibiting high ductility under high strain-rate loading. In turn, the high dynamic ductility is believed to make the high dynamic toughness of nanostructured copolymers.

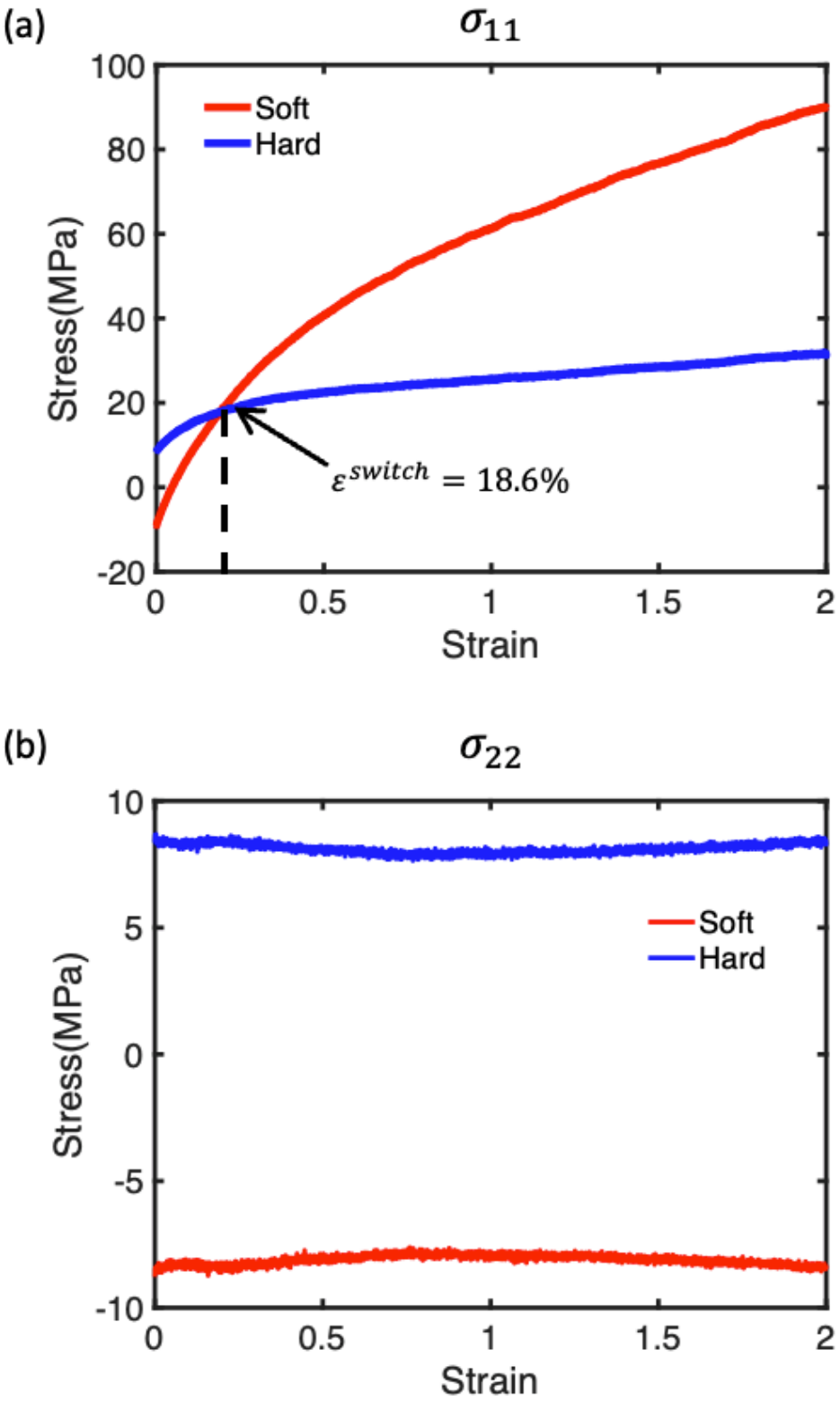

Figure 4.12 Total stresses in soft and hard domains along the (a) stretch direction, and (b) transverse direction.

4.5 Conclusions

In this chapter, we first designed and manufactured an *in-situ* AFM loading device with a twin-thread screw that provides a stationary displacement reference point with minimal drifting. We studied the kinematic characteristics of the device using DIC analysis and found the submicron observation sight trace is achievable with the combination of DIC control. Then we used the device to study the nanophase evolution processes of polyurea under stress-relaxation at various fixed strains ranging from 0% to 260% by collecting high-resolution *in-situ* AFM tapping-mode phase images. To our knowledge, this is the first *in-situ* AFM tapping-phase study of segmental block copolymers' nano and mesoscale phase transitions within the submicron scan size. From phase image autocorrelations, we found the strain-induced anisotropic hard-domain shape coarsening in the equilibrium phase morphology. Furthermore, we found the hard domains first fragment under tensile deformation once beyond yielding, and domain self-healing generates the coarsened bicontinuous structure. Coarse-grain simulations help us understand the domain fragmentation process and the load-carrying capacity between hard and soft domains. We found the hard domain fragmentation process promotes ductility of the nanocomposite structure and does not localize the homogenized deformation. In turn, the hard domain fragmentation process helps maintain the high crack-growth-incubation toughness under high-strain-rate extreme loading. The fragmentation followed by the nanoscale self-healing process constitutes the stress relaxation of nanostructured copolymers under large deformation. The relaxation mechanism further provides unusually high dynamic running-crack toughness, as measured and presented in **Chapter 3**.

Chapter 5

Conclusions and Perspectives

5.1 Concluding remarks

In this dissertation, we have successfully addressed two fundamental questions of the hierarchically nanostructured copolymer through multi-scale big-data-generating experiments and simulations: (1) What are polyurea's accurate dynamic cohesive parameters and toughness? (2) Why is polyurea so tough under dynamic loading? Key findings for each chapter are summarized here.

In Chapter 2, a deep-learning framework based on a convolutional neural network (CNN) has been proposed to inversely determine the interfacial cohesive parameters of a polyurea-coated bi-material sample in the plate impact experiments. This framework consists of an experimental technique that can generate massive image-based experimental data from a single experiment, a state-of-the-art deep learning algorithm, and a representative computational training dataset. We demonstrated that the dynamic cohesive parameters could be inversely determined with a mean average percentage error (MAPE) less than 2%.

In Chapter 3, dynamic cohesive laws, and toughness of polyurea PU1000 were successfully measured from a big-data-generating experiment with our newly invented DL-ISI by employing the deep-learning framework proposed in Chapter 2. The experimental

DL-ISI fringe image was first inpainted by a state-of-the-art cGAN model pre-trained with a corresponding FEM dataset. Subsequently, the dynamic fracture toughness of polyurea was measured as $G_c = 12100 \pm 1100 J/m^2$ under a very high crack-tip loading rate, $\dot{K} \sim 10^7 MPa\sqrt{m}/s$. We found polyurea exhibits apparent dynamic toughening, and the cohesive strength under crack-tip loading, $\sigma_c = 294 MPa$, is found to be almost three times higher than the spall strength ~105 MPa.

In Chapter 4, we chased a molecular-level understanding of polyurea's dynamic toughening through *in-situ* AFM experiments and mesoscale simulations. For this purpose, we designed and manufactured a novel *in-situ* AFM loading device with invariant observation sight. Using this device, we collected high-resolution *in-situ* AFM tapping-mode phase images of polyurea under stress-relaxation at various fixed strains ranging from 0% to 260%. From the *in-situ* AFM and coarse-grained MD simulation study, we found the hard domain fragmentation process promotes ductility of the copolymer. Furthermore, the hard domain fragmentation process helps maintain the high crack-growth-incubation toughness under high-strain-rate extreme loading. The relaxation mechanism further provides unusually high dynamic running-crack toughness.

In summary, discovering the dynamic toughening mechanism of the nanostructure copolymer could not be possible without any of the components in this thesis. With plate impact experiments coupled with DL-ISI, we could precisely measure the material motion under high strain-rate loading. With the deep learning framework, we could inversely obtain accurate dynamic toughness and cohesive parameters from the experimental data. With the mesoscale simulation, we could reveal the dynamic fragmentation processes of hydrogen-bond cross-linked hard domains under high-strain-rate deformation in the

timescale of nanoseconds, which contributes to the high crack-growth-incubation toughness. Furthermore, with the *in-situ* AFM study, we could observe the domain self-healing process, which helps the high dynamic running-crack toughness.

To our knowledge, our studies are the first precise measurement of dynamic toughness of nanostructured block copolymers, as well as the first *in-situ* AFM tapping-phase study of their nano and mesoscale phase evolutions within the submicron scan size. We believe these experimental results fill the gap in the current understanding of copolymer's cooperative failure under extreme conditions. We also believe the framework in this thesis, which consists of multi-scale big-data generating experiments and simulations, could steer the future direction on experimental mechanics, which combines the innovative high-throughput experimental techniques, multi-scale simulations, and state-of-the-art machine learning algorithms to design and characterize next-level advanced materials.

5.2 Outlook for future research

This thesis addressed some fundamental questions on the dynamic toughening mechanisms of hierarchically nanostructured copolymers, which is essential to design next-level tough soft materials under extreme loading conditions. While progress has been made, there are still some improvements and some open questions that can be addressed in future work.

(1) For simplicity and computational efficiency, we assumed the bilinear cohesive law in the bulk and interface. Even though the crack initiation and growth process are mostly governed by the fracture toughness, more detailed material-specific cohesive laws for different damage evolution could be specified in future

frameworks. Furthermore, rate-dependent cohesive laws (Salih et al., 2016) with extra rate-governing parameters can also be inversely determined through training a neural network from simulations under different strain rates.

(2) In Chapter 2, we proposed the deep learning framework to inversely determine the interfacial cohesive parameters between polyurea coating and the Al substrate. Understanding the interfacial cohesive behaviors are essential to design protective coatings under dynamic loading conditions. Also, the displacement gradient on the Al substrate is an order of magnitude smaller than the bulk polyurea during 1st crack-opening period; the full-field DL-ISI fringes could be recorded. Therefore, dynamic big-data-generating experiments on bi-material samples are needed in the future.

(3) As discussed in Chapter 3, there is a multi-fidelity issue between the computational training dataset and the experimental inputs such that FEM training datasets have low-fidelity and the experimental data have high-fidelity. A multi-fidelity neural network (MFNN), which has the capability to learn the correlations between multi-fidelity datasets, could significantly increase the prediction accuracy on the experimental inputs (Lu et al., 2020). Therefore, as more experimental fringes are collected in the future, a CNN-based multi-fidelity neural network could be developed to reduce the prediction variance on the cohesive parameters.

(4) In our *in-situ* AFM study, we observed some artificial fiber-bundle structures caused by material-point drifting during the relaxation process. If we corrected those drifting images, we could observe the whole domain evolution process from fragmentation to the equilibrium structure. Therefore, a deep-learning-based

material-drifting correction algorithm is needed for further *in-situ* AFM/SEM studies.

(5) The toughening mechanisms of polyurea from the hard-domain fragmentation and the self-healing should be valid across all strain rates. However, the fragmentation size of the hard domain depends on the loading rate (Shenoy and Kim, 2003). Therefore, a theoretical model is desired in future work to understand the relationship between the hard-domain fragmentation size and the strain rate, as well as the role of the soft matrix.

(6) As shown in our coarse-grain simulations, the effect of polydispersity on the statistical domain morphology is not distinct. However, experiments have shown polydispersity could contribute to the hierarchical clustering (Doncom et al., 2017), which is also observed in our $500nm \times 500nm$ AFM tapping morphology image. Unfortunately, our current simulation box with ~ $50nm$ size could not reveal this aspect. Therefore, extension of the current DPD simulation to an upper-level length-scale would be desired in the future to understand the clustering process due to the polydispersity.

(7) Our deep learning framework belongs to the physics-based data-driven approaches. An accurate prediction could be achieved from a reasonable amount of training datasets since we used the bilinear two-parameter cohesive laws. However, the total computational dataset will be large when the dimensions of the cohesive parameters increase. To solve such a problem with a high dimensional cohesive parameter space in the future, a state-of-the-art Bayesian framework based on deep learning (Meng et al., 2021), which can learn functional priors from historical data, can

significantly reduce the training dataset size because of the informative learned priors.

(8) The framework of our big-data-generating experiment can be widely extended to other experimental techniques to design and characterize next-level materials. For example, we could use this framework to inversely determine our blood vessel stiffness and instability modes from externally measurable massive pressure datasets (Jin et al., 2021). Or we could inversely determine the peak-polarization density on advanced 2D materials due to quantum-flexoelectric crinkles (Kothari et al., 2018) from big-data nano-particle self-assembly experiments.

Reference

Asylum NanoRack™ sample stretching stage. https://afm.oxinst.com/products/mfp-3d-other-driving-forces-acccessories/mfp-3d-nanorack-sample-stretching-stage.

Abadi, M., Barham, P., Chen, J., Chen, Z., Davis, A., Dean, J., Devin, M., Ghemawat, S., Irving, G., Isard, M., 2016. Tensorflow: A system for large-scale machine learning, 12th {USENIX} symposium on operating systems design and implementation ({OSDI} 16), pp. 265-283.

Agrawal, V., Arya, G., Oswald, J., 2014. Simultaneous Iterative Boltzmann Inversion for Coarse-Graining of Polyurea. Macromolecules 47, 3378-3389.

Agrawal, V., Holzworth, K., Nantasetphong, W., Amirkhizi, A.V., Oswald, J., Nemat-Nasser, S., 2016. Prediction of Viscoelastic Properties with Coarse-Grained Molecular Dynamics and Experimental Validation for a Benchmark Polyurea System. J Polym Sci Pol Phys 54, 797-810.

Amini, M.R., Isaacs, J., Nemat-Nasser, S., 2010. Investigation of effect of polyurea on response of steel plates to impulsive loads in direct pressure-pulse experiments. Mech Mater 42, 628-639.

Arman, B., Reddy, A.S., Arya, G., 2012. Viscoelastic Properties and Shock Response of Coarse-Grained Models of Multiblock versus Diblock Copolymers: Insights into Dissipative Properties of Polyurea. Macromolecules 45, 3247-3255.

Ashby, M.F., 2012. Materials and the environment: eco-informed material choice. Elsevier.

Bamberg, E., Grippo, C.P., Wanakamol, P., Slocum, A.H., Boyce, M.C., Thomas, E.L., 2006. A tensile test device for in situ atomic force microscope mechanical testing. Precis Eng 30, 71-84.

Barenblatt, G.I., 1983. Citation Classic - the Mathematical-Theory of Equilibrium Cracks in Brittle-Fracture. Cc/Eng Tech Appl Sci, 20-20.

Barsoum, R.G.S., 2015. Elastomeric polymers with high rate sensitivity: applications in blast, shockwave, and penetration mechanics. William Andrew.

Bazant, Z.P., 2002. Concrete fracture models: testing and practice. Eng Fract Mech 69, 165-205.

Bogoslovov, R.B., Roland, C.M., Gamache, R.M., 2007. Impact-induced glass transition in elastomeric coatings. Appl Phys Lett 90.

Bojarski, M., Del Testa, D., Dworakowski, D., Firner, B., Flepp, B., Goyal, P., Jackel, L.D., Monfort, M., Muller, U., Zhang, J., 2016. End to end learning for self-driving cars. arXiv preprint arXiv:1604.07316.

Castagna, A.M., Pangon, A., Choi, T., Dillon, G.P., Runt, J., 2012. The Role of Soft Segment Molecular Weight on Microphase Separation and Dynamics of Bulk Polymerized Polyureas. Macromolecules 45, 8438-8444.

Choi, T., Fragiadakis, D., Roland, C.M., Runt, J., 2012. Microstructure and Segmental Dynamics of Polyurea under Uniaxial Deformation. Macromolecules 45, 3581-3589.

Clifton, R., Jiao, T., 2015. Testing, Experiments and Properties of HSREP: Pressure and Strain-Rate Sensitivity of an Elastomer:(1) Pressure-Shear Plate Impact Experiments;(2) Constitutive Modeling. Elastomeric Polym. with High Rate Sensit. .

Cui, Z.W., Brinson, L.C., 2013. Thermomechanical properties and deformation of coarse-grained models of hard-soft block copolymers. Phys Rev E 88.

Das, S., Yilgor, I., Yilgor, E., Inci, B., Tezgel, O., Beyer, F.L., Wilkes, G.L., 2007. Structure-property relationships and melt rheology of segmented, non-chain extended polyureas: Effect of soft segment molecular weight. Polymer 48, 290-301.

DebenUK, 2021. In-situ Tensile & Compression stages for SEM. https://deben.co.uk/tensile-testing/sem/mini-tensile-tester-200n-compression-horizontal-bending-stage/.

Doncom, K.E., Blackman, L.D., Wright, D.B., Gibson, M.I., O'Reilly, R.K., 2017. Dispersity effects in polymer self-assemblies: a matter of hierarchical control. Chemical Society Reviews 46, 4119-4134.

Dugdale, D.S., 1960. Yielding of Steel Sheets Containing Slits. J Mech Phys Solids 8, 100-104.

Espinosa, H.D., 1992. Micromechanics of the dynamic response of ceramics and ceramic composites. Brown University.

Ferdousi, S., Chen, Q., Soltani, M., Zhu, J.D., Cao, P.F., Choi, W.B., Advincula, R., Jiang, Y.J., 2021. Characterize traction-separation relation and interfacial imperfections by data-driven machine learning models. Sci Rep-Uk 11.

Fernández-Godino, M.G., Park, C., Kim, N.-H., Haftka, R.T., 2016. Review of multi-fidelity models. arXiv preprint arXiv:1609.07196.

Flory, P.J., 1942. Thermodynamics of high polymer solutions. J Chem Phys 10, 51-61.

Freund, L., 1972. Crack propagation in an elastic solid subjected to general loading—I. Constant rate of extension. J Mech Phys Solids 20, 129-140.

Freund, L., 1973. Crack propagation in an elastic solid subjected to general loading—III. Stress wave loading. J Mech Phys Solids 21, 47-61.

Freund, L.B., 1998. Dynamic fracture mechanics. Cambridge university press.

Gao, H., Rice, J.R., 1989. A first-order perturbation analysis of crack trapping by arrays of obstacles.

Goodfellow, I.J., Pouget-Abadie, J., Mirza, M., Xu, B., Warde-Farley, D., Ozair, S., Courville, A., Bengio, Y., 2014. Generative Adversarial Networks, p. arXiv:1406.2661.

Groot, R.D., Madden, T.J., 1998. Dynamic simulation of diblock copolymer microphase separation. J Chem Phys 108, 8713-8724.

Groot, R.D., Warren, P.B., 1997. Dissipative particle dynamics: Bridging the gap between atomistic and mesoscopic simulation. J Chem Phys 107, 4423-4435.

Grujicic, M., Pandurangan, B., Bell, W.C., Cheeseman, B.A., Yen, C.F., Randow, C.L., 2011a. Molecular-level simulations of shock generation and propagation in polyurea. Mat Sci Eng a-Struct 528, 3799-3808.

Grujicic, M., Pandurangan, B., King, A.E., Runt, J., Tarter, J., Dillon, G., 2011b. Multi-length scale modeling and analysis of microstructure evolution and mechanical properties in polyurea. J Mater Sci 46, 1767-1779.

Grujicic, M., Snipes, J.S., Galgalikar, R., Ramaswami, S., 2014a. Material-Model-Based Determination of the Shock-Hugoniot Relations in Nanosegregated Polyurea. J Mater Eng Perform 23, 357-371.

Grujicic, M., Snipes, J.S., Ramaswami, S., Yavari, R., Ramasubramanian, M.K., 2014b. Meso-scale Computational Investigation of Shock-Wave Attenuation by Trailing Release Wave in Different Grades of Polyurea. J Mater Eng Perform 23, 49-64.

Grujicic, M., Yavari, R., Snipes, J.S., Ramaswami, S., Jiao, T., Clifton, R.J., 2015. Experimental and Computational Study of the Shearing Resistance of Polyurea at High Pressures and High Strain Rates. J Mater Eng Perform 24, 778-798.

Grujicic, M., Yavari, R., Snipes, J.S., Ramaswami, S., Runt, J., Tarter, J., Dillon, G., 2012. Molecular-level computational investigation of shock-wave mitigation capability of polyurea. J Mater Sci 47, 8197-8215.

Grunschel, S.E., 2009. Pressure-Shear Plate Impact Experiments on High-Purity Aluminum at Temperatures Approaching Melt. Brown University.

Heyden, S., Ortiz, M., Fortunelli, A., 2016. All-atom molecular dynamics simulations of multiphase segregated polyurea under quasistatic, adiabatic, uniaxial compression. Polymer 106, 100-108.

Hinton, G., Deng, L., Yu, D., Dahl, G.E., Mohamed, A., Jaitly, N., Senior, A., Vanhoucke, V., Nguyen, P., Sainath, T.N., Kingsbury, B., 2012. Deep Neural Networks for Acoustic Modeling in Speech Recognition: The Shared Views of Four Research Groups. IEEE Signal Processing Magazine 29, 82-97.

Hong, S., Chew, H.B., Kim, K.S., 2009. Cohesive-zone laws for void growth - I. Experimental field projection of crack-tip crazing in glassy polymers. J Mech Phys Solids 57, 1357-1373.

Hong, S.S., Kim, K.S., 2003. Extraction of cohesive-zone laws from elastic far-fields of a cohesive crack tip: a field projection method. J Mech Phys Solids 51, 1267-1286.

Hoogerbrugge, P.J., Koelman, J.M.V.A., 1992. Simulating Microscopic Hydrodynamic Phenomena with Dissipative Particle Dynamics. Europhys Lett 19, 155-160.

Hsu, Y.C., Yu, C.H., Buehler, M.J., 2020. Using Deep Learning to Predict Fracture Patterns in Crystalline Solids. Matter-Us 3, 197-211.

Huang, H.J., Alexander-Katz, A., 2019. Dissipative particle dynamics for directed self-assembly of block copolymers. J Chem Phys 151.

Huggins, M.L., 1941. Solutions of long chain compounds. J Chem Phys 9, 440-440.

Isola, P., Zhu, J.-Y., Zhou, T., Efros, A.A., 2016. Image-to-Image Translation with Conditional Adversarial Networks, p. arXiv:1611.07004.

Jain, A., Youssef, G., Gupta, V., 2013. Dynamic tensile strength of polyurea-bonded steel/E-glass composite joints. J Adhes Sci Technol 27, 403-412.

Jia, Z.Z., Amirkhizi, A.V., Nantasetphong, W., Nemat-Nasser, S., 2016. Experimentally-based relaxation modulus of polyurea and its composites. Mech Time-Depend Mat 20, 155-174.

Jiao, T., Clifton, R.J., 2014. Measurement of the response of an elastomer at pressures up to 9 GPa and shear-rates of 105 – 106s−1. Journal of Physics: Conference Series 500, 112036.

Jin, H., Landauer, A.K., Kim, K.-S., 2021. Ruga mechanics of soft-orifice closure under external pressure. Proceedings of the Royal Society A 477, 20210238.

Judge, T.R., Bryanston-Cross, P., 1994. A review of phase unwrapping techniques in fringe analysis. Optics and Lasers in Engineering 21, 199-239.

Keutsch, F.N., Saykally, R.J., 2001. Water clusters: Untangling the mysteries of the liquid, one molecule at a time. Proceedings of the National Academy of Sciences 98, 10533-10540.

Kim, H., Citron, J., Youssef, G., Navarro, A., Gupta, V., 2012. Dynamic fracture energy of polyurea-bonded steel/E-glass composite joints. Mech Mater 45, 10-19.

Kim, K.-S., Jin, H., Jiao, T., Clifton, R.J., 2021. Dynamic Fracture-Toughness Testing of a Hierarchically Nano-Structured Solid. Springer International Publishing, Cham, pp. 97-100.

Kim, K.S., 1980. Plane wave experiments in dynamic plasticity. Brown University.

Kim, K.S., Clifton, R.J., Kumar, P., 1977. A combined normal-and transverse-displacement interferometer with an application to impact of y-cut quartz. Journal of Applied Physics 48, 4132-4139.

Kim, K.S., McMeeking, R.M., Johnson, K.L., 1998. Adhesion, slip, cohesive zones and energy fluxes for elastic spheres in contact. J Mech Phys Solids 46, 243-266.

Kingma, D.P., Ba, J., 2014. Adam: A Method for Stochastic Optimization, p. arXiv:1412.6980.

Kothari, M., Cha, M.-H., Kim, K.-S., 2018. Critical curvature localization in graphene. I. Quantum-flexoelectricity effect. Proceedings of the Royal Society A: Mathematical, Physical and Engineering Sciences 474, 20180054.

Kremer, K., Grest, G.S., 1990. Dynamics of Entangled Linear Polymer Melts - a Molecular-Dynamics Simulation. J Chem Phys 92, 5057-5086.

Krizhevsky, A., Sutskever, I., Hinton, G.E., 2012. ImageNet classification with deep convolutional neural networks, Proceedings of the 25th International Conference on Neural Information Processing Systems - Volume 1. Curran Associates Inc., Lake Tahoe, Nevada, pp. 1097–1105.

Kumar, P., Clifton, R.J., 1977. Optical Alignment of Impact Faces for Plate Impact Experiments. Journal of Applied Physics 48, 1366-1367.

Landauer, A.K., Patel, M., Henann, D.L., Franck, C., 2018. A q-Factor-Based Digital Image Correlation Algorithm (qDIC) for Resolving Finite Deformations with Degenerate Speckle Patterns. Exp Mech 58, 815-830.

LeCun, Y., Bengio, Y., Hinton, G., 2015. Deep learning. Nature 521, 436-444.

Li, Q.Y., Kim, K.S., 2008. Micromechanics of friction: effects of nanometre-scale roughness. P Roy Soc a-Math Phy 464, 1319-1343.

Li, Q.Y., Kim, K.S., 2009. Micromechanics of Rough Surface Adhesion: A Homogenized Projection Method. Acta Mech Solida Sin 22, 377-390.

Li, T., Zhang, C., Xie, Z.N., Xu, J., Guo, B.H., 2018. A multi-scale investigation on effects of hydrogen bonding on microstructure and macro-properties in a polyurea. Polymer 145, 261-271.

Li, T., Zheng, T.Z., Han, J.R., Liu, Z.L., Guo, Z.X., Zhuang, Z., Xu, J., Guo, B.H., 2019. Effects of Diisocyanate Structure and Disulfide Chain Extender on Hard Segmental Packing and Self-Healing Property of Polyurea Elastomers. Polymers-Basel 11.

Liu, M.H., Oswald, J., 2019. Coarse-grained molecular modeling of the microphase structure of polyurea elastomer. Polymer 176, 1-10.

Liu, X., Athanasiou, C.E., Padture, N.P., Sheldon, B.W., Gao, H.J., 2020. A machine learning approach to fracture mechanics problems. Acta Mater 190, 105-112.

Liu, X., Athanasiou, C.E., Padture, N.P., Sheldon, B.W., Gao, H.J., 2021. Knowledge extraction and transfer in data-driven fracture mechanics. P Natl Acad Sci USA 118.

Lu, L., Dao, M., Kumar, P., Ramamurty, U., Karniadakis, G.E., Suresh, S., 2020. Extraction of mechanical properties of materials through deep learning from instrumented indentation. P Natl Acad Sci USA 117, 7052-7062.

Manav, M., Ortiz, M., 2021. Molecular dynamics study of the shock response of polyurea. Polymer 212.

Meng, X., Karniadakis, G.E., 2020. A composite neural network that learns from multi-fidelity data: Application to function approximation and inverse PDE problems. J Comput Phys 401, 109020.

Meng, X., Yang, L., Mao, Z., Ferrandis, J.d.A., Karniadakis, G.E., 2021. Learning Functional Priors and Posteriors from Data and Physics. arXiv preprint arXiv:2106.05863.

Mirza, M., Osindero, S., 2014. Conditional Generative Adversarial Nets, p. arXiv:1411.1784.

Mohammed, I., Liechti, K.M., 2000. Cohesive zone modeling of crack nucleation at bimaterial corners. J Mech Phys Solids 48, 735-764.

Ni, B., Gao, H.J., 2021. A deep learning approach to the inverse problem of modulus identification in elasticity. Mrs Bull 46, 19-25.

Pan, S.J., Yang, Q., 2009. A survey on transfer learning. IEEE Transactions on knowledge and data engineering 22, 1345-1359.

Pangon, A., Dillon, G.P., Runt, J., 2014. Influence of mixed soft segments on microphase separation of polyurea elastomers. Polymer 55, 1837-1844.

Parkhi, O.M., Vedaldi, A., Zisserman, A., 2015. Deep face recognition.

Pathak, J.A., Twigg, J.N., Nugent, K.E., Ho, D.L., Lin, E.K., Mott, P.H., Robertson, C.G., Vukmir, M.K., Epps, T.H., Roland, C.M., 2008. Structure Evolution in a Polyurea Segmented Block Copolymer Because of Mechanical Deformation. Macromolecules 41, 7543-7548.

Plimpton, S., 1995. Fast Parallel Algorithms for Short-Range Molecular-Dynamics. J Comput Phys 117, 1-19.

Raissi, M., Perdikaris, P., Karniadakis, G.E., 2019. Physics-informed neural networks: A deep learning framework for solving forward and inverse problems involving nonlinear partial differential equations. J Comput Phys 378, 686-707.

Ravichandran, G., 1987. Dynamic fracture under plane wave loading. Brown University.

Ravichandran, G., Clifton, R.J., 1989. Dynamic Fracture under Plane-Wave Loading. Int J Fracture 40, 157-201.

Rezaei, M., Harmuth, K., Gierke, W., Kellermeier, T., Fischer, M., Yang, H., Meinel, C., 2017. Conditional Adversarial Network for Semantic Segmentation of Brain Tumor, p. arXiv:1708.05227.

Rice, J.R., Ben-Zion, Y., Klm, K.-S., 1994. Three-dimensional perturbation solution for a dynamic planar crack moving unsteadily in a model elastic solid. J Mech Phys Solids 42, 813-843.

Rinaldi, R.G., Boyce, M.C., Weigand, S.J., Londono, D.J., Guise, M.W., 2011. Microstructure Evolution during Tensile Loading Histories of a Polyurea. J Polym Sci Pol Phys 49, 1660-1671.

Roland, C.M., Casalini, R., 2007. Effect of hydrostatic pressure on the viscoelastic response of polyurea. Polymer 48, 5747-5752.

Roland, C.M., Twigg, J.N., Vu, Y., Mott, P.H., 2007. High strain rate mechanical behavior of polyurea. Polymer 48, 574-578.

Ronneberger, O., Fischer, P., Brox, T., 2015. U-Net: Convolutional Networks for Biomedical Image Segmentation, p. arXiv:1505.04597.

Salih, S., Davey, K., Zou, Z., 2016. Rate-dependent elastic and elasto-plastic cohesive zone models for dynamic crack propagation. Int J Solids Struct 90, 95-115.

Sami, S., Yildirim, E., Yurtsever, M., Yurtsever, E., Yilgor, E., Yilgor, I., Wilkes, G.L., 2014. Understanding the influence of hydrogen bonding and diisocyanate symmetry on the morphology and properties of segmented polyurethanes and polyureas: Computational and experimental study. Polymer 55, 4563-4576.

Sanchez-Lengeling, B., Aspuru-Guzik, A., 2018. Inverse molecular design using machine learning: Generative models for matter engineering. Science 361, 360-365.

Sarva, S.S., Deschanel, S., Boyce, M.C., Chen, W.N., 2007. Stress-strain behavior of a polyurea and a polyurethane from low to high strain rates. Polymer 48, 2208-2213.

Shenoy, V., Kim, K.-S., 2003. Disorder effects in dynamic fragmentation of brittle materials. J Mech Phys Solids 51, 2023-2035.

Shi, Z., Tsymbalov, E., Dao, M., Suresh, S., Shapeev, A., Li, J., 2020. Deep elastic strain engineering of bandgap through machine learning (vol 116, pg 4117, 2019). P Natl Acad Sci USA 117, 6274-6274.

Shim, J., Mohr, D., 2009. Using split Hopkinson pressure bars to perform large strain compression tests on polyurea at low, intermediate and high strain rates. Int J Impact Eng 36, 1116-1127.

Su, M., Peng, H., Yuan, M., Li, S.F., 2021. Identification of the interfacial cohesive law parameters of FRP strips externally bonded to concrete using machine learning techniques. Eng Fract Mech 247.

Tambe, N.S., Bhushan, B., 2004. In situ study of nano-cracking in multilayered magnetic tapes under monotonic and fatigue loading using an AFM. Ultramicroscopy 100, 359-373.

Tvergaard, V., Hutchinson, J.W., 1996. Effect of strain dependent cohesive zone model on predictions of interface crack growth. J Phys Iv 6, 165-172.

Wisse, E., Spiering, A.J.H., van Leeuwen, E.N.M., Renken, R.A.E., Dankers, P.Y.W., Brouwer, L.A., van Luyn, M.J.A., Harmsen, M.C., Sommerdijk, N.A.J.M., Meijer, E.W., 2006. Molecular recognition in poly(epsilon-caprolactone)-based thermoplastic elastomers. Biomacromolecules 7, 3385-3395.

Xu, X.P., Needleman, A., 1993. Void Nucleation by Inclusion Debonding in a Crystal Matrix. Model Simul Mater Sc 1, 111-132.

Yang, Z.Z., Yu, C.H., Buehler, M.J., 2021a. Deep learning model to predict complex stress and strain fields in hierarchical composites. Sci Adv 7.

Yang, Z.Z., Yu, C.H., Guo, K., Buehler, M.J., 2021b. End-to-end deep learning method to predict complete strain and stress tensors for complex hierarchical composite microstructures. J Mech Phys Solids 154.

Yao, K.L., Liu, Z.L., Li, T., Guo, B.H., Zhuang, Z., 2020. Mesoscale structure-based investigation of polyurea dynamic modulus and shock-wave dissipation. Polymer 202.

Yi, J., Boyce, M.C., Lee, G.F., Balizer, E., 2006. Large deformation rate-dependent stress-strain behavior of polyurea and polyurethanes. Polymer 47, 319-329.

Yilgor, E., Yilgor, I., Yurtsever, E., 2002. Hydrogen bonding and polyurethane morphology. I. Quantum mechanical calculations of hydrogen bond energies and vibrational spectroscopy of model compounds. Polymer 43, 6551-6559.

Young, R., Lovell, P., 2011. Introduction to Polymers. CRC press.

Youssef, G., Gupta, V., 2012. Dynamic tensile strength of polyurea. J Mater Res 27, 494-499.

Zhang, E., Yin, M., Karniadakis, G.E., 2020. Physics-Informed Neural Networks for Nonhomogeneous Material Identification in Elasticity Imaging, p. arXiv:2009.04525.

Zhang, Z., Clifton, R.J., 2003. Shear band propagation from a crack tip. J Mech Phys Solids 51, 1903-1922.

Zhang, Z., Clifton, R.J., 2007. Shear band propagation from a crack tip subjected to Mode II shear wave loading. Int J Solids Struct 44, 1900-1926.

Zhao, J., Knauss, W.G., Ravichandran, G., 2007. Applicability of the time-temperature superposition principle in modeling dynamic response of a polyurea. Mech Time-Depend Mat 11, 289-308.

Zhu, Y., Liechti, K.M., Ravi-Chandar, K., 2009. Direct extraction of rate-dependent traction-separation laws for polyurea/steel interfaces. Int J Solids Struct 46, 31-51.